First Measurement of the B_s^0 Semileptonic Branching Ratio to an Orbitally Excited D_s^{**} State, $Br(B_s^0 \to D_{s1}^-(2536)\mu^+\nu X)$

Jason Rieger

Submitted to the faculty of the University Graduate School

in partial fulfillment of the requirements

for the degree

Doctor of Philosophy

in the Department of Physics

Indiana University

December 8, 2007

Accepted by the Graduate Faculty, Indiana University, in partial fulfillment of the requirements for the degree of Doctor of Philosophy.

Rick Van Kooten, Ph.D.

Mike Berger, Ph.D.

Jon Urheim, Ph.D.

Andrzej Zieminski, Ph.D.

December 8, 2007

Acknowledgments

In every thesis, the advisor is acknowledged first. Having completed my thesis and reached the acknowledgments section, I definitely understand why.

My advisor, Rick Van Kooten, has not only been my advisor throughout this research, but has been one of the most influential people in my life during that time. Sure, he possesses an amazing physics mind and is a font of knowledge, but that's only a part of it. He also has been patient and understanding during times when I've struggled with my research and has provided guidance at every step. Without question, I will always compare every future boss during my career to Rick and comparing favorably will always be an uphill battle (unless my current boss is reading, in which case, you're the best!). So, it is with extreme admiration that I thank my advisor.

I would also like to acknowledge the contribution of Andrzej Zieminski, who lead my Editorial Board during the formative years of this analysis. His guidance and suggestions were integral to the success of this analysis and helped usher this analysis through to completion. Thank also go to Gene Fisk, Arthur Maciel, and all the members of my EB.

I'd also like to thank the entire B Physics group and convenors who's excellent questions and suggestions have contributed to a well rounded analysis. Special thanks go to Brendan Casey, not only for his keen insight and willingness to help, but for always making conferences more entertaining.

And then there's all the friends one makes while in a large collaboration. Miko and Tuula were the first friends I made upon arriving at Fermilab and have been great. Dan, Jorge, Joel, and Len are always great to see around the lab or at a party. And definitely I have to acknowledge the other Dan, my office mate at Fermilab who was always helpful. It definitely helped to have an experienced person sitting to my right. And, of course, all of my friends throughout the years at Indiana University, especially Aaron and Karen who helped make graduate school survivable by simply being great friends.

But most importantly, I'd like to thank my family. My parents have always been supportive of my career endevours and have never tried to steer me in a direction I didn't want to go. They have stood behind me during times when I was doubting myself, offering encouragement and support. I'd also like to thank my brothers for giving me excellent role models in life. And then there's my in-laws, who have done so much for me and treated me like a son. I'm not sure that I would have made it through the last months before my defense without their help.

Finally, and most importantly, I'd like to thank my beautiful wife, Leah. Of course, simple thanks are nowhere near enough. How do you thank some-

one who's been your wife, best friend, office mate, lab partner and running partner for all your adult life. Just regarding this analysis, she has helped me in every facet of research, from debugging code to acting as a physics sounding board. But that's the least of it. To put it as simply as I can, she has made me a better person in every aspect of my life and I'd be half as successful without her. She challenges me at every turn and I am unbelievably lucky to have found her.

Abstract

In a data sample of approximately 1.3 fb^{-1} collected with the DØ detector between 2002 and 2006, the orbitally excited charm state $D_{s1}^{\pm}(2536)$has been observed with a measured mass of $2535.7 \pm 0.6\,(\text{stat}) \pm 0.5\,(\text{syst})\,\text{MeV}/c^2$ via the decay mode $B_s^0 \to D_{s1}^-(2536)\mu^+\nu X$followed by $D_{s1}^{\pm}(2536) \to D^{*\pm}K_S^0$. By normalizing to the known branching ratio $Br(\bar{b} \to D^{*-}\mu^+\nu X)$ and to the number of reconstructed D^* mesons with an associated identified muon, a first-ever measurement is made of the product branching ratio $(\bar{b} \to D_{s1}^-(2536)\mu^+\nu X) \cdot Br(D_{s1}^- \to D^{*-}K_S^0)$. Assuming that $D_{s1}^-(2536)$ production in semileptonic decay is entirely from B_s^0, an extraction of the semileptonic branching ratio $Br(B_s^0 \to D_{s1}^-(2536)\mu^+\nu X)$ is made. Comparisons are made with theoretical expectations.

Contents

List of Tables

List of Figures

Chapter 1

Introduction

Ever since the earliest human gained the capacity for rational thought, he has questioned where he came from and how the universe works. Unfortunately for early man, the tools with which to answer these questions didn't come around for another 100 million years. Luckily for the reader, Particle Physics (or High Energy Physics, as it's also commonly known) seeks to answer these most fundamental questions with the Standard Model.

In Chapter 2, we present a brief overview of the Standard Model and give a motivation for the topic of this thesis, the measurement of $Br(B_s^0 \to D_{s1}^-(2536)\mu^+\nu X)$. We will then discuss the theoretical basis for this analysis and then in Chapters 3 and 4 we will describe the DØ detector which was used to collect data for this measurement and the reconstruction of this data, respectively. Chapter 5 will discuss the measurement of $Br(B_s^0 \to D_{s1}^-(2536)\mu^+\nu X)$ and finally Chapter 6 will compare the measurement with theoretical predictions.

Chapter 2

Theoretical Basis for Measurement

In this section, we will discuss the theoretical framework that provides a basis for the research described in this thesis.

2.1 Standard Model

The Standard Model (SM) [1] is a theoretical construct that provides the framework for Elementary Particle Physics. Having survived rigorous testing thus far, its predictions have been matched by experimental data with remarkable precision. However, some of the restrictions of the SM are that it predicts neither particle masses nor includes gravity and thus physicists are continually motivated to extend the theory into new realms.

The Standard Model of particle physics describes the most fundamental particles and their interactions. Particles in the Standard Model fall into two

categories: fermions and bosons. Fermions, particles with half-integer spin that obey Fermi-Dirac statistics, interact through forces mediated by bosons, which have integer spin and obey Bose-Einstein statistics. Fermions can be further divided into two classes of particles, quarks and leptons. Quarks are fundamental particles with charge of either $-1/3$ or $+2/3$ that combine to form mesons and baryons. There are six types of quarks: the up (u), down (d), strange (s), charm (c), bottom (b), and top (t). The u, c, and t quarks are referred to as the 'up-type' quarks with charge $+2/3$ and the d, s, b are referred to as the 'down-type' quarks with a charge of $-1/3$. Aside for the top quark, which is too short-lived to hadronize with other quarks to form mesons and baryons, the quarks are the major constituents of matter, together forming all hadrons observed either in nature or in the laboratory.

The six leptons consist of the electron (e), muon (μ), tau (τ), and their complementary neutrinos (ν_e, ν_μ, and ν_τ). Neutrinos have been found to have a very small mass [2], although predicted to be massless by the original incarnation of the SM. Quarks and leptons combine to form the elementary particles that comprise the known universe and interact through forces mediated by bosons. Every particle in the Standard Model has an anti-particle with opposite fundamental properties, including spin and charge. The quarks and leptons can be divided up into generations, with each quark doublet consisting of and up-like and a down-like quark and each lepton doublet consisting of a charged lepton and a neutral neutrino. Described in the tables

below are the quarks (Table 2.1) and leptons (Table 2.2) along with their basic properties [3].

Table 2.1: The fundamental quarks.

Particle Name	Symbol	Charge	Mass (MeV)	Generation
up	u	$+2/3$	~ 3	1
down	d	$-1/3$	~ 5	
charm	c	$+2/3$	~ 1200	2
strange	s	$-1/3$	~ 100	
top	t	$+2/3$	$\sim 178,000$	3
bottom	b	$-1/3$	~ 4500	

Table 2.2: The fundamental leptons.

Particle Name	Symbol	Charge	Mass (MeV)	Generation
electron	e^-	-1	0.511	1
electron neutrino	ν_e	0	< 0.000003	
muon	μ	-1	105.6	2
muon neutrino	ν_μ	0	< 0.19	
tau	τ	-1	1777	3
tau neutrino	ν_τ	0	< 18.2	

Mediating the interaction between fermions are the vector gauge bosons: the photon (γ), Z^0 and $W^\pm$, and gluons (g). The electromagnetic field, quantized within the Quantum Electrodynamic Theory (QED) [4], is mediated by the photon, falling off as the square of the distance and having infinite range. Mediating the weak force are the massive Z^0 and $W^\pm$ bosons and this force

operates at short distances ($\sim 10^{-16}$ cm). The electromagnetic and weak forces are unified by a gauge theory, the electroweak force. The gauge symmetry group of the electroweak force, $SU(2)_L \times U(1)_Y$ requires four massless gauge bosons. However, through a mechanism known as spontaneous symmetry breaking [5], the Z^0 and $W^{\pm}$ acquire mass and the remaining massless gauge boson is the photon. The introduction of the Higgs mechanism allows for this spontaneous symmetry breaking and brings to light a new particle, the Higgs boson. Thus far the Higgs boson has not been discovered.

Finally, the strong force is mediated by gluons. The gluon couples to a 'color' charge much as the photon couples to electric charge described by Quantum Chromodynamics (QCD) [6], a theory analogous to QED in that QCD is the quantization of the color field. QCD is an $SU(3)_C$ gauge field theory with three fundamental colors in the representation of the group. The three colors are known as red, green, and blue with their complementary anti-charges. Gluons have a color associated with them as well and thus will interact with each other.

The strong force is dependent on a coupling constant that increases with the distance between particles and thus the force becomes stronger with distance. This results in 'quark confinement'. As the distance between quarks increases, the quarks will either be brought back together by this increased attraction or the energy will be great enough to create a quark-antiquark pair. Due to this process, the particles we observe are always color neutral

and thus we find an absence of single quarks. At shorter distances, the coupling constant grows weaker and the quarks behave as free particles, a process known as 'asymptotic freedom.' This asymptotic freedom only becomes evident at high energies. This makes particle accelerators ideal instruments for probing the depths of these particles.

Gravity, the most readily observed force in everyday life, is not described in the Standard Model. Gravity interacts at long ranges but is an extremely weak force and does not have a bearing on particle interactions at the subatomic level.

Table 2.3: The fundamental forces and properties [3].

Force	Carrier	Range (cm)	Relative Strength	Mass (GeV)	Charge	Spin
Gravity	graviton (G)	infinite	10^{-40}	0	0	2
Weak	W^+	$\sim 10^{-16}$	10^{-6}	80.4	1	1
	W^-			80.4	-1	1
	Z^0			91.2	0	1
EM	photon (γ)	infinite	10^{-2}	0	0	1
Strong	gluons (g)	$\sim 10^{-13}$	1	0	0	1

2.2 CP Violation and the Unitarity CKM Matrix

2.2.1 The Unitarity CKM Matrix

The research described in this thesis will be dealing with a weak decay of a b quark to a charm quark. To understand this process, it is necessary to examine the weak decay process in the Standard Model. Within the Standard Model, the weak charged current between the up-like and down-like quark families is represented by the following form:

$$J_{\mu}^{CC} = (\bar{u}, \bar{c}, \bar{t})\gamma_{\mu}\frac{(1-\gamma^5)}{2}U\begin{pmatrix} d \\ s \\ b \end{pmatrix}, \tag{2.1}$$

where U is a unitary 3×3 matrix known as the Cabibbo-Kobayashi-Maskawa (CKM) matrix [7] and $\frac{\gamma_{\mu}(1-\gamma^5)}{2}$ is the weak charge current, with $\gamma^5 = i\gamma^0\gamma^1\gamma^2\gamma^3$. The elements of the CKM matrix are given by

$$\begin{pmatrix} V_{ud} & V_{us} & V_{ub} \\ V_{cd} & V_{cs} & V_{cb} \\ V_{td} & V_{ts} & V_{tb} \end{pmatrix}, \tag{2.2}$$

where each element of the CKM matrix is a complex number representing the coupling strength between up-like and down-like quarks. The matrix elements represent the interaction amplitude of the decay vertex from down-

like quarks through the weak interaction to up-like quarks. For example, the decay vertex at which a b quark decays through a W^- to a c quark would include a term represented by V_{cb}. Conversely, for decays of up-like quarks to down-like quarks, the interaction amplitude is represented by the complex conjugate of the respective matrix element, i.e., the decay of a top quark to a bottom quark through a W^+ boson would be proportional to V_{tb}^*.

As a $n \times n = 3 \times 3$ complex matrix, there would generally be 18 ($2n^2$) free parameters to describe the matrix. The requirement that this matrix be unitary, i.e. $V^\dagger V = 1$, reduces this number of parameters by a factor of two, leaving n^2 parameters. The phases are arbitrary, so $2n-1$ can be eliminated by phase rotations, bringing the total number of free parameters to $(n-1)^2$ for $n = 1$. These four independent free parameters are usually represented by three real Euler angles and a single complex phase. The three rotation angles are referred to as mixing angles and the complex phase allows for CP violation.

The current measured bounds on the CKM elements are shown in Table 2.4 [3]. This table also shows popular experimental channels for extracting these elements.

2.2.2 Parameterization of the CKM Matrix

As we can see from Table 2.4, the diagonal of the matrix is highly favored with interaction magnitudes of close to one. Conversely, those elements far-

Table 2.4: Quark transitions and their strength.

Quark Transition	Strength	Method of Measurement
V_{ud}	$0.9739 - 0.9751$	Nuclear β decay
V_{us}	$0.221 - 0.227$	$\bar{K^0} \to \pi^+ e^- \bar{\nu_e}$
V_{ub}	$0.0029 - 0.0045$	$B \to \pi \ell \bar{\nu_\ell}$
V_{cd}	$0.221 - 0.227$	$D^0 \to \pi^- e^+ \nu_e$
V_{cs}	$0.9730 - 0.9744$	$D^0 \to K^- e^+ \nu_e$
V_{cb}	$0.0029 - 0.0044$	$B \to \chi_c \ell \bar{\nu_\ell}$
V_{td}	$0.0048 - 0.0014$	$B - B^0$ mixing
V_{ts}	$0.037 - 0.043$	$b \to s\gamma$
V_{tb}	$0.9990 - 0.9992$	$t \to bW$

thest from the diagonal are the most suppressed. A popular representation of the CKM matrix is the Wolfenstein parameterization [8] that clearly demonstrates this interaction magnitude hierarchy. With this paramaterization, the matrix is expanded in powers of independent parameters, λ, A, ρ, and η. In this parameterization,

$$\lambda \equiv s_{12};\ A \equiv s_{23}/\lambda^2;\ \rho - i\eta \equiv s_{13} e^{-i\delta_{13}}/A\lambda^3, \tag{2.3}$$

where s_{ij} is the mixing angle between quark generations.

We know from experiment that $\lambda \approx 0.22, A \approx 0.8$, and $\sqrt{\rho^2 + \eta^2} \approx 0.4$. With this parameterization, we obtain the Wolfenstein parameterization from the CKM matrix:

$$V = \begin{pmatrix} 1 - \frac{1}{2}\lambda^2 & \lambda & A\lambda^3(\rho - i\eta) \\ -\lambda & 1 - \frac{1}{2}\lambda^2 & A\lambda^2 \\ A\lambda^3(1 - \rho - i\eta) & -A\lambda^2 & 1 \end{pmatrix}. \tag{2.4}$$

Here η represents the CP-violating phase and, given that it is always multiplied by a factor of λ^3 and λ is a small fraction, we expect CP violation to be small in the Standard Model.

2.2.3 The Unitarity Triangle

The requirement that the CKM matrix be unitary ($V^\dagger V = 1$) leads to six relations [9]:

$$V_{ud}V_{us}^* + V_{cd}V_{cs}^* + V_{td}V_{ts}^* = 0, \tag{2.5}$$

$$V_{us}V_{ub}^* + V_{cs}V_{cb}^* + V_{ts}V_{tb}^* = 0, \tag{2.6}$$

$$V_{ud}V_{ub}^* + V_{cd}V_{cb}^* + V_{td}V_{tb}^* = 0, \tag{2.7}$$

$$V_{ud}V_{cd}^* + V_{us}V_{cs}^* + V_{ub}V_{cb}^* = 0, \tag{2.8}$$

$$V_{cd}V_{td}^* + V_{cs}V_{ts}^* + V_{cb}V_{tb}^* = 0, \tag{2.9}$$

$$V_{ud}V_{td}^* + V_{us}V_{ts}^* + V_{ub}V_{tb}^* = 0. \tag{2.10}$$

These expressions can be represented as six triangles in the complex plane, all with the same area, i.e., half of the Jarlskog invariant, J [10], which is a phase-convention independent measure of CP violation, $\mathrm{Im}[V_{ij}V_{kl}V_{il}^*V_{kj}^*]$. All but two of the triangles are long and thin. However, those two relations yield

triangles with approximately equal sides, each side on the order λ^3. Taking the relation in equation 2.7,

$$V_{ud}V_{ub}^* + V_{cd}V_{cb}^* + V_{td}V_{tb}^* = 0, \tag{2.11}$$

we can form the triangle known as the Unitarity Triangle (see Figure 2.1). If one aligns $V_{cd}V_{cb}^*$ with the real axis and divides by its magnitude $|V_{cd}V_{cb}^*|$, we arrive at the rescaled Unitarity Triangle.

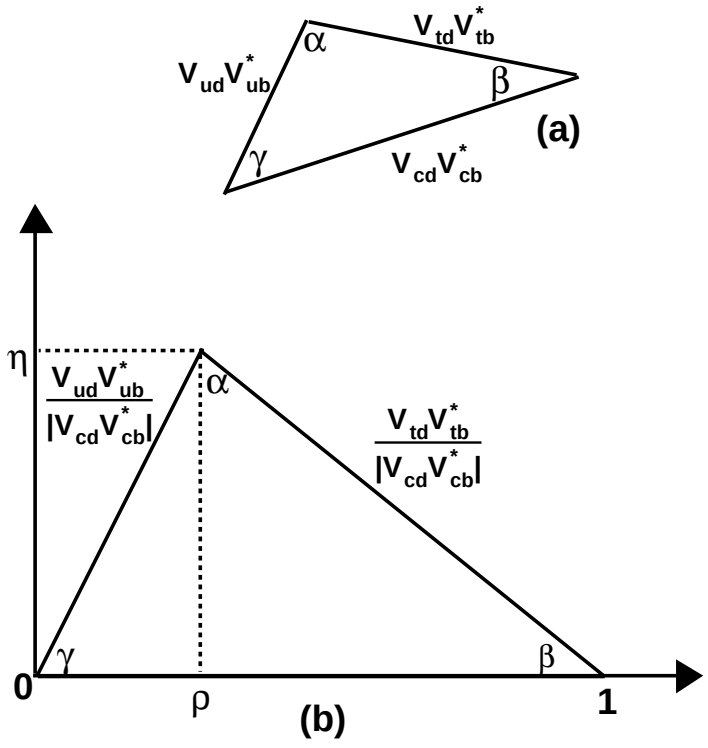

Figure 2.1: (a) The Unitarity Triangle; (b) the Unitarity Triangle rescaled, all sides divided by $|V_{cd}V_{cb}^*|$.

In doing this, one side of the triangle is of unit length and lies along the real axis in the (ρ, η) complex plane. Thus, the points of the triangle are at (0,0), (1,0), and $(\bar{\rho}, \bar{\eta})$ where $\bar{\rho}, \bar{\eta}$ are defined as

$$\bar{\rho} + i\bar{\eta} \equiv -\frac{V_{ud}V_{ub}^*}{V_{cd}V_{cb}^*}, \tag{2.12}$$

$$\bar{\rho} = \rho(1 - \lambda^2/2), \bar{\eta} = \eta(1 - \lambda^2/2). \tag{2.13}$$

Using these relations, we can express the angles of the triangle as

$$\alpha = \tan^{-1}(\frac{\bar{\eta}}{\bar{\eta}^2 + \bar{\rho}(\bar{\rho} - 1)}), \beta = \tan^{-1}(\frac{\bar{\eta}}{1 - \bar{\rho}}), \gamma = \tan^{-1}(\frac{\bar{\eta}}{\bar{\rho}}). \tag{2.14}$$

The Unitarity Triangle provides a clear picture of the CKM mechanism. Experimentally, we can measure the sides of the triangle and its angles, and within the confines of the Standard Model, the sides of the triangle should 'close'. Should the triangle not close, that would be a clear indication of physics beyond the Standard Model. Thus, great efforts have been made to precisely measure each CKM matrix element to constrain the possibilities of new physics.

2.3 Semileptonic B Decays

This thesis will describe the measurement of the branching fraction of the decay of a B_s^0 meson to an orbitally excited D_s meson. Thus, before this

measurement can be addressed, it will be necessary to describe the concept of a semileptonic B decay.

A B meson is a meson that contains a b quark in a bound state with another anti-quark. The family of B mesons consists of the B^+ ($\bar{b}u$), B^0_d ($\bar{b}d$), B^0_s ($\bar{b}s$), and B^+_c ($\bar{b}c$) as well as their anti-particle conjugates. Note that the bottom quark does not form mesons with the top quark since the top quark has too short a lifetime to form mesons.

When considering a B-meson decay, it is instructive to first begin with the simple case in which the bare b quark decays as shown in Figure 2.2.

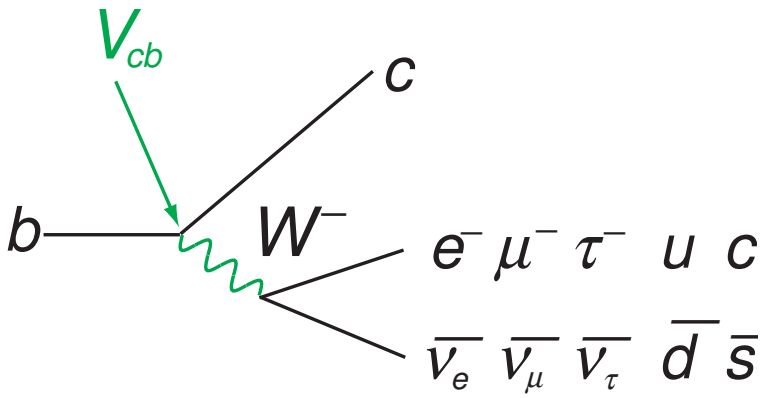

Figure 2.2: Simple bare-quark quark model of B^0_s decay.

In the case of the semileptonic decay of the b, the b quark decays weakly, emitting a W^- boson, into a c quark. The W^- boson subsequently decays into a muon plus a neutrino. In the bare-quark model, one can make a naive estimate of the $b \to c\mu\nu$ branching fraction. To calculate the total decay

width of $b \to c$, one needs to look at all the possible decay products of the W:

$$\begin{aligned} W &\to e\nu \\ W &\to \mu\nu \\ W &\to \tau\nu \\ W &\to ud\,(\times 3 \text{ colors}). \\ W &\to cs\,(\times 3 \text{ colors}) \end{aligned} \tag{2.15}$$

Making the naive assumption that all decay products have the same mass, one can make a rough estimate of the branching fraction:

$$Br(b \to c\mu\nu) \sim Br(W \to \mu\nu) = \frac{1}{1+1+1+3+3} = \frac{1}{9} = \ 11\% \tag{2.16}$$

Of course, the bare-quark model ignores the fact that the quarks interact within mesons. For example, in the decay $B_s^0 \to D_s^{**}\mu\nu$, the naive model begins with a s quark in a bound state with a $\bar{b}$ quark. This model of this decay assumes that the s quark spectates while the b quark decays into a charm, with the c quark then forming a bound state with the strange quark (Figure 2.3). The reality of the situation, of course, is not this straight forward. In an actual semileptonic B decay, there is gluon exchange since the b and s quarks are in a bound state (Figure 2.4).

Given that this complicates the situation significantly, it is necessary to develop a model to deal with both the gluons and the light quarks. To handle

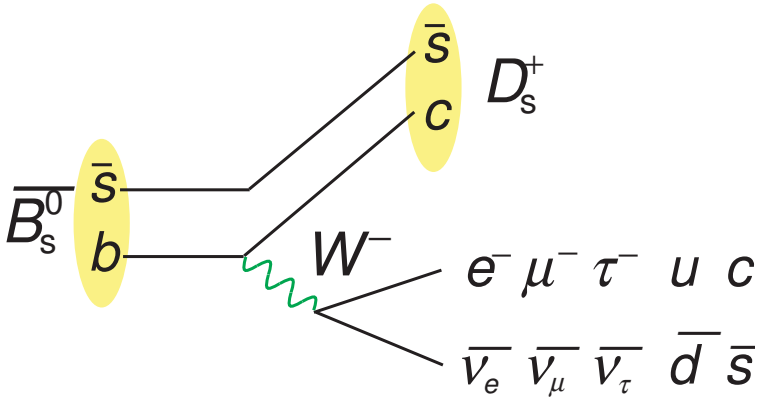

Figure 2.3: Model of B_s^0 decay with strange quark spectating.

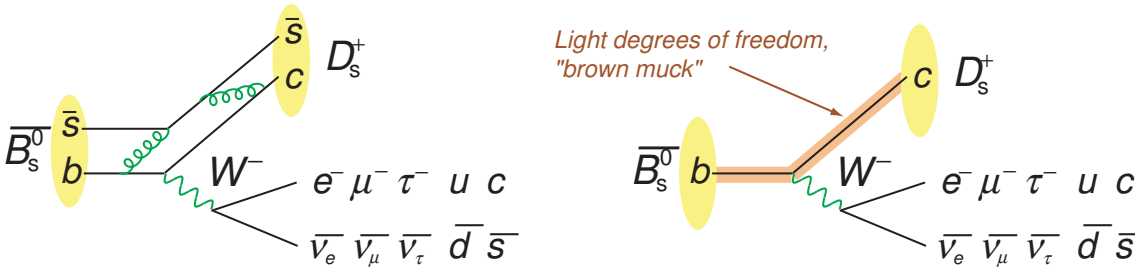

Figure 2.4: More realistic quark model of B_s^0 decay with gluon exchange.

such decay, Heavy Quark Effective Theory (HQET) was developed. In this theory, the light quark and the gluons can all be lumped together as the 'light degrees of freedom' and can be considered separately from the heavy (b or c) quark. Heavy Quark Effective Theory will be further discussed in Subsection 2.5.1.

2.4 Constraining the Unitarity Triangle with semileptonic B decays

Before leaving the idea of the Unitarity Triangle and delving into Heavy Quark Effective Theory, we can now return to the idea of constraining the Unitarity Triangle from the perspective of semileptonic B decays [11]. The most precise measurement of the matrix element V_{cb} can be made with inclusive or exclusive $b \to c\ell\nu$ decays. However, the difficulty in determining V_{cb} from exclusive $B \to D^{(*)}\ell\nu$ decays lies in the need for knowledge of the $D^{(*)}$ form factor, i.e., the structure function used to describe the probability density for a hadron. These form factors are non-perturbative quantities which need to be calculated using, for example, lattice QCD or QCD sum rules.

However, the semileptonic width $\Gamma(B \to X_c\ell\nu)$, where X_c represents any c quark meson can be calculated using a simultaneous expansion of $\alpha_s(m_b)$ and Λ_{QCD}/m_b within the framework of Heavy Quark Effective Theory. The parameters that cannot be extracted perturbatively can, in this case, be extracted by measuring moments of lepton energy or hadronic invariant mass.

2.5 Heavy Quark Effective Theory

The following discussion of Heavy Quark Effective Theory follows the treatment in Ref. [12].

2.5.1 Basis of Heavy Quark Effective Theory

Heavy Quark Effective Theory (HQET) [12, 13, 15] is a theory that is applicable in the situation where one of the constituent quarks is heavy and the other(s) is (are) light. It is in the case where $m_Q \gg \Lambda_{QCD}$, where m_Q is the mass of the heavy quark and Λ_{QCD} is the scale of the constituent mass of a light quark (i.e., ≈ 200 MeV/c^2). Quarks with larger mass include top, bottom, and charm. Top, however, is actually too heavy and decays too quickly to form hadrons and so this theory does not apply to the top quark. In this limit, the heavy b or c quark is taken to have infinite mass and can be considered to be at rest in the frame of the particle.

The heavy quark can be pictured to be surrounded by a cloud consisting of the light quarks and gluons often referred to as the 'brown muck.' While the calculation of the properties of this cloud is difficult, in the heavy quark limit the 'muck' has properties that are essentially independent of the heavy quark. The reason for this is that strongly interacting particles have an effective radius of approximately $\frac{1}{\Lambda_{QCD}} \approx 1$ F which puts Λ_a at approximately 200 MeV. The distance scale that light quarks can resolve is the approximate radius of the hadron. The Compton wavelength of the heavy quark is given by $\lambda_Q \approx \frac{1}{m_Q}$ and so, as the mass of the bottom and charm quark is well above 200 MeV, the heavy quark mass sets a distance scale much below the $\frac{1}{\Lambda_{QCD}}$ distances which the brown muck can resolve. Basically, the heavy quark and the light degrees of freedom operate on different distance scales which

allows us to separate the physics for the two cases. The light quarks are thus independent of the flavor and spin of the heavy quark and only depend on the color field. The reason for the lack of dependence on the spin of the heavy quark is that the spin couples through a 'color magnetism' term, a relativistic term proportional to $\frac{1}{m_Q}$ and thus, given that the heavy quark is considered at rest in the rest frame of the particle, relativistic effects are not considered and the spin decouples.

Given that the light quarks are independent of the type of heavy quark, many relations can be drawn between hadrons containing the same light quarks but different heavy quarks. The natural analogy to draw here is with the atom, where the nucleus is analogous to the heavy quark and the brown muck is paralleled by the electron cloud. Within atomic physics, different isotopes will share the same properties despite having different nuclear masses. To first order, the atomic wavefunction is independent of nuclear mass as the nuclear spin decouples from the electron cloud in the limit that $\frac{m_e}{m_N} \to 0$. The electrons, therefore, are only effected by the overall charge of a nucleus and thus properties are shared between isotopes.

So it follows that in the limit where $m_Q \to \infty$, hadrons that differ only in flavor or spin quantum numbers of the heavy quark will have the same properties with regard to the light degrees of freedom. This allows us to draw comparisons between B, D, $D^{*(*)}$, and $B^{*(*)}$ mesons since the only factor affecting the light degrees of freedom is the static color charge.

The heavy quark, however, does not actually have infinite mass and thus it is necessary to apply perturbative $\frac{1}{m_Q}$ corrections to the initial approximation. HQET is based on a symmetry of an effective theory and is a good approximation of QCD within certain kinematic regions, specifically when the heavy quark interacts through the exchange of soft gluons. In such a system, the heavy quark nearly follows classic equations of motion (which is referred to as 'on mass shell') and it's momentum fluctuates around the mass shell on the order of Λ_{QCD} and these fluctuations vanish in the limit that $\frac{\Lambda_{QCD}}{m_Q} \to 0$. Within these limits, Heavy Quark Effective Theory provides a framework with which to study the corrections necessary with the heavy-quark symmetry in a systematic fashion.

QCD Lagrangian in HQET

The QCD Lagrangian for heavy quarks, $\mathcal{L}_Q = \bar{Q}(i \not{D} - m_Q)Q$, needs to be represented in a form that utilizes the limit $m_Q \to \infty$. In this relation, $\not{D} = \gamma^\mu D_\mu$ where $D_\mu \equiv \partial_\mu - ieA_\mu$ and A_μ is the gauge field. The light quark Lagrangian would then be added to this Lagrangian as the light quark degrees of freedom are separately conserved as mentioned above. This Lagrangian only includes the strong interaction; weak and electromagnetic currents will be added as external currents.

Starting with the momentum of the heavy quark, p_Q, we can assume that the heavy quark has essentially the same momentum as the hadron it resides within and thus can be represented as

$$(p_Q)_\mu = m_Q v_\mu + k_\mu = m_Q(v_\mu + \frac{k_\mu}{m_Q}). \tag{2.17}$$

We will define our effective heavy quark fields

$$h_v(x) = e^{im_Q v\cdot x} P_+ Q(x), \tag{2.18}$$

$$H_v(x) = e^{im_Q v\cdot x} P_- Q(x), \tag{2.19}$$

where $P_\pm$ is the positive component of the energy projection operator defined as

$$P_\pm = \frac{1 \pm \not{v}}{2}. \tag{2.20}$$

Thus, it follows that

$$Q(x) = e^{-im_Q v\cdot x}(h_v(x) + H_v(x)). \tag{2.21}$$

Returning to the QCD Lagrangian for a heavy quark, $\mathcal{L}_Q = \bar{Q}(i \not{D} - m_Q)Q$, we get

$$\mathcal{L}_Q = \bar{h}_v iv\cdot D h_v - \bar{H}_v(iv\cdot D + 2m_Q)H_v + \bar{h}_v i \not{D}_\perp H_v + \bar{H}_v i \not{D}_\perp h_v, \tag{2.22}$$

where $D^\mu_\perp = D^\mu - v^\mu v\cdot D$ is orthogonal to the heavy-quark velocity. Breaking down the Lagrangian, we can see that h_v corresponds to the massless degrees of freedom, H_v to fluctuations proportional to twice the heavy

quark mass, and then there are terms mixing the two fields. They correspond to pair creation or annihilation of heavy quark pair production. The heavy quark degrees of freedom can be eliminated by using the equation of motion and taking the variation of the Lagrangian with respect to $\bar{H}_v$. Doing this, one obtains:

$$(iv \cdot D + 2m_Q)H_v = i \not{D}_\perp h_v, \tag{2.23}$$

which can be solved to obtain the expression for H_v:

$$H_v = \frac{1}{2m_Q + iv \cdot D} i \not{D}_\perp h_v. \tag{2.24}$$

From this expression, we can see that H_v is, in fact, of the order $1/m_Q$ and will vanish in the heavy quark limit. Given this, we can see from the Lagrangian that the Lagrangian becomes, in the Heavy Quark limit, a function of purely the light degrees of freedom.

From this basic Lagrangian, corrections can be made to the heavy quark limit, including expansion of the Lagrangian by orders of $1/m_Q$, QCD radiative corrections, recoil corrections, and other relativistic corrections.

Semileptonic Decays in HQET

To build a framework to aid in the understanding of semileptonic decays in HQET, it is instructive to first begin with the example of the elastic scattering of a B meson. The scattering is induced by a vector current

coupled to the b quark and, in the heavy quark limit, the heavy quark acts as a static color charge for the light degrees of freedom. In this limit, the b quark moves with approximately the velocity of the B meson, v. In the case of an elastic scattering, the static color charge acts to replace the B meson moving with a velocity v with one moving at a velocity v'. Should $v = v'$, the light degrees of freedom are undisturbed, but in the case where there is a velocity change, the light degrees are now reacting to a moving color charge and must rearrange themselves accordingly leading to a form factor suppression.

Key to this example is the fact that, as $m_Q \to \infty$, the form factor can only depend on the Lorentz boost $\gamma = v \cdot v'$ and thus the transition is described by a dimensionless probability function, $\xi(v \cdot v')$. This function is known as the Isgur-Wise function [14]. Thus, we can write elastic scattering as

$$\frac{1}{m_B}\langle \bar{B}(v')|\bar{b}_{v'}\gamma^\mu b_v|\bar{B}(v)\rangle = \xi(v\cdot v')(v+v')^\mu, \tag{2.25}$$

where b_v and $b_{v'}$ are velocity-dependent heavy-quark fields. The factor of $1/m_B$ arises from the relativistic normalization of meson states, given by

$$\langle \bar{B}(p)|\bar{B}(p)\rangle = 2m_B v^0 (2\pi)^3 \delta^3(\vec{p} - \vec{p}'). \tag{2.26}$$

It is conventional to represent the above by an elastic form factor $F_{el}(q^2)$ that depends on the momentum transfer $q^2 = (p - p')^2$:

$$\langle \bar{B}(p)|\bar{B}(p)\rangle = F_{el}(q^2)(p+p')^\mu, \tag{2.27}$$

which means that $F_{el}(q^2) = \xi(v \cdot v')$. We know that $p = m_B v$ and $p' = m_B v'$ and so, if we expand out the relation $q^2 = (p-p')^2$ we find $q^2 = p^2 - 2m_B^2 v \cdot v' + p'^2$. Since $p^2 = p'^2 = m_B^2$ we finally find that $q^2 = -2m_B^2(v \cdot v' - 1)$. By conservation of current, the elastic form factor must normalize to unity, meaning that if $v = v'$, $v \cdot v' = 1$ and $\xi(1) = 1$ which makes sense as the probability of an elastic collision should equal unity if $v = v'$. The point where $v = v'$ is known as the zero-recoil limit.

The interaction of interest, however, is not the elastic case but rather the case where a B meson decays to a D meson. In the heavy quark limit, one can take advantage of the heavy quark symmetry and replace the b quark with a c quark transforming the B meson into a D meson. After this symmetry transformation, we can represent the decay probability as

$$\frac{1}{\sqrt{m_B m_D}}\langle D(v')|\bar{c}_{v'}\gamma^\mu b_v|\bar{B}(v)\rangle = \xi(v \cdot v')(v+v')^\mu. \tag{2.28}$$

Key here is the fact that this is still determined by the probability function $\xi(v \cdot v')(v+v')^\mu$. A common approach to representing the matrix element of a electroweak decay is to represent the flavor-changing current by positive and negative form factors [16],

$$\langle D(v')|\bar{c}_{v'}\gamma^\mu b_v|\bar{B}(v)\rangle = W_+(q^2)(p+p')^\mu - W_-(q^2)(p-p')^\mu. \tag{2.29}$$

Utilizing the fact that $q^\mu = (p - p')^\mu$, we can relate the above equations and find a relation for the positive and negative form factors:

$$W_\pm(q^2) = \frac{m_B \pm m_D}{2\sqrt{m_B m_D}}\xi(v \cdot v')$$
$$q^2 = m_B^2 + m_D^2 - 2m_B m_D v \cdot v' \tag{2.30}$$

Utilizing these form factors, one can make a prediction for the semileptonic decay rate of $B \to D$ and we find, in the heavy quark limit,

$$\frac{d\Gamma(\bar{B} \to D\ell\nu)}{dw} = \frac{G_F^2}{48\pi^3}|V_{cb}|^2(m_B + m_D)^2 m_D^3(w^2 - 1)^{3/2}\xi^2(w), \tag{2.31}$$

where $w = v \cdot v'$. Using similar knowledge, predictions can be made for the branching ratio $Br(B_s^0 \to D_{s1}^-(2536)\mu^+\nu X)$ and these predictions will be discussed in future sections.

2.6 HQET models

There are several HQET models that take various approaches to applying $1/m_Q$ and relativistic corrections to the standard HQET model. These models are discussed below and later compared with the results for this measurement in Chapter 6.

Isgur-Scora-Grinstein-Wise model without Relativistic Corrections (ISGW model)

The branching ratio calculated and compared with experiment in section 6 follows the method described by Isgur-Scora-Grinstein-Wise, commonly known as the non-relativistic ISGW model [17]. To calculate the decay rate for $B_S^0 \to D_{s1}(2536)\mu\nu$, the authors applied the following general expression for the decay rate of a B meson to a P-wave meson, X

$$\frac{d\Gamma(B \to X\ell^-\bar{\nu})}{dt} = \frac{|V_{qb}|^2 G_F^2}{96\pi^3 m_X^2}\{4m_B^2 S_+^2 |\vec{P}_X|^5 + (r^2 + 8m_X^2 tv^2 + 2(m_B^2 - m_X^2 - t)rS_+)|\vec{P}_X|^3 + \frac{3m_X^2}{m_B^2}tr^2|\vec{P}_T|, \quad (2.32)$$

where S_+, r, v are form factors, $\vec{P}_X$ is the three-momentum of X in the rest frame of the B meson, and $t = (p_P - p_X)^2$. The contributions of the three powers of momentum $|\vec{P}_X|^5, |\vec{P}_X|^3, |\vec{P}_X|$ means that the particle is coupled to waves of $L = 2, 1, 0$ in the final state.

In calculating the branching fractions, the value of $|V_{cb}| = 0.0402$ [18] is used and a branching fraction of 0.195% [17] is found.

This model is considered a precursor to modern HQET and does not incorporate the full Heavy Quark Symmetry, but is rather a form factor model used to model heavy quark interaction.

Isgur-Wise model with Relativistic Corrections (ISGW2 model)

Ten years after the publication of the original paper by Isgur-Scora-Grinstein-Wise, Isgur and Scora provided an update to their model which would appropriately reflect advances made in the field of Heavy Quark Symmetry [14]. It was named the ISGW2 model to reflect the fact that the model was, in fact, not a new model but rather an update to the previous ISGW model. Changes made in the update of the model include:

- heavy quark symmetry constraints on the relations between form factors away from zero-recoil;
- heavy quark symmetry constraints on the slope of form factors away from zero-recoil are built into the theory;
- relating of naive currents of quark model to full weak currents via HQET;
- heavy-quark-symmetry-breaking color magnetic interactions are included;
- modification of connection of quark model form factors to physics form factors to be consistent with heavy quark symmetry breaking at order $1/m_Q$;
- relativistic corrections are taken into account; and
- more realistic form factor shapes are employed.

Using this method, a result of $(0.53 \pm 0.27)\%$ [19] is found.

Relativistic Quark Model with $1/m_Q$ corrections

In a paper by Ebert, Faustov, and Galkin, it is found that relativistic corrections to Heavy Quark Symmetry as well as $1/m_Q$ contributions will significantly affect the calculation of branching fractions in semileptonic B decays to orbitally excited D mesons [20]. The relativistic approach taken in this paper is based on the quasipotential approach in quantum field theory. The specific choice of potential, in this case, is the quark-antiquark interaction potential. This provides a consistent approach to relativistic corrections at a given order in v^2/c^2 and also allows for a $1/m_Q$ expansion considered previously.

Previous iterations of the Relativistic Quark Model (RQM) did not include $1/m_Q$ corrections, but one can see the importance of this improvement in the calculation of the branching fraction $B_s^0 \to D_{s1}\mu\nu$ since including $1/m_Q$ corrections increases the predicted branching fraction by a factor of almost three from a previous result of 0.38% to the current prediction of 1.06%. These improvements also bring predictions for other semileptonic decays to orbitally excited states into line with previous measurements.

2.6.1 Spectroscopy in Heavy Quark Effective Theory

As discussed above, in the heavy-quark limit, the spin of the heavy quark decouples from the light degrees of freedom and thus the heavy and light systems can be considered separately. Furthermore, as the system has been

shown to not depend, to first order, on the flavor of the heavy quark, the system can be defined by the quantum numbers of the 'brown muck'.

Given the approximation within HQET that the heavy quark is at rest in the frame of the hadron, we can describe the heavy quark through the assignment of a spin quantum number, $\vec{s}_Q$. The light degrees of freedom which, following the simple hydrogen atom model of HQET, can be thought of as orbiting the heavy quark as shown in Figure 2.5, are assigned a total angular momentum $\vec{j}_q = \vec{s}_q + \vec{L}$, where $\vec{s}_q$ is the spin of the light degrees of freedom and $\vec{L}$ is the orbital angular momentum of the light degrees of freedom.

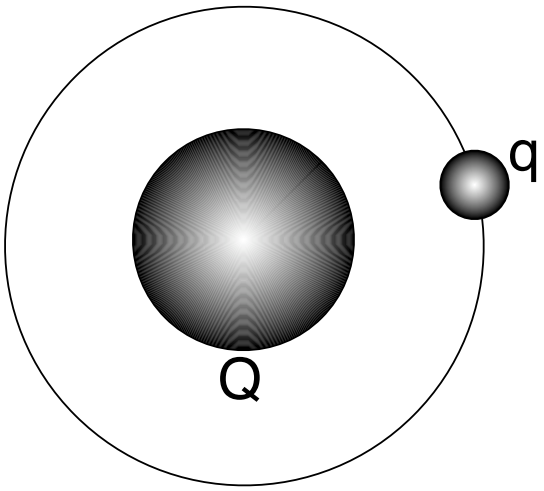

Figure 2.5: Model of a heavy quark with light degrees of freedom in the Heavy Quark Effective Theory. Q represents the heavy quark and q represents the light degrees of freedom.

It is clear, then, that in the heavy quark limit, each energy level has a

pair of degenerate states given by:

$$\vec{j}_q, \vec{J} = \vec{s}_q + \vec{L}. \tag{2.33}$$

D_s^{**} mesons are composed of a charm and strange quark in a $L = 1$ state of orbital momentum, i.e., P-wave. In the limit $m_c \gg \Lambda_{QCD}$, where Λ_{QCD} is the QCD energy scale, the quarks in this state have well defined quantum numbers, with $L = 1$ and $S = \frac{1}{2}$. Hence the total angular momentum (spin + orbital) of the light degrees of freedom can be labeled by $j_q = \frac{1}{2}$ or $\frac{3}{2}$ and the spin of the heavy quark can be taken as separately conserved. The $j_q = \frac{3}{2}$ angular momentum then combines with the heavy quark spin to form two states with $J^P = 1^+$ (D_{s1}) and $J^P = 2^+$ (D_{s2}^*). Being a $J^P = 1^+$ state, the $D_{s1}^{\pm}(2536)$ can decay only into a $D^*(J^P = 1^-)$ and K meson ($J^P = 0^-$) to conserve angular momentum and parity in a D-wave decay (relative angular momentum $L = 2$). Due to the angular momentum barrier, these states have narrow widths for decays into a D^* and a K meson.

Finally, for $j_q = \frac{1}{2}$, there are two states with $J^P = 0^+$ (D_{s0}) and $J^P = 1^+$ (D_{s1}^*). These decay via S-wave and are normally expected to have large decay widths. However, the recently discovered [21] particles, $D_{sJ}(2317)$ and $D_{sJ}(2460)$ that are usually assigned to these states are surprisingly light (compared to predictions [22]), are observed below the DK and D^*K threshold as shown in Figure 2.6 and hence also narrow. Aside from the quark-antiquark interpretation, the $D_{sJ}(2317)$ has been interpreted as a DK

molecule, a $D_s\pi$ molecule, or a four-quark state [23], although the measurement of the decay angular distribution [24] does increase the likelihood of this particle assignment and decrease the possibility of such exotic states.

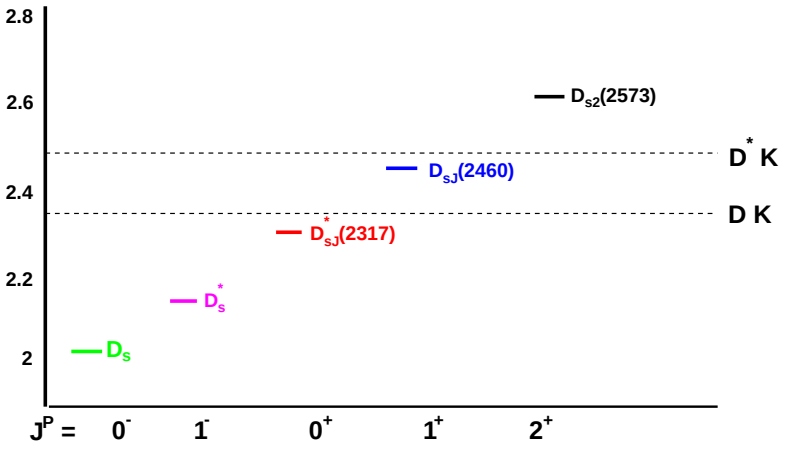

Figure 2.6: A plot of the excited D_s mesons showing their masses with respect to the DK and D^*K mass threshold.

For the excited D_s states, we get the set of degenerate pairs as indicated in Table 2.5. The state that will be studied in this analysis is the $D_{s1}(2536)$ which has both spins aligned ($s_q = +\frac{1}{2}$ and $s_Q = +\frac{1}{2}$) as well as an orbital angular momentum of $\vec{L} = 1$. All of the D_s states with $L = 1$ are collectively known as D_s^{**} or D_{sJ}, and $D_{s1}(2536)$ will often be referred to as D_s^{**} within future sections.

Table 2.5: Spectroscopy of D_s meson.

j_q	L	J	meson
$j_q = \frac{1}{2}$	$L = 0$	$J = 0$	D_s
$j_q = \frac{1}{2}$	$L = 0$	$J = 1$	D_s^*
$j_q = \frac{1}{2}$	$L = 1$	$J = 0$	D_{s0}^*
$j_q = \frac{1}{2}$	$L = 1$	$J = 1$	D_{s1}^*
$j_q = \frac{3}{2}$	$L = 1$	$J = 1$	D_{s1}
$j_q = \frac{3}{2}$	$L = 1$	$J = 2$	D_{s2}^*

2.7 Physics Motivation for this Measurement

Semileptonic B_s^0 meson decays into orbitally excited P-wave strange-charm mesons (D_s^{**}) are of interest for several reasons. They are expected to make up a significant fraction of B_s semileptonic decays and are hence important when comparing inclusive and exclusive decay rates, extracting CKM matrix elements, and using semileptonic decays in B_s^0 mixing analyses. The semileptonic B decay rate to an excited charm meson is determined by the corresponding matrix elements of the weak axial-vector and vector currents. At zero recoil (where the final excited charm meson is at rest in the rest frame of the initial B meson, see Figure 2.7), these currents correspond to conserved quantities of the heavy quark spin-flavor symmetry. For B semileptonic decays to heavier excited charm states, most of the available phase space is near zero recoil, increasing the importance of corrections in HQET. Measured decay properties can then be compared to theoretical

HQET predictions, as discussed previously.

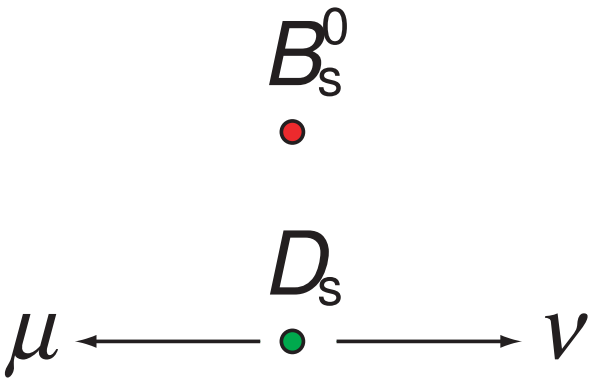

Figure 2.7: The case of zero recoil, where the charm meson is at rest with respect to the other B decay products.

Chapter 3

Experimental Apparatus

3.1 The Tevatron

The Tevatron complex [26, 27] is located at the Fermi National Laboratory approximately 45 miles outside Chicago in Batavia, IL. Currently, The Tevatron is the most powerful high energy collider in the world, creating beam energies that push the limits of the particle physics frontier. Figure 3.1 provides an overview of the accelerator apparatus.

3.2 Proton Production and Acceleration

The process of making protons begins when negative hydrogen (H^-) ions are created and accelerated to 750 keV by the Cockcroft-Walton Pre-Accelerator. From there, they are transferred to the linear accelerator (Linac) where the energy is boosted to 400 MeV. These ions are then passed onto the Booster, but not before the H^- ions pass through a carbon foil which

strips them of their electrons, leaving only a proton. This pure proton beam will then reach an energy of 8 GeV before moving onto the next stage of acceleration, the Main Injector.

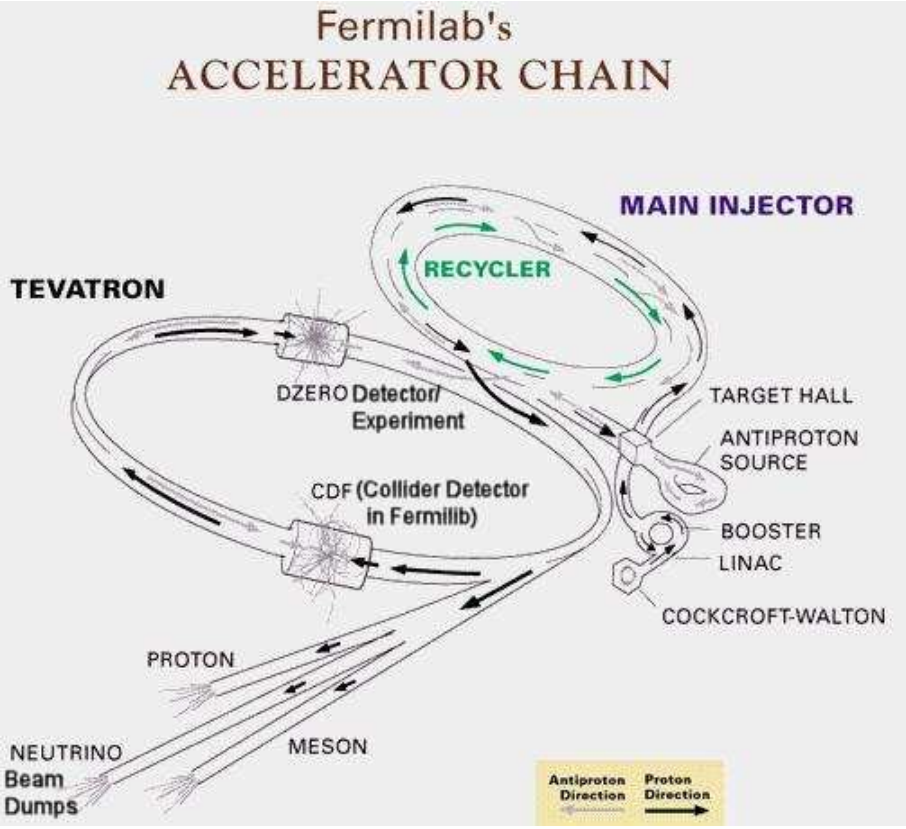

Figure 3.1: The Fermilab accelerator complex.

3.2.1 The Main Injector and Recycler

The Main Injector's [28] purpose is twofold. It accelerates protons to 150 GeV while collecting them into bunches as well as accelerating protons

to 120 GeV for passing onto the Antiproton Source. The Main Injector was one of the major upgrades for Run II as it is capable of delivering three times as many protons to the Tevatron as the Main Ring from Run I. Run I is defined as the data taking period between 1992 and 1996, while Run II is defined as the period of operation after upgrades to the Tevatron were put in place during a shutdown period from 1996 to 2001.

The protons that are passed to the Antiproton Source are impacted on a nickel/copper target which results in the production of antiprotons [29]. For every one million protons that hit the target, approximately 20 antiprotons are produced. The antiprotons are then passed to the Debuncher where the momentum spread of the antiprotons is reduced through a process known as stochastic cooling. Then, the antiprotons are passed to the Accumulator where they are stored until a sufficient number of antiprotons are built up to be transferred to the Recycler. The Recycler is a 8 GeV permanent magnet ring which acts as both a storage ring for accumulating antiprotons and a collection point for uncollided antiprotons from a previous store that are then passed onto the Main Injector and then into the Tevatron in bunches.

3.2.2 The Tevatron

The bunch configuration in the Tevatron beam typical consist of 36 bunches of protons and 36 bunches of antiprotons with a 396 ns spacing between each bunch. The number of protons in each bunch is approximately

$N_p \sim 2.7 \times 10^{11}$ while the antiprotons bunches have on order $N_{\bar{p}} \sim 5 \times 10^{10}$.

The protons and antiprotons enter the Tevatron at an energy of 150 GeV and are accelerated around the ring (which measures approximately 3.7 miles in circumference) in opposite directions to an energy of 980 GeV in a 4 T field in superconducting dipole magnets. The protons and antiprotons collide at a center-of-mass energy of 1.96 TeV at 6 different points along the ring including DØ and BØ (the location of the CDF detector).

The instantaneous luminosity at the beginning of a store is typically on the order of 2×10^{32} cm^{-2}s^{-1}. A store is a continuous colliding of proton and antiproton beams, typically lasting about 24 hours. The instantaneous luminosity is greatest at the beginning of a store and falls off exponentially during the remainder of the store.

3.3 The DØ Detector

The DØ detector [30] consists of several subsystems all working together to extract the key physical quantities from each $p\bar{p}$ collision provided by the Tevatron. Constructed with an onion-like structure, each subsystem surrounds another as shown in the schematic view of the detector in Figure 3.2.

In the following sections we will discuss the DØ coordinate system, central tracking system, calorimeter, muon system, and luminosity monitor.

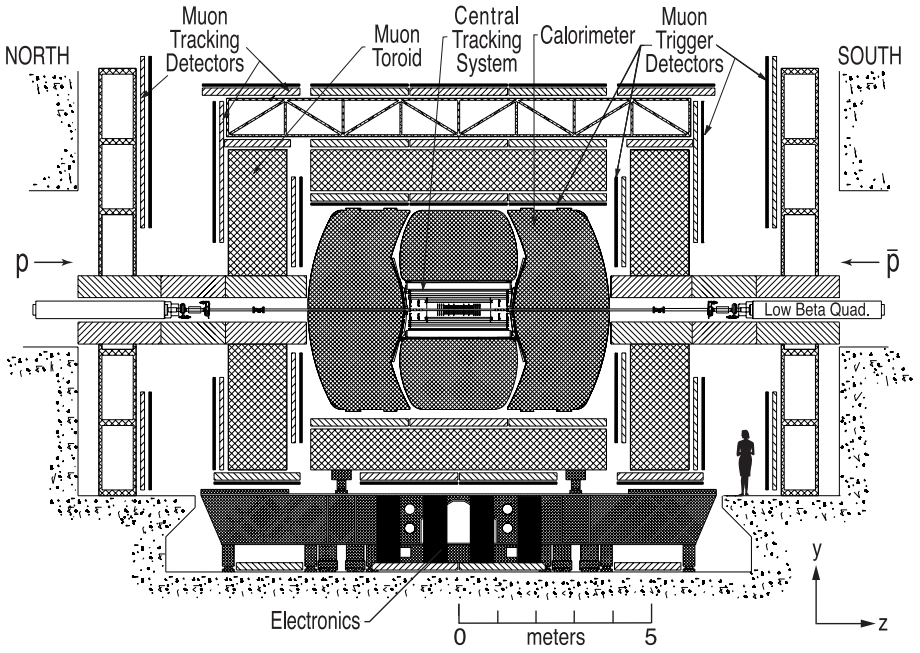

Figure 3.2: The DØ Detector.

3.3.1 The coordinate system

The DØ detector uses a right-handed coordinate system with the positive z-axis along the line of the proton beam, the y-axis upwards, and the x-axis pointing inward towards the center of the ring.

The spherical coordinates (r, θ, ϕ) are also used where the radius is the perpendicular distance from the beam line. Pseudorapidity (η) is often used in lieu of the angle θ and is defined as:

$$\eta = -\ln[\tan(\frac{\theta}{2})], \tag{3.1}$$

which approximates, in the high energy limit, the true rapidity as defined by:

$$y = \frac{1}{2}\ln\left(\frac{E + p_z}{E - p_z}\right). \tag{3.2}$$

3.3.2 Central Tracking System

The central tracking system is comprised of the silicon microstrip tracker (SMT) and the central fiber tracker (CFT) as shown in Figure 3.3.

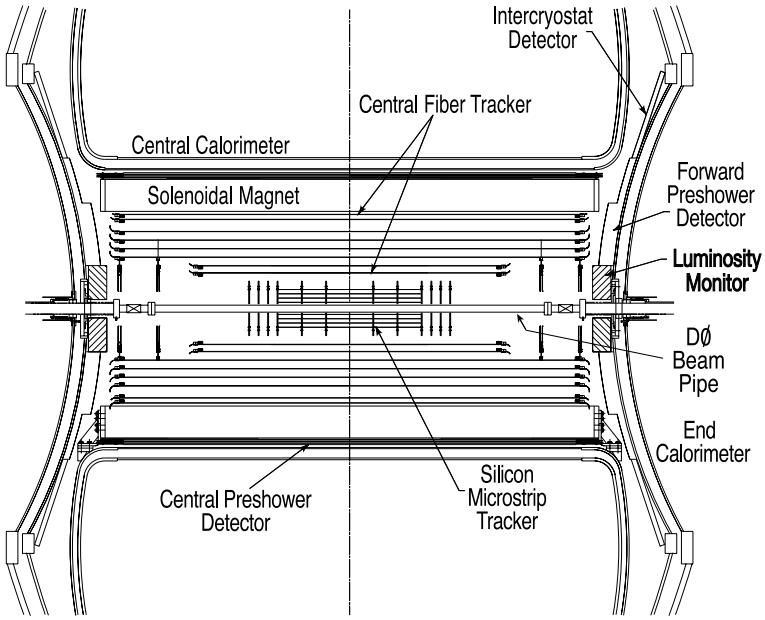

Figure 3.3: Schematic drawing depicting the DØ tracking system.

These trackers are surrounded by a 2 T superconducting solenoid. The goals of the tracking system include: measurement of particle momentum us-

ing the magnetic field, electron identification (e/π separation by comparing energy deposits with measured momentum), position tracking over a large range of pseudorapidity ($\eta < 3$), secondary vertex identification, and hardware track triggering.

Silicon Microstrip Tracker

The first layer of the tracking system going out from the interaction point is the silicon microstrip tracker (SMT) (see Fig 3.4), which is the precision tracking component of the tracking system, capable of measuring position with a resolution on the order of 10 μm.

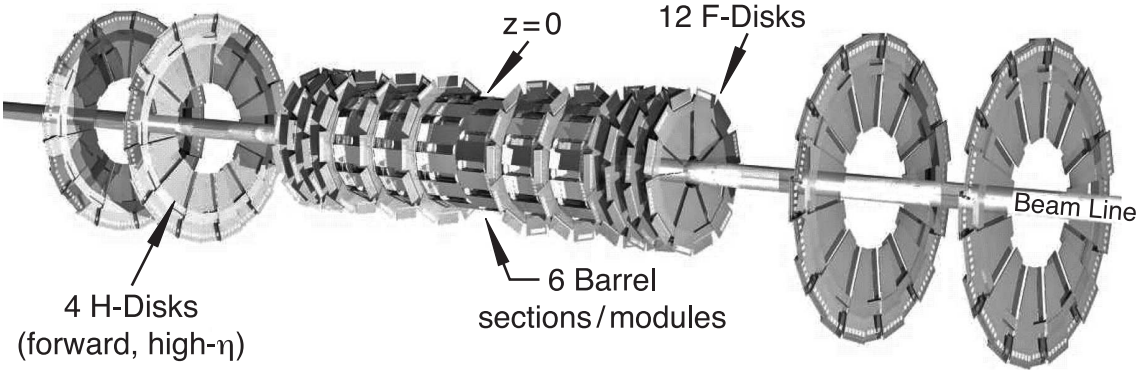

Figure 3.4: Schematic of the silicon microstrip tracker.

The SMT length is due to the length of the interaction region ($\sigma_z \sim$ 25 cm), but due to this length, it is a challenge to arrange detectors such that tracks are generally perpendicular to the detector surfaces for the full range of pseudorapidity. To resolve this, the SMT consists of a combination

of barrels and disks, with the barrels measuring primarily the $r-\phi$ coordinate and the disks measuring $r-z$ and $r-\phi$. This allows for three-dimensional reconstruction of vertices at high η by the disks and reconstruction of vertices at small η in the barrels and CFT.

The SMT detector has six 12 cm long barrels each with four silicon readout layers. Installed on these readout layers are silicon modules called 'ladders'. Layers 1 and 2 have twelve ladders each while layers 3 and 4 have 24 ladders each for a total of 432 ladders as shown in Figure 3.5.

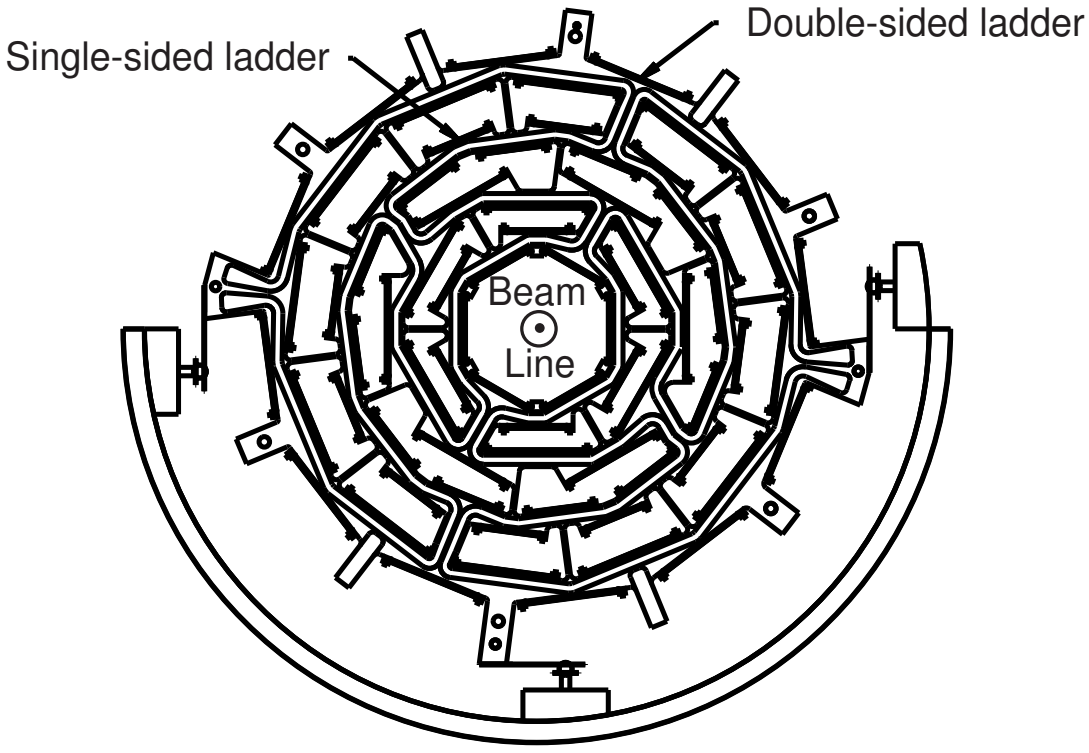

Figure 3.5: Cross section of SMT barrel.

In the four central barrels, layers 1 and 3 are double-sided with axial strips on one side and 90° stereo angle strips on the other. The two outer barrels are single-sided detectors with only axial strips. In layers 2 and 4, the barrels are double-sided detectors with axial and 2°-stereo strips. In addition to barrels, there are also 12 'F' disks and 4 'H' disks. The F disks are double-sided detectors with +15° stereo angle on one side and −15° on the other. Each F disk has an inner radius of 2.6 cm and an outer radius of 10 cm. Of the 12, 4 of the F disks are interspersed between barrel segments with the remaining 8 disks located at the end of each barrel. The 4 H disks, located in the far forward regions at $|z| = 110$ cm and $|z| = 120$ cm, are also double sided detectors with ±7.5° stereo angle. In total, the SMT consists of 912 readout modules with 792,576 channels, detailed in Table 3.1.

The SMT is read out by 128-channel SVXIIe chips. These chips are mounted on High Density Interconnect (HDI) boards and data is relayed to sequencer boards through adapter cards and interface boards. The data is then sent to the data acquisition system via a fiber optic link. The SMT provides single-hit resolutions of approximately 10 μm.

Central Fiber Tracker

The next subdetector out from the SMT is the central fiber tracker (CFT). The purpose of the CFT is primarily to combine with the SMT in track reconstruction and momentum measurement in the $|\eta| < 2$ region. Additionally, the CFT is an essential tool for providing fast track triggering in the $|\eta| < 1.6$

Table 3.1: Summary of the silicon microstrip detector.

	Barrels	F-Disks	H-Disks
Channels	387072	258048	147456
Modules	432	144	96
Silicon Area	1.3 m^2	0.4 m^2	1.3 m^2
Inner Radius	2.7 cm	2.6 cm	9.5 cm
Outer Radius	10.5 cm	10.0 cm	26 cm

region.

The CFT is comprised of scintillating fibers mounted on 8 concentric cylinder supports with a doublet layer of fibers oriented parallel to the beam axis mounted on each support. Additionally, mounted on alternating cylinders is an additional doublet layer oriented at a 2° to 3° stereo angle. A cross section of the CFT is shown in Figure 3.6.

The radii of the supports range from 20 to 52 cm from the beamline. The scintillating optical fibers are composed of a polystyrene core covered with a layer of acrylic cladding which is in turn coated with a layer of fluoro-acyrlic cladding. Each layer of cladding is 15 μm thick. The polystyrene is doped with 1% paraterphenyl which helps increase light yield and 1500 ppm 3-hydroxyflavone which shifts the scintillation light wavelength to 530 nm, the ideal wavelength for transmission in polystyrene. The fibers have a diameter of 835 μm and have lengths anywhere from 166 to 252 cm. In total, there are 76,800 scintillating fiber readout channels.

The fibers are then abutted to clear fiber waveguides (fabricated at Indiana University) that transports the scintillation light to a photodetector called a Visible Light Photon Counter (VLPC). The VLPCs are arsenic-doped silicon-avalanche devices capable of converting visible light into an electrical signal. The VLPCs operate with a high quantum efficiency ($\sim$ 80%), have large gains (22,000 to 65,000), low noise, a resolution of ~ 100 μm, and read out over 78,000 separate channels. These detectors operate at temperatures of $8 - 10^{\circ}$ K and are capable of resolving single photons as shown in Figure 3.7. The CFT provides a single-hit resolution of approximately 110 μm.

The Solenoid

For Run II, a 2 T solenoid magnet has been added to allow for the determination of the momentum of charged particles. The size dictated by the available space in the central calorimeter void is 2.73 m long with a 1.42 m diameter and it consists of two layers of 0.848 mm superconducting coil, operating at a temperature of 4.7 K with a current of 4749 A. The magnetic field has been measured to be uniform within 0.5%.

3.3.3 Preshower Detector

The preshower detector consists of two parts, the central preshower detector (CPS) and the forward preshower detector (FPS). The preshower detectors aid in the identification of electrons, enhance track matching between

hits in the calorimeter and tracking detectors, and help correct for energy loss in material upstream from the calorimeter. Location of the preshower detectors is shown on Figure 3.3.

The CPS consists of three concentric layers of triangular scintillator strips with a wavelength shifting fiber (WLS) embedded in the center of each strip. The WLS transfers light from the scintillators to waveguides and then that light is transferred to VLPCs in a manner very similar to that of the CFT readout. The FPS is very similar to the CPS, with two layers of two planes of scintillator strips located at different z positions. The two layers are separated by lead-stainless-steel absorber except for the region $1.5 < |\eta| < 1.65$ where the FPS lies in the shadow of the solenoid magnet coil and thus requires no additional absorber. Figure 3.8 shows the layout of both the CPS and FPS.

3.3.4 Calorimeter

The calorimeter plays a principle role in the measurement of particle energy. It provides a measure of electron, photon, and jet energy independent of a central magnetic field and also assists in particle identification while providing the transverse momentum balance ('missing E_T') in an event.

The DØ calorimeter, shown in Figure 3.9 is a sampling calorimeter, meaning that only a portion of the calorimeter outputs a signal. A sampling calorimeter utilizes both a high density material to cause energy loss and an active medium to generate a signal. The DØ calorimeter uses a combination

of nearly pure depleted uranium and copper for the absorption material. For the active medium, ionization due to showering particles in liquid Argon is used to produce the electric signal.

The principle upon which all calorimeters work is that particles lose energy through interacting with matter. This energy loss can be caused either through an electromagnetic interaction or a strong force interaction. For electrons, energy loss occurs through the electromagnetic interaction. Depending on the incident energy, the electrons will either lose energy via ionization ($E_e < 10$ MeV) or brehmsstrahlung ($E_e > 10$ MeV). Electrons that undergo brehmsstrahlung will emit a photon that will generally produce electrons and positrons through pair production. These electrons and positrons will, in turn, produce more photons which also pair produce and the end result is the 'shower' of an electromagnetic interaction within the calorimeter.

Hadrons interact through an inelastic collision with the nucleus of the absorption material, causing the emission of additional hadrons which themselves then undergo collisions with nuclei. The end result of this chain reaction is a situation analogous to that of the electromagnetic shower where we get a cascade of hadronic particles. However, while electromagnetic radiation tends to have a relatively short radiation length, the nuclear equivalent of radiation length tends to be much larger. Thus, hadronic showers tend to be more extended in the calorimeter than electromagnetic showers.

The calorimeter consists of three sections: the Central Calorimeter (CC),

which covers the region $|\eta| < 1.0$, and two Endcap Calorimeters (EC) positioned on either end of the CC, covering $1.0 < |\eta| < 4.0$. All sections of the calorimeter have three types of modules: an electromagnetic section (EM), a fine hadronic calorimeter (FC), and a coarse hadronic calorimeter (HC). The EM utilizes thin plates of nearly pure depleted uranium for absorption, the FC uses thicker plates of a uranium-niobium alloy, and the HC used relatively thick plates of copper or stainless steel. For each segment, liquid Argon is used in between these plates as an active material for transmitting the signal through ionization of atoms by charged particles. A schematic of a typical calorimeter cell is shown on Figure 3.10.

The position resolution of a particle passing through the calorimeter is determined by the size of the cells. For the EM, which is divided into 4 layers, most of the the cells are divided into a coarse segmentation (0.1×0.1 in $\eta \times \phi$ space) except for the third layer which has a finer segmentation (0.05×0.05) since this is the layer where the electromagnetic shower is expected to reach its maximum. Within the hadronic calorimeter, the FC has a segmentation of 0.1×0.1 and the CH has a segmentation of 0.2×0.2. This is demonstrated in a schematic cutaway of DØ calorimeter (Fig. 3.11).

In between the EC and CC, there are several gaps where, rather than instrumentation, particles pass through support structures. To account for energy loss in these areas, two different type of detectors are installed: the Inter-Cryostat Detector (ICD) and Massless Gaps (MG). The ICD is a single

layer of scintillating tiles mounted on the surface of the EC. The MG consists of two readout cells (consisting of signal boards and liquid argon gaps and using the cryostat walls as an absorber) installed before the first layer of uranium.

3.3.5 Muon System

Since muons only leave a minimal energy deposit in the calorimeter, a dedicated detector is required to detect muons since the inner detectors alone are ambiguous at best in this regard. The muon detector [31] is the outer-most layer of the DØ detector and, for a particle to reach the muon detector, it would be required to pass through the tracking system, the solenoid magnet, and the calorimeter. Given the muons' low energy loss in the presence of matter as compared to other particles, generally the only charged particle to reach the muon system is a muon.

The muon system consists of the central muon detector, the forward muon detector, and scintillation counters. A schematic of the muon system is shown in Figure 3.12.

The central muon detector is comprised of Proportional Drift Tubes (PDTs) and covers the pseudorapidity range $|\eta| < 1$. The forward muon system is made up of Mini-Drift Tubes (MDTs) and extends the coverage out to $|\eta| < 2.2$ and the scintillation counters are used for triggering and rejection of cosmic muons. Schematics of the PDTs and MDTs (Figure 3.13)

as well as the scintillation counters (Figure 3.14) are shown. Each section is made up of three layers, A, B, and C, where layer A is between the calorimeter and a 2 T toroid magnet and layers B and C are outside the toroid. The toroid magnet bends the muons in the r-z plance as they pass through the field, allowing for a local momentum measurement independent to that found in the tracking system. There is additional shielding surrounding the beam pipe in the forward region to reduce beam effects and limit the detector's exposure to radiation. .

Central Muon Detector

The PDTs in the Central Muon Detector are large, typically with a surface area of 2.8×5.6 m^2. Each drift tube has a wire of gold-plated tungsten strung through the center which serves as the anode and the drift tubes are filled with a gas mixture of 84% Argon, 8% CH_4 and 8% CF_4. As the muon passes through the PDT, the gas is ionized and the drift time of the electrons to the wire gives a positional resolution of the muon of 1.0 mm in the z direction. Combining the signal from multiple neighboring PDTs gives a resolution in the chamber x-y plane of between 10–50 cm, depending on how close to the readout electronics the hit is along the wire.

Forward Muon Detectors

The MDTs in the forward region are significantly smaller than the PDTs, consisting of 8 cells each measuring 9.4 mm $\times$ 9.4 mm in cross-section (see

Figure 3.15). There are 6,080 such drift tubes arranged in 6 layers, each layer consisting of eight octants. The drift tubes are filled with a gas mixture of 90% CF_4 and 10% CH_4, a mixture with a very short drift time of 60 ns, and have a 50 μm tungsten-gold wire in the center, oriented parallel to the magnetic field from the center toroid magnet. The forward muon system has a position resolution of $\sim$ 1 mm and improves the resolution for high momentum muons. The forward detector is especially important for tracks in the pseudorapidity regions between $1.6 < |\eta| < 2.0$ which do not hit all layers of the CFT.

Scintillation Counters

The scintillation counters are used both for triggering and also to reject background from muons that do not originate from the interaction point, such as cosmics. These counters are essential as, while they do not have the resolution of the drift tubes, they have a very fast response time, a quality essential to triggering. The scintillators are used in both the central and forward regions.

In the central region, the system of scintillation counters includes Aϕ scintillator counters in the A-layer and bottom of the B-layer as well as the cosmic cap and bottom counters. There are 240 counters in the cosmic cap, 136 bottom counters, and 630 in the A-layer. The A-layer Aϕ counters are 33.25 inches long in order to provide the necessary time resolution and match the length of the PDTs and has a ϕ segmentation of 4.5° to match the

CFT segmentation. The counters overlap slightly to minimize the likelihood of muons passing through cracks between counters. The cosmic cap and bottom counters also have a ϕ segmentation of 4.5° and are installed on the top, bottom, and sides along the outside of the PDT.

3.3.6 Luminosity Monitor

The luminosity monitor is used to determine the luminosity at DØ. The monitor, consisting of two arrays of twenty-four scintillator counters read out by PMTs, is mounted on the front faces of the end calorimeters at $z = \pm 140$ cm, covering a pseudorapidity of $2.7 \leq |\eta| \leq 4.4$. Schematics are shown demonstrating the location of the detectors (Fig. 3.16) and the layout of the detector arrays (Fig. 3.17). In addition to determining the luminosity, the luminosity counter also helps in the determination of the z-coordinate of the primary vertex through a measurement of the difference in arrival time for particles hitting the counters.

3.4 The DØ Trigger System

At the DØ interaction point, protons and anti-protons collide at a rate of 1.7 MHz, a rate much higher than the rate at which we can readout events and write them to tape. In addition, not all events are of physics interest and thus need to be excluded. As a result, DØ employs a triggering system which identifies interesting events in real time which can then be stored for

later analysis.

The trigger system is comprised of two hardware trigger levels and one software level, simply referred to as Levels 1, 2, and 3 (L1, L2, L3) respectively. L1 accepts the 1.7 MHz rate and, through a series of simple hardware-based decisions, provides a 2 kHz rate to L2. L2 utilizes field programmable gate arrays (FPGA), hardware engines associated with each detector, to reduce the rate to 1 kHz, and L3 uses software algorithms to finally reduce the rate to that which we can read out, 50 Hz. An overview of the DØ trigger system is shown in Figure 3.18.

3.4.1 Level 1

The L1 trigger consists of specialized hardware that provides input on each event based on whether it has features of interest. That input is passed to the trigger framework (TFW) which collects all the L1 information to determine whether that event should be passed on for further investigation. The L1 trigger provides trigger decisions in 4.2 μs with little or no downtime.

The triggers consist of information from the calorimeter, CFT, preshower detector, and muon systems, all of which combine within the TFW to arrive at one global decision. The L1 triggers are all buffered to eliminate downtime with enough memory associated with each trigger to retain data from 32 crossings. L1 utilizes 128 separate trigger bits, each bit requiring a specific combination of trigger terms using field programmable get arrays (FPGAs).

Should one of these 128 trigger bits be satisfied, the event is passed onto L2 buffers.

3.4.2 Level 2

The L2 trigger combines both detector-specific FPGA hardware engines and a global processor (L2Global) which makes a decision after testing for correlations between physics signatures in the different detector subsystems, making decisions within 100 μs.

The L2 trigger makes decisions in two stages. First, the subdetectors processors take information from the information passed by L1 and uses this information to form physical objects, including energy clusters and tracks. Second, L2Global looks for correlations across detector subsystems and events passing L2 requirements are transferred to L3 buffers. A full layout of the L1 and L2 triggers in shown in Figure 3.19.

3.4.3 Level 3 and Data Acquisition

The L3 trigger is a fully programmable, software-based trigger system. The L3 trigger system makes a limited reconstruction of events and, based on this, reduces an inputed rate of up to 1 kHz down to 50 Hz. A schematic of Level 3 and the data acquisition system that will be discussed below is shown in Figure 3.20.

The L3 stage utilizes information from the entire detector and thus re-

quires input from all subdetectors. L3 receives input from L2 and, upon receiving an L2 accept, a controller card in the subdetector VME signals a single board computer (SBC) to start gathering data from the crate and store it in memory located on the SBC. A dedicated SBC called the Routing Master collects information including event number and L1 and L2 triggers for that event and then assigns each event to a unique farm node within a processing farm of 96 nodes [32], to which each SBC should transmit the event information. The information is transferred from the SBC to the farm node via two 100 MB/s ethernet cables.

The data, after arriving at a given farm node, is processed by a software package called the Event Builder. The Event Builder will combine event fragments from all subdetectors and combine them into a format that allows the L3 trigger to make a decision regarding the event. Should all subdetectors not transmit information to the farm node within one second, the event is dropped. Between two and four L3 trigger processes are applied to the event and, should the event satisfy at least one of these criteria, the event is passed over 100 MB/s ethernet cables to the Collector, a temporary storage device. Once enough events are accumulated, the data is transferred first to a machine called the Datalogger and then finally to the Feynman Computing Center (located at Fermilab) where it is stored to tape and kept in a tape robot system.

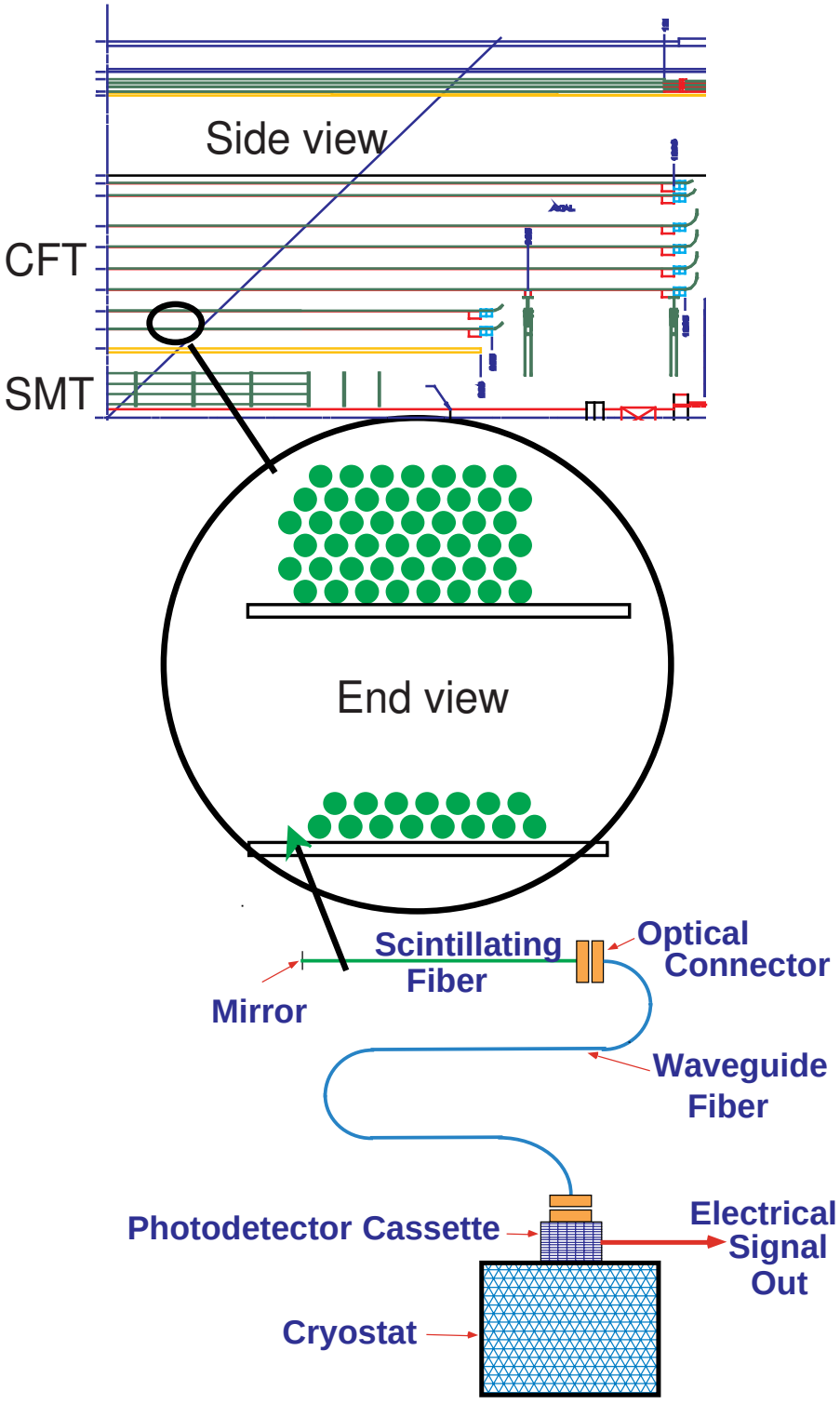

Figure 3.6: Cross section of the Central Fiber Tracker.

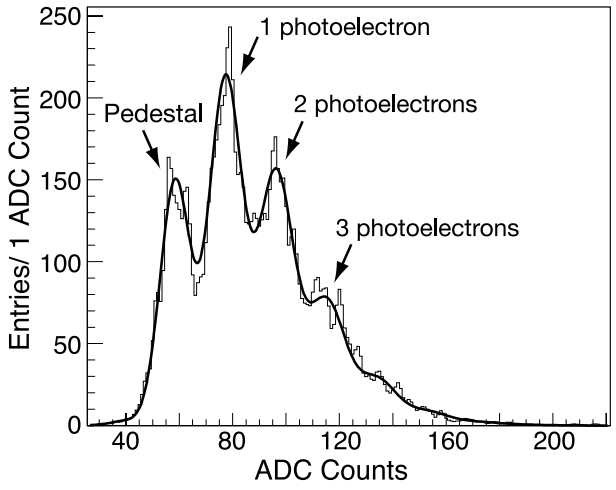

Figure 3.7: A typical LED spectrum for a single VLPC showing single photon resolution.

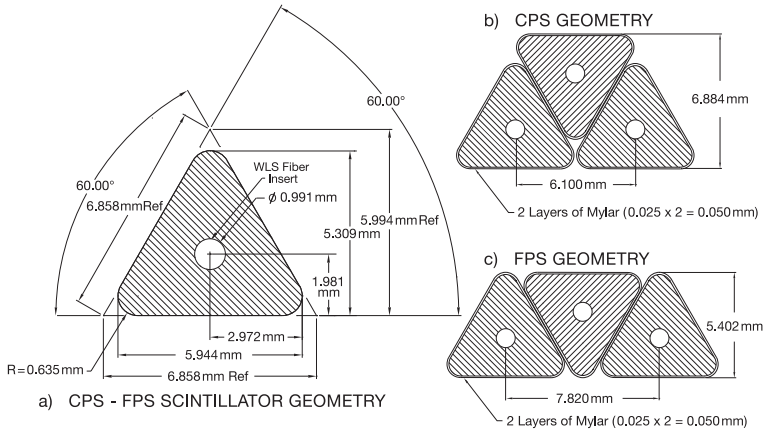

Figure 3.8: Cross section and layout of the CPS and FPS. The circles represent the location of the wavelength-shifting fiber.

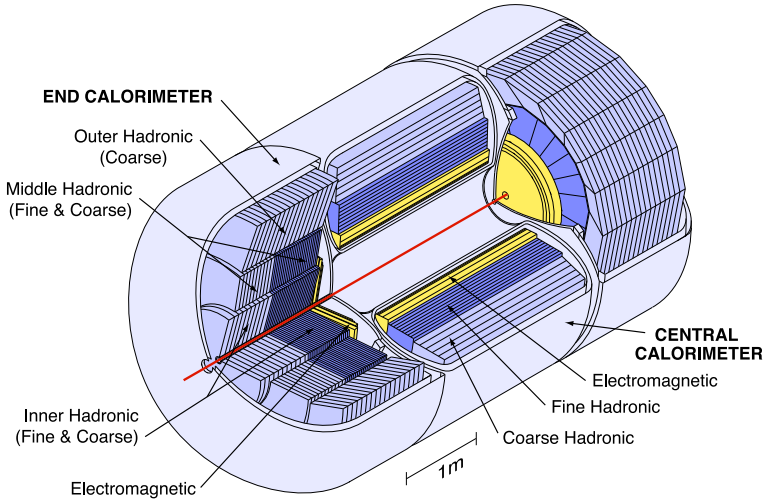

Figure 3.9: Cutaway view of the calorimeter system of the DØ detector.

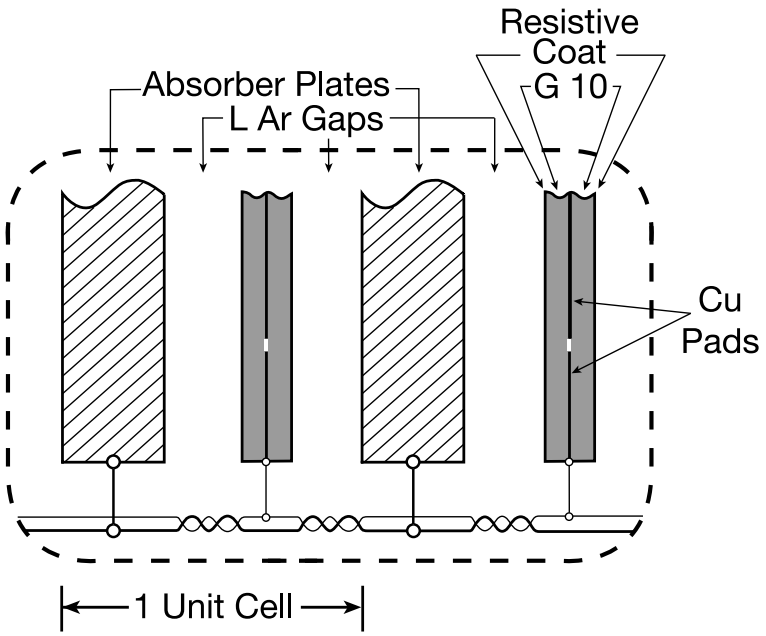

Figure 3.10: Schematic of calorimeter cell showing Liquid Argon gap and signal board unit cell.

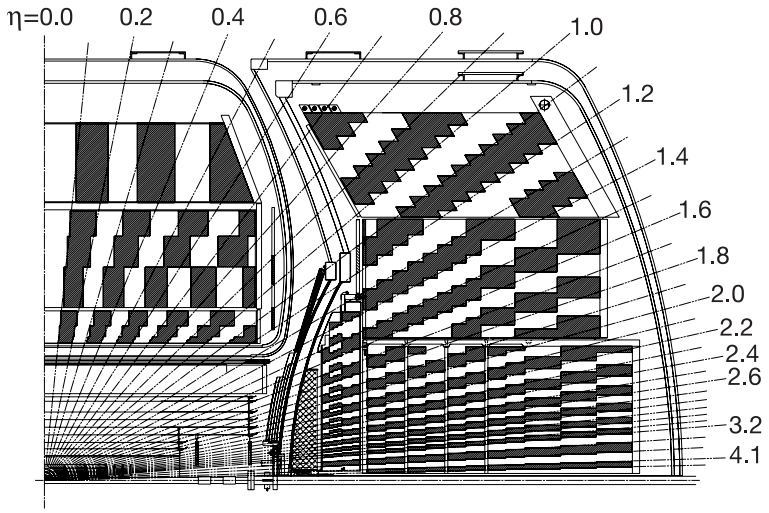

Figure 3.11: Quarter cutaway view showing segmentation pattern of calorimeter.

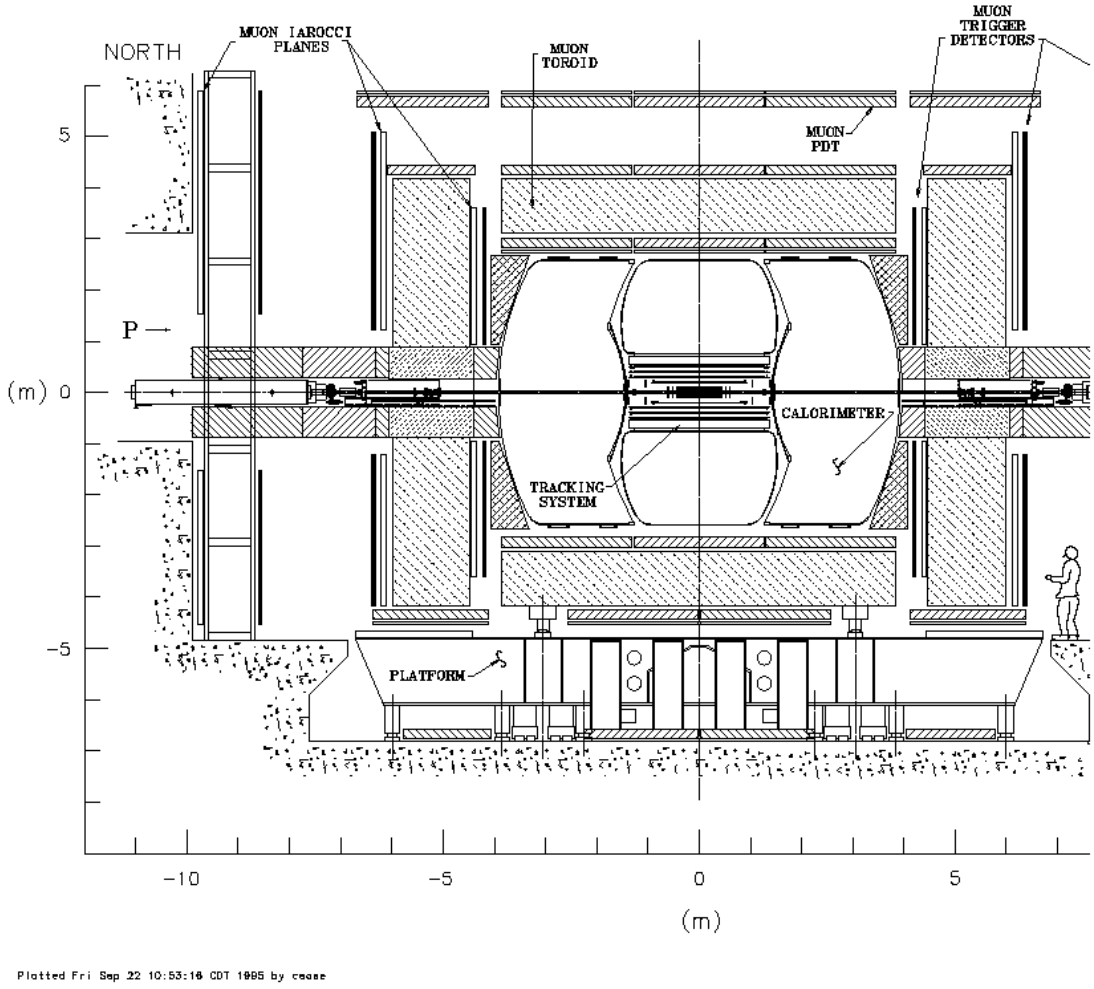

Figure 3.12: Schematic view of the muon detector.

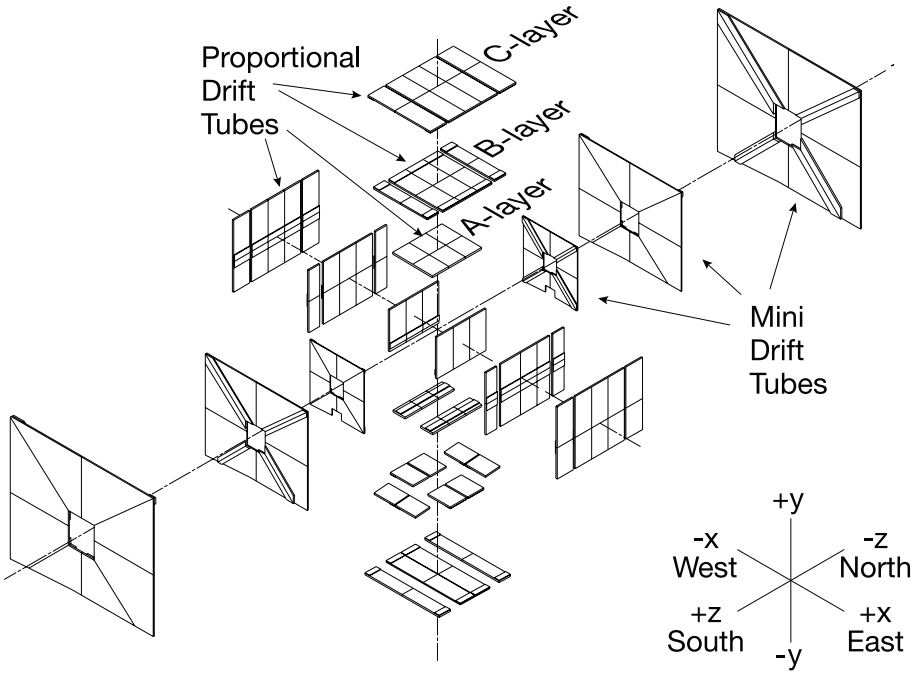

Figure 3.13: Schematic view of PDTs and MDTs.

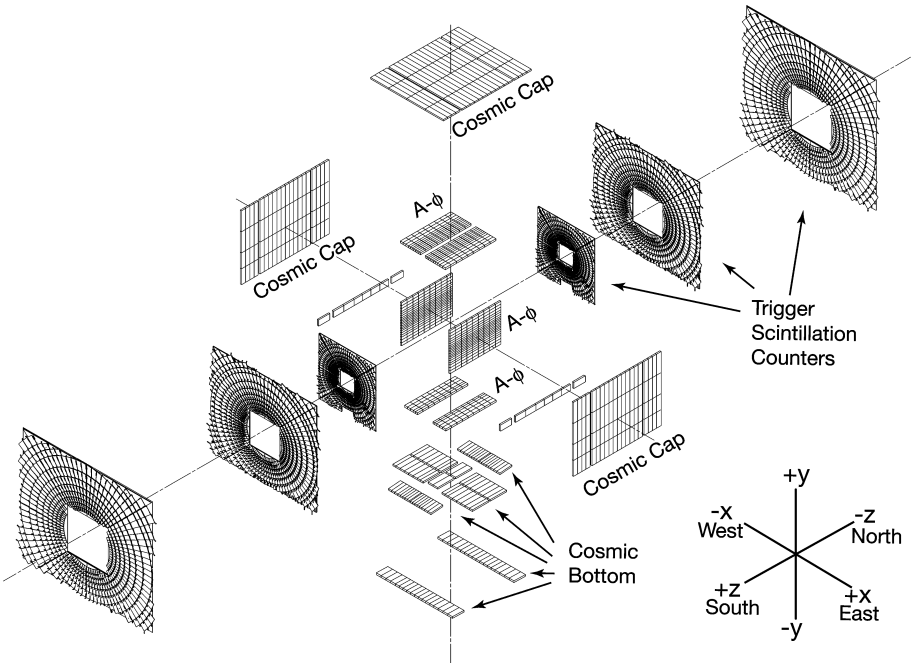

Figure 3.14: Schematic view of muon scintillation counters.

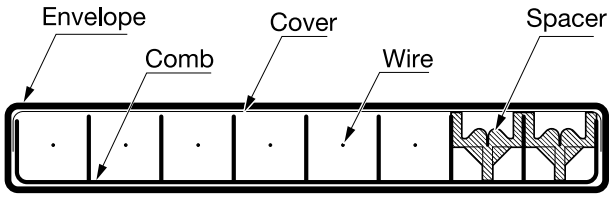

Figure 3.15: Cross-sectional view of mini drift tube.

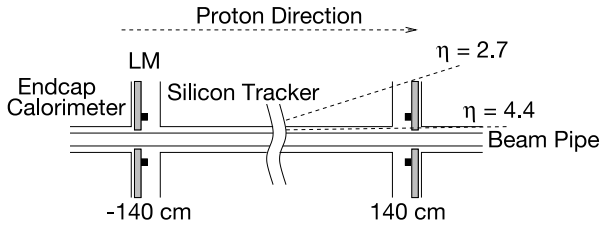

Figure 3.16: Schematic showing the location of the luminosity monitors within the DØ detector.

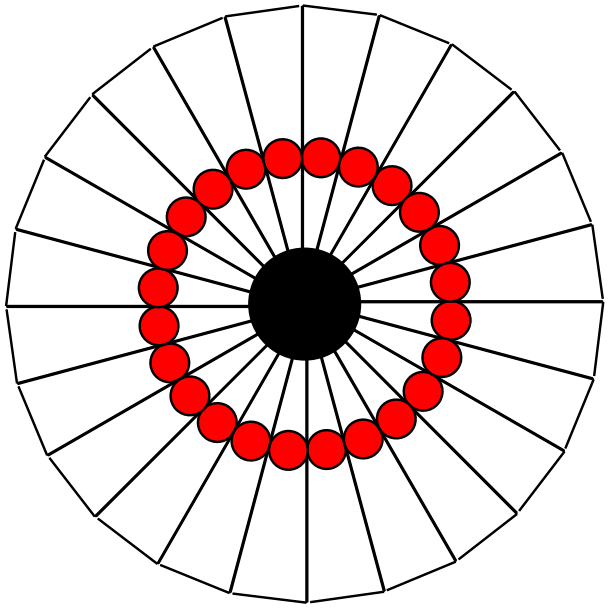

Figure 3.17: Schematic of luminosity monitor, showing scintillation counters (triangular segments) and PMTs (block dots).

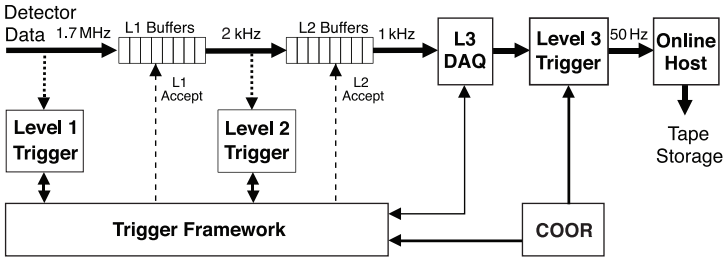

Figure 3.18: The DØ trigger system.

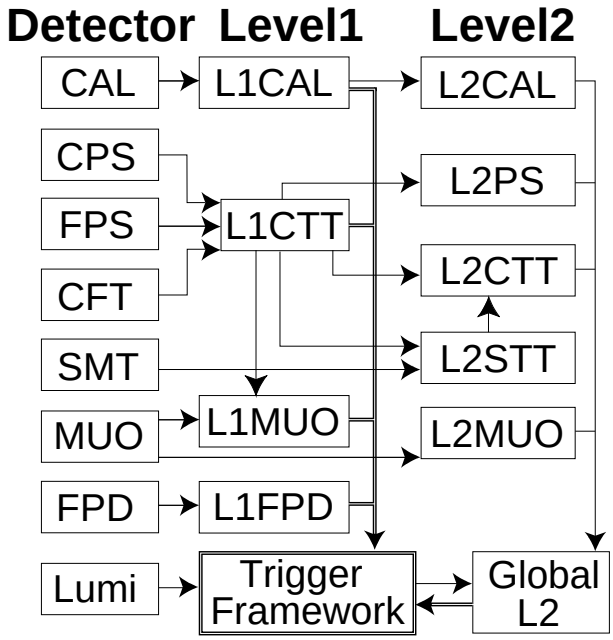

Figure 3.19: Flowchart showing the DØ Level 1 and Level 2 trigger system.

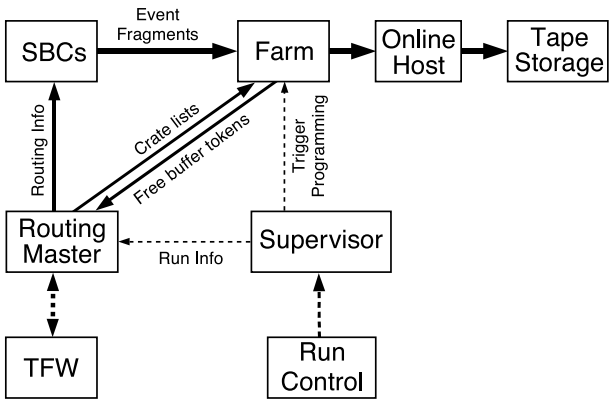

Figure 3.20: Schematic representation of L3 system and data acquisition.

Chapter 4

Event Reconstruction and Simulation

After an event is collected and stored, the next important step is to reconstruct the various energy deposits in the sub-detectors into a physics object which can then be analyzed off-line. Section 4.1 describes how particle tracks are reconstructed in both data and Monte Carlo simulation and section 4.2 discusses the generation and simulation of events in Monte Carlo samples.

4.1 Event Reconstruction

The following sections describe how tracks are reconstructed in the tracking and muon sub-systems.

4.1.1 Track Reconstruction

As a charged particle passes through a magnetic field, such as the solenoid within the DØ detector, it follows a helical path. This three-dimensional path takes the particle through various sub-detectors and various deposits of energy are left within those sub-detectors. The three-dimensional helical path of the particle is known as a track and we can reconstruct the track by examining the energy deposits left behind.

The first step in identifying a track is the identification of charge 'clusters' in the tracking system, followed by the linking of track hits using two different methods, the Histogramming Track Finding (HTF) [33] method and Alternative Algorithm (AA) [34] tracking. Finally, a global track reconstruction algorithm is used to combine tracks found using the aforementioned methods.

Track Hit Clustering

The process of clustering begins with the identification of a hit in the SMT or CFT. In the SMT, a hit is defined by the deposit of charge from an ionizing particle that is over a certain threshold (8 analog-to-digital counts). The threshold is necessary to reduce false hits from detector noise. If a hit is found in an adjacent silicon strip, the two hits are combined to begin the formation of a cluster and the process is repeated for each additional hit in an neighboring strip. The center of the hit is determined by a charge-weighted

average of the central position of each silicon strip. Within the CFT, a hit is recorded when two consecutive layered fibers record the presence of a charged particle. The position of the hit is considered to be the half-way point between the two fibers which represent the beginning and end of the cluster.

Histogramming Track Finding Method

The HTF method operates on the idea that particles which leave several hits in the transverse plane (x-y) will have both a unique curvature and azimuthal angle. Based on this, HTF method transforms hits in the x-y plane into a plane formed by the curvature ($\rho = 1/R$) and the azimuthal angle (ϕ) known as $\rho - \phi$ space. Hits from the same particle will form a peak in $\rho - \phi$ space while one expects a flat distribution from random hits. A histogram is created from this hit information and processed through a two-dimensional Kalman filter to remove noisy tracks with large track errors. This process also incorporates detector geometry and material density. This results in a set of smooth tracks. The longitudinal information is then included and the tracks are then extrapolated either out towards the CFT or back in towards to SMT depending in which system the track originated.

Alternative Algorithm Tracking

Alternative Algorithm Tracking (AA) is the reconstruction method most suited to reconstructing low-p_T B-physics tracks. To begin, the AA method

obtains track candidates using any three clusters in the SMT to form an initial track hypothesis (or a 'seed' hit) starting from the innermost layers and working outward. The algorithm then adds a second layer if the axial angle between the first and second layer is less than 0.08 rad. A third layer can then be added if the radius of an extrapolated curve drawn through the three points has a radius of greater than 30 cm (which corresponds to a $p_T \geq 180$ MeV). Also, the impact parameter with respect to the beamspot must be less than 2.5 cm and the track fit must have a $\chi^2 < 16$.

The track reconstruction then continues to the next layer of either the SMT or CFT and an expected crossing region (or 'expectation window') is computed and any track within this expectation window is tested and, should a new track be found that meets the requirements for a track match, a new hypothesis is made. If no track is found, the layer is considered a 'miss'. The misses are categorized into three different types: inside misses (misses between any two hits in a track hypothesis, forward misses, and backward misses (misses when extrapolating forward or backward, respectively). The restrictions on number of misses depends on the category of miss, with inside misses holding the most stringent requirements. This is because, were the detector 100% efficient, an inside miss would assuredly mean a fake track. For a forward or backward miss, however, there exist physical reasons for a miss (e.g. track interaction with matter for a forward miss or a track not origination from the primary vertex, such as a K_S^0 decay, for a backward

miss).

The track fit hypotheses are then ordered as follows: hypotheses with the most hits are placed first; for equal number of hits, the fewest total misses are preferred; for same number of hits and misses, the best track χ^2 is placed first. To determine the best track, the 'number of shared hits' criteria must be satisfied which is as follows:

$$N_{\text{shared}} \leq \frac{2}{3} N_{\text{total}} N_{\text{shared}} \leq \frac{1}{5} N_{\text{total}} \text{ and } N_{\text{total}} - N_{\text{shared}} < 3, \tag{4.1}$$

where N_{total} is the total number of axial clusters associated with a track candidate and N_{shared} is the number of shared axial clusters. To additionally reduce the number of fake tracks, each track with a small impact parameter with respect to the primary vertex has its hit count incremented by 2 and the track are re-ordered. The track selection process is then repeated with this new order and this helps ensure that the track candidates are associated with the primary vertex.

Finally, to improve overall efficiency, the AA method also considers tracks with CFT clusters only. In this case, the tracking starts in the innermost layer of the CFT and continues to the outermost layer of the CFT. It is required that the track extrapolated from these clusters must have an impact parameter with respect to the primary vertex of less than 1.5 cm. Then, when this track is found, the track is extrapolated to the SMT and any clusters found that can be associated with this track are kept. Allowing track finding

in this manner greatly increases the overall efficiency of the track finding algorithm.

Calorimeter Reconstruction

As a charged particle passed through the calorimeter, it ionizes the liquid argon and the collection of electrons from this ionization defines a calorimeter signal. The signal is then digitized and readout by electronics, a correction is applied to account for differences between cells, and the corrected number of counts is then converted into an energy deposit measured in GeV.

Calorimeter objects are reconstructed by forming clusters of energy deposits in neighboring cells. An EM cluster is defined as a group of towers in the calorimeter within a cone around the highest energy tower. Once the total energy is calculated, the fraction of cells from EM versus hadronic layers is used to determine whether the object is an electromagnetic or hadronic jet. Should the object be an EM object, it is identified as an electron if it is matched to a central track or a photon if there is no track match. The analysis which is the focus of this thesis does not use calorimeter information.

Muon Reconstruction

Muons are reconstructed by requiring hits in the three layers of the muon detector. Hits in both the drift tubes and scintillator are used in the reconstruction of muon tracks.

In the central region, the PDTs provide a measurement of the time it

takes for the electrons from the ionization to reach the anode (drift time) and the time from the electron hitting the wire to arrival at readout (axial time). The axial time will give a measurement of the particle position along the wire and the drift time combined with the angle of the track gives the distance perpendicular to the wire. If this information is combined with the scintillator hit position the axial resolution is improved. In the forward region, the MDTs provide a single measurement which is the sum of the drift and axial time. To extract the axial position toroid of the track, a matching scintillator hit is required. With this knowledge, the drift time can be determined and used to calculate the distance perpendicular to the wire.

Once the hits have been reconstructed, straight lines called links are formed between straight track segments that are within 20 cm of each other, are not in the same plane, and are not from the same wire hit. This process is called a linked list algorithm. Should two links be found to be compatible with a straight line the links are merged to form a new link which contains all the constituent link information. Once the track fit is made, the segment is extrapolated to a corresponding scintillator position in the plane of the wire hits. Should a scintillator hit be found, the track is refit taking into account scintillator timing.

Matching in the B and C layer is made assuming straight line segments as there is no magnetic field between these outer layers. A fit is made between these segments and, since multiple track candidates can be made with each

set of line segments, the one with the best χ^2/n_{dof} is chosen. Should a segment only have two hits, the segment most compatible with coming from the primary vertex is chosen. After the track matching in the B and C layer is complete, the A-layer segments are fit with the BC layer segments to obtain a 'local' muon track. Since the particle would have to traverse the magnetic field in the toroid between layers A and B, the fit is made to a helical path. The fit takes into account energy loss within material as well as multiple scattering at each point. This local muon track is then matched to a track within the central tracker to form a 'global' muon track.

4.2 Event Simulation

To model the DØ detector and its response to both signal and background events, Monte Carlo (MC) events are simulated as described in the following sections.

4.2.1 Event Generation

An 'event generator' is used to describe $p\bar{p}$ hard scatter events and it is used to simulate events at the four-vector level. The generator used in this analysis is the PYTHIA generator [35]. It incorporates all of the underlying physics as currently understood in the generation of events including hard and soft sub-processes, parton distribution functions, fragmentation, decays, etc. To properly simulate these properties, Monte Carlo techniques are used

to simulate quantum mechanical variations observed in nature and includes both average behavior and fluctuations.

B hadrons (and charm hadrons) created in PYTHIA are decayed in EVTGEN [36], a program especially designed for heavy flavor physics which includes all known, and in some cases, anticipated, decay modes of B mesons and their daughter particles. These decays are them filtered using `d0_mess`, a package that allows the user to select certain decay modes and also place requirements on certain kinematic properties of the particles.

In this analysis, PYTHIA is used to generate events requiring a $b\bar{b}$ pair to be produced initially in the collision with the b and $\bar{b}$ produced back-to-back (`msel`=5, see Fig. 4.1) and a 'QCD inclusive' sample where $b\bar{b}$ pairs are produced through gluon splitting as well as via direct production (`msel`=1, see Fig. 4.2). With QCD inclusive production, it is possible to produce, for example, a $u\bar{u}$ pair in the initial collision but then have one of the quarks radiate a gluon which subsequently splits into a $b\bar{b}$ pair. This kinematic signature will be different from the $b\bar{b}$ pairs generated back to back in `msel`=5 production as these $b\bar{b}$ pairs tend to be close to one another in angle. The ability to use the '`msel`=5' production is essential to speeding up production when one is not concerned about additional effects due to gluon splitting.

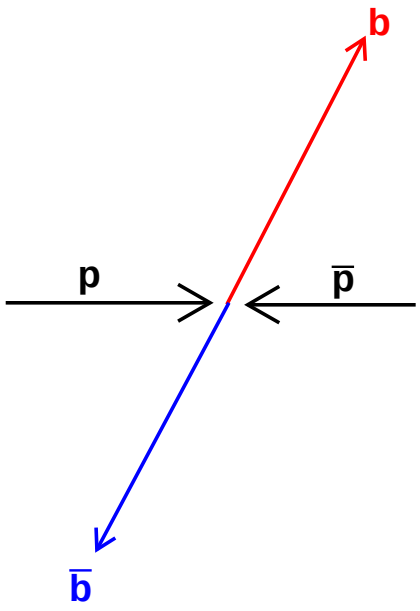

Figure 4.1: Back-to-back $b\bar{b}$ production (`msel`=5).

4.2.2 Detector Simulation

The generator produces four-vectors of final state particles. To correctly model our observation of the data events, these four-vectors are passed through a full simulation of the DØ detector. The simulation consists of two parts: DØGSTAR [37] and DØSIM [38]. DØGSTAR is based on the CERN program GEANT [39] that allows one to describe a detector by building up the geometry from a library of known shapes. DØGSTAR allows one to

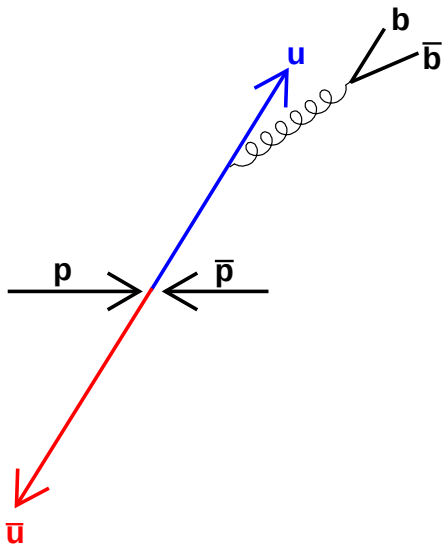

Figure 4.2: Example of production of $b\bar{b}$ pairs through gluon splitting. `msel`=1 production includes both this form of $b\bar{b}$ production, flavor creation, as well as back-to-back production.

trace a particle through the detector and identify where the particle interacts with matter while simulating energy deposits and secondary interactions.

DØSIM take the output from DØGSTAR and modifies it to account for various detector-related effects including analog-to-digital conversion within the detector and then converts the MC to mimic real data takes when it is processed through the DØ electronics. Also included in this simulation are various detector inefficiencies and noise from the detector and its electronics. DØSIM also takes into account 'pile-up', which is the collision of multiple

$p\bar{p}$ pairs within a single bunch crossing. The output of DØSIM is in the same format as that which comes from the detector, which allows it to be processed by DØRECO. DØRECO reconstructs the Monte Carlo events in the same manner as the data events, with the exception that it retains generator level information to allow the correlation of generated events with reconstructed events.

The Monte Carlo programs are often updated to include improvements that aid in the proper simulation of DØ data. The updates are released in versions and the Monte Carlo for this analysis was produced both with version p14.06.01 and p17.09.01. References to p14 and p17 within this thesis refer to those production versions, respectively.

Chapter 5

Data Analysis

5.1 Analysis Overview

This analysis will discuss the measurement of the branching ratio $Br(B_s^0 \rightarrow D_{s1}^-(2536)\mu^+\nu X)$ at the DØ detector. Beginning with the formation of the B_s meson, the decay into a D_s^{**} will be explained, followed by the measurement of the branching ratio. Finally, systematic errors will be assessed and a comparison with theoretical predictions will be made.

5.1.1 Creating a B_s^0

At the Tevatron, protons and anti-protons are collided at a center of mass energy of $\sqrt{s} = 1.96$ TeV. Protons and antiprotons both consist of three constituent 'valence' quarks, virtual gluons, and virtual 'sea' quark-antiquark pairs. The momentum of the protons is distributed between the three components of the hadron according to the parton distribution function.

Typically gluons carry about half of the momentum of a proton [40].

In the leading-order (LO) QCD approximation, heavy quarks are produced via either quark-antiquark annihilation or gluon-gluon fusion. Of particular interest to this thesis is gluon-gluon fusion as shown in Figure 5.1 as this is the dominant source of $b - \bar{b}$ production. Also of interest is the next-to-leading order (NLO) production of $b-\bar{b}$ pairs through gluon splitting and flavor excitation processes as shown in Figure 5.2. The LO and NLO cases are both important cases to consider as they result in very different kinematically-aligned $b-\bar{b}$ pairs. In the LO case, the $b-\bar{b}$ pairs will be back to back with no extra gluons and in the NLO case, the b quark and the $\bar{b}$ will close together and a significant portion of the transverse energy will be taken up by gluons [41].

Once a b quark is produced, the next step is the formation of B hadrons. This process is called hadronization. This process can be thought of as a situation where one has gluons acting as a 'string' between a $b-\bar{b}$ pair. The string is then stretched as the quark-antiquark pair separates, until the potential energy in the gluon string is too great and the string 'breaks', resulting in a new quark-antiquark pair. Two new strings will then form and break and so on until there is no longer sufficient energy to form quark-antiquark pairs. Depending on what the stretching of the $b - \bar{b}$ quark produces, a $u\bar{u}, d\bar{d}$, $s\bar{s}$ or $c\bar{c}$, the b quark will combine to form either a B^+, B^0_d, B^0_s, or B^+_c meson. The lightest mass quarks, u and d, are produced most often and the meson of

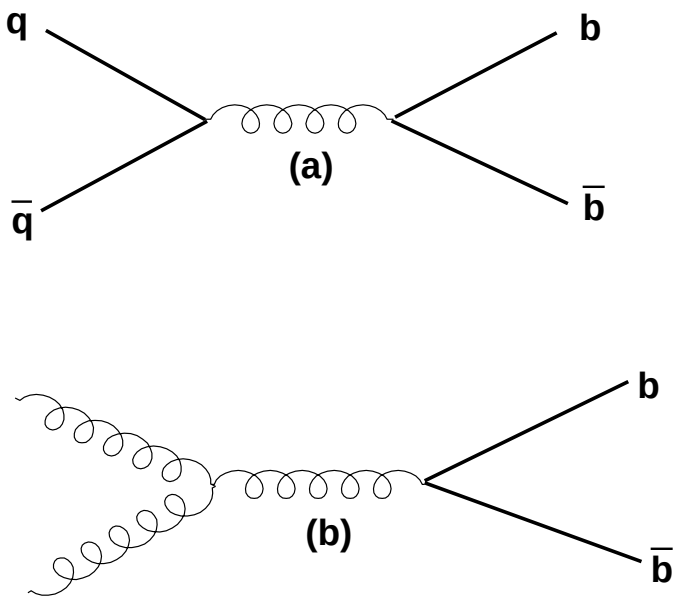

Figure 5.1: $b\bar{b}$ production in the leading-order QCD approximation.

interest in this thesis, B_s^0, is suppressed due to the higher mass of the strange quark. The b quark will hadronize to a B^+ or B_d^0 approximately 40% of the time, B_s^0 approximately 11% of the time and other hadrons, including the λ_B and B_c, the rest of the time.

5.1.2 The Decay $B_s^0 \to D_{s1}^-(2536)\mu^+\nu X$

Once a B_s^0 meson is produced, it can then decay via the electroweak process after traveling a distance on the order of 1 mm, emitting a W^+

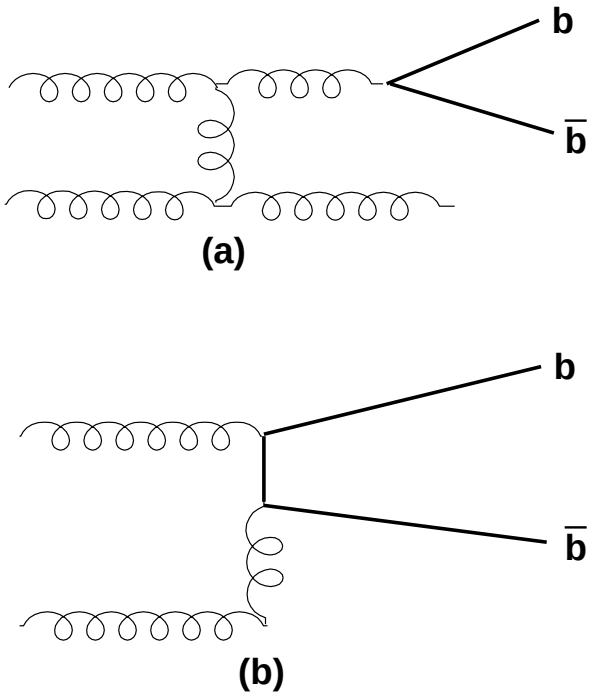

Figure 5.2: $b\bar{b}$ production in the next-to-leading order QCD approximation.

boson with the $\bar{b}$ quark decaying to a $\bar{c}$. The $\bar{c}$ quark and s quark combine to form a D_s while the W^+ can decay into a muon and a muon neutrino. The neutrino escapes the detector undetected and the muon will travel to the muon detectors. As indicated in Section 3.3.5, the DØ detector has excellent muon detection and this is the particle that is triggered on for this analysis. Thus, to take fully advantage of the muon in the final state, the analysis begins with the single muon skim, which will be described in section 5.2.

Should both quarks in the D_s have their spins aligned and also be pro-

duced in an orbitally excited state, this D_s meson is said to be doubly excited and is denoted as D_s^{**}. As it takes more energy to produce a D_s meson in a state that is both spin and orbitally excited, this process is expected to be more rare than just simple semileptonic D_s production. It is the measurement of the frequency in which a B_s^0 will decay to a D_s^{**}, the branching ratio, that we will present in this thesis.

The D_s^{**} will almost immediately decay to a D^{*+} (a spin aligned $\bar{c}u$ state with L=0) and a K_S^0. The D^{*+} will then subsequently decay to a D^0 and a 'slow' pion. The D^{*+} and the D^0 have a mass difference of very little more than the mass of a pion, and thus there is level little additional energy left over to boost the pion. Thus it is referred to as a 'slow' pion and is indicated by the symbol π^*. The K_S^0 travels a distance on the order of several centimeters before decaying into a π^+ and a π^-. The neutral K_S^0 track is not seen in the detector, only the resulting pion tracks from the decay. Finally, the D^0 decays into a $K^-\pi^+$. The final state of a muon, the two pions from the K_S^0 decay, the slow pion, and the K^+, leave a signature in the detector and are the five tracks which need to be reconstructed for this analysis as shown in Figure 5.3.

This state is ideally suited to detection within the DØ detector. As the DØ detector does not have particle identification, it cannot differentiate between different tracks within the detector, e.g. a K and a π are indistinguishable within the detector, it is necessary to take advantage of the

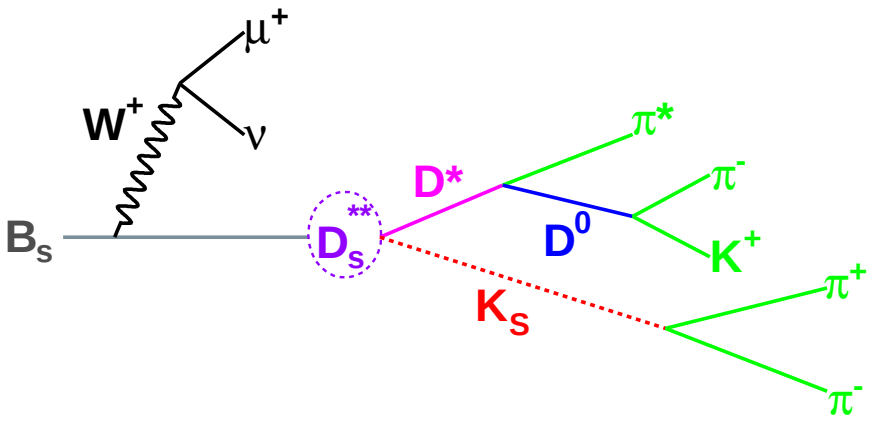

Figure 5.3: A pictorial view of the decay chain $B_s^0 \rightarrow D_{s1}^-(2536)\mu^+\nu X$, resulting in the final state of four pions, a kaon, and a muon.

characteristic signatures of the D^* and K_S^0. The D^* is unique in that, due to the very small mass difference between the D^* and D^0, cuts placed on the mass difference between the D^* and D^0 yield a very pure sample of D^* events with very low background (see Figure 5.5 in section 5.2.5). The K_S^0, on the other hand, is unique in that it travels for a relatively long distance (several centimeters) before decaying, thus removing the soft pion tracks of its decay products away from the primary vertex where the majority of tracks in a $p\bar{p}$ collision are found. This makes the pion tracks less likely to be incorrectly vertexed and reduces the probability of a random π track being assigned to a K_S^0 meson candidate.

5.1.3 Measuring $Br(B_s^0 \to D_{s1}^-(2536)\mu^+\nu X)$

Once the decay $Br(B_s^0 \to D_{s1}^-(2536)\mu^+\nu X)$ is fully reconstructed and a signal sample is selected (the details of which will be discussed in future sections), one can measure the branching ratio.

The branching ratio $Br(B_s^0 \to D_{s1}^-(2536)\mu^+\nu X)$ can be determined by normalizing to the known value of the branching fraction $Br(\bar{b} \to D^{*-}\mu^+\nu X) = (2.75\pm0.19)\%$ [3]. This semileptonic branching ratio includes any decay channel or sequence of channels resulting in a D^* and a lepton (muon in our case), and is over all b hadrons, and therefore includes the relative production of each b hadron species starting from a $\bar{b}$ quark.

Since the final state of interest, $D_{s1}^{\pm}(2536) \to D^{*\pm}K_S^0$, is taking a reconstructed D^* and combining it with a reconstructed K_S^0, the selection is broken up into two sections: one to reconstruct D^* with an associated μ, coming dominantly from B meson decays, and then the addition and vertexing of a K_S^0 with the D^* and muon.

To determine the branching ratio, the following formula is used:

$$\begin{aligned} & f(\bar{b} \to B_s^0) \cdot Br(B_s^0 \to D_s^{**}\mu^+\nu X)\cdot \\ Br(D_s^{**} \to D^{*-}K_S^0) &= Br(\bar{b} \to D^{*-}\mu^+\nu X) \cdot \frac{N_{D_s^{**}}}{N_{D^*\mu}}\cdot \\ & \frac{\epsilon(\bar{b} \to D^*\mu)}{\epsilon(B_s^0 \to D_s^{**}\mu \to D^*\mu)} \cdot \frac{1}{\epsilon_{K_S^0}} \ . \end{aligned} \tag{5.1}$$

The input $f(\bar{b} \to B_s^0) = 0.107 \pm 0.011$ [3] is the fraction of time that a b quark hadronizes to a B_s^0 meson. As mentioned above, the majority of

the time, a $\bar{b}$ quark will combine with an up or down quark to form a B^+ or B_d^0 meson, respectively, but approximately 10.7% of the time the $\bar{b}$ quark forms a B_s^0 by hadronizing with a strange quark. Finally, as described above, $Br(\bar{b} \to D^{*-}\mu^+\nu X) = (2.75 \pm 0.19)\%$ [3] is taken from other measurements.

$\epsilon_{K_S^0}$ is the efficiency in the signal decay channel to additionally reconstruct and vertex a K_S^0 to form a $D_{s1}^{\pm}(2536)$ once a $D^* + \mu$ have already been reconstructed. Finally, we will identify the ratio of efficiencies later as: $R_{D^*}^{\text{gen}} = \epsilon(B_s^0 \to D_{s1}\mu \to D^*\mu)/\epsilon(\bar{b} \to D^*\mu)$, i.e., the numerator is the efficiency in the decay channel for reconstructing a $D^* + \mu$, while the denominator is the efficiency to reconstruct $D^* + \mu$ using identical cuts given that a b quark decays into a channel or sequence of channels ultimately resulting in $D^* + \mu$. Neither of these efficiencies include any K_S^0 selection requirements.

The benefit of a normalization done this way is that the only absolute efficiency needed from Monte Carlo is that of $\epsilon_{K_S^0}$ which covers just a fraction of the total efficiency for this state. Absolute efficiencies for muon identification, D^* reconstruction, triggering to enter the single muon sample, etc., are not needed, and uncertainties in the efficiencies tend to cancel in the ratio.

5.2 Event Sample and Selection

5.2.1 Data Sample

This measurement uses the large preselected single muon data sample corresponding to approximately 1.35 fb^{-1} of integrated luminosity [42] col-

lected by the DØ detector between April 2002 and March 2006 [1]. The single muon data sample is an object skim and is a combination of several other object skims with varying p_T requirements listed below:

- A single, central muon with $p_T > 8$ GeV,
- Two muons, one of which has a p_T of at least 1 GeV in the central region,
- A muon with a $p_T > 5$ GeV, plus two tracks with $p_T > 5$ GeV and $p_T > 8$ GeV, respectively,
- A muon with a $p_T > 10$ GeV in the central region plus two jets, each with $p_T > 8$ GeV,
- A muon plus two jets, each with $p_T > 10$ GeV. The muon is required to have $p_T > 4$ GeV, $nseg > 3$, and be within a jet.

In principle, any trigger could contribute to this sample. Events were reconstructed using the standard DØ software suite [43] after the removal of events that enter the sample only via impact parameter biasing triggers. Information only from the muon and tracking systems was used in this analysis.

Evidence of $D_{s1}^{\pm}(2536)$ mesons was found in decays of $B \to \mu\nu D_s^{**}X$ as resonances in the $D^{*+}K_S^0$ invariant mass spectrum. D mesons were required

[1] A precise measurement of the integrated luminosity is not needed for this analysis since we normalize our channel of interest to $\bar{b} \to D^*\mu\nu X$.

to decay subsequently to $D^{*+} \rightarrow D^0\pi^+$, $D^0 \rightarrow K^-\pi^+$. The K^0_S meson was reconstructed using $K^0_S \rightarrow \pi^+\pi^-$.

The event selections are described below. B mesons are first selected using their semileptonic decays, $B \rightarrow \bar{D}^0\mu^+X$, followed by finding D^* mesons in $B \rightarrow D^{*-}\mu^+X$. This selection is a mostly a standard one, used by the DØ analysis measuring the B^+/B^0_d lifetime ratio [54] and B^0_d oscillations [51]. At this point, the $D^* + \mu$ sample is dominated by $B^0_d \rightarrow D^{*-}\mu^+\nu X$ decays before a $D^{\pm}_{s1}(2536)$ selection is made.

5.2.2 Removing Trigger Bias

While the majority of events selected in the inclusive muon sample satisfy single muon trigger requirements, it is possible to have events trigger only on lifetime-biasing triggers. To avoid this, events that triggered exclusively on impact parameter biasing triggers were removed from the event selection. These triggers are removed to eliminate the need to determine their trigger efficiencies and their subsequent impact on lifetime-biased selection criteria in the analysis.

- Impact-parameter biasing triggers removed from sample are
  - ML1_TMM_IPPHI
  - MM1_TMM_IPPHI
  - ML2_MM_IPPHI

- MM1_HI_TMM_IPPHI
- MEB1_MM_IPPHI
- ML1_IPTMM_IMP_V
- MM1_IPTMM5_IMPV
- MM1_HI_IPTMM
- ML1_TMM_2IP_IMPV
- ML1_TMM_3IP_IMPV
- ML1_TMM_4IP_IMPV
- MM1_TMM_IMP_2IPV
- MM1_TMM_IMP_3IPV
- MM1_TMM_IMP_4IPV
- ML2_2IPMM_IMP_V
- ML2_3IPMM_IMP_V
- ML2_4IPMM_IMP_V
- ML3_2IPMM_IMP_V
- MM1_HI_TMM_2IPV
- MM1_HI_TMM_3IPV
- MEB1_2IPMM_IMP_V
- MEB1_3IPMM_IMP_V

- MEB1_4IPMM_IMP_V
- MUJB_MM0_BID
- JT1_ACO_MHT_BDV
- JT2_3JT15L_IP_VX
- JT3_3JT10L_LM3_V
- JT7_3JT15L_IP_VX
- MUJ1_2JT12_LMB_V
- MUJ1_JTHATK_LMVB
- MUJ2_2JT12_LMB_V
- MUJ2_JTHATK_LMVB
- ZBB_TLM3_2JBID_V
- ZBB_JT_HATKTLMV
- EZBB_SHT122J12VB
- MT3_L2M0_MM3_IP
- ZB1_TLM3_2JBID_V
- ZB1_JT15HA_TLM8V
- E3_SHT122J12VB

5.2.3 Muon Selection

As indicated above, the analysis begins with the selection of a muon. This is a key element to the analysis as it takes advantage of the excellent DØ muon detection system. With excellent η coverage, one can expect a large muon yield.

Muons were identified using standard DØ criteria [44]. For this analysis, muons were required to have hits in more than one muon chamber ($nseg > 1$), to have an associated track in the central tracking system with at least one hit in both SMT and CFT present, and to have transverse momentum $p_T^\mu > 2$ GeV/c, pseudorapidity $|\eta^\mu| < 2$, and total momentum $p^\mu > 3$ GeV/c.

All charged particles in the event were clustered into jets using the DURHAM clustering algorithm [45]. Events with more than one identified muon in the same jet were rejected, as well as the events with an identified $J/\psi \to \mu^+\mu^-$ decay.

5.2.4 D^0 Selection

Once a muon is selected, the next step in the selection is the vertexing of a $\bar{D}^0$ candidate with the muon.

The $\bar{D}^0$ candidate was constructed from two particles of opposite charge included in the same jet as the reconstructed muon. Both particles should have hits in SMT and CFT, transverse momentum $p_T > 0.7$ GeV/c, and pseudo-rapidity $|\eta| < 2$. They were required to form a common D-vertex

with fit $\chi^2_D < 9$. For each particle, the axial[2] ϵ_T and stereo[3] ϵ_L projections of track impact parameter with respect to the primary vertex together with the corresponding errors ($\sigma(\epsilon_T)$, $\sigma(\epsilon_L)$) were computed. The combined significance $\sqrt{(\epsilon_T/\sigma(\epsilon_T))^2 + (\epsilon_L/\sigma(\epsilon_L))^2}$ was required to be greater than 2. The distance d_T^D between the primary and D vertex in the axial plane was required to exceed 4 standard deviations: $d_T^D/\sigma(d_T^D) > 4$. The angle α_T^D between the $\bar{D}^0$ momentum and the direction from the primary to the $\bar{D}^0$ vertex in the axial plane was required to satisfy the condition: $\cos(\alpha_T^D) > 0.9$.

The tracks of muon and $\bar{D}^0$ candidate were required to form a common B-vertex with fit $\chi^2_B < 9$. The momentum of the B candidate was computed as the sum of momenta of the μ and $\bar{D}^0$. The mass of the (μ^+ $\bar{D}^0$) system was required to fall within $2.3 < M(\mu^+ \bar{D}^0) < 5.2$ GeV/c^2. If the distance d_T^B between the primary and B vertices in the axial plane exceeded $4 \cdot \sigma(d_T^B)$, the angle α_T^B between the B momentum and the direction from primary to B vertex in the axial plane was demanded to satisfy the condition $\cos(\alpha_T^B) > 0.95$. The distance d_T^B was allowed to be greater than d_T^D, provided that the distance between B and D vertices d_T^{BD} was less than $3 \cdot \sigma(d_T^{BD})$.

The masses of the kaon and pion were assigned to particles according to the charge of the muon, requiring a $\mu^+K^+\pi^-$ final system. In the following, events falling into the $K\pi$ invariant mass window between 1.75 and 1.95 GeV/c^2 will be referred to as $\mu^+\bar{D}^0$ candidates.

[2]In the plane perpendicular to the beam direction.

[3]In the plane parallel to the beam direction.

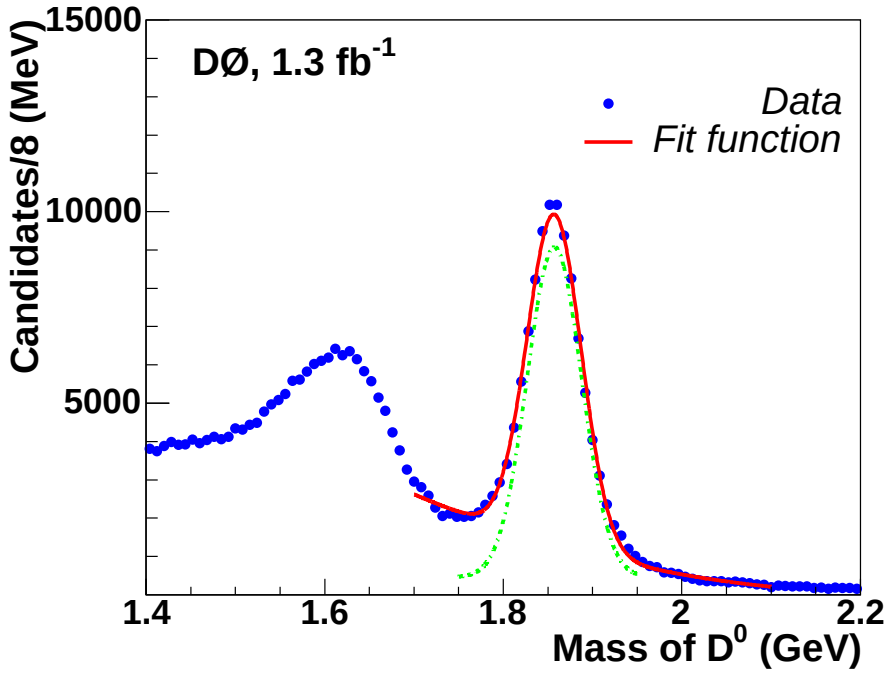

Figure 5.4: The invariant mass of $K\pi$ system for $\mu^+K^+\pi^-$ combinations within D^* mass difference window (see subsection 5.2.5). The curve shows the result of the fit of the $K^+\pi^-$ mass distribution with the signal modeled with a double Gaussian function with the means fixed and a polynomial function for the background. The total number of D^0 candidates in the peak is determined to be 104970 ± 3922 (stat.).

5.2.5 D^* Selection

With a μD^0 vertex selected and determined to be from a B, it is next necessary to vertex a 'slow' pion with the $\bar{D}^0$. As discussed above, a very clear peak is expected due to the small (~ 0.14 GeV) mass difference between the $\bar{D}^0$ and the D^*. In taking the mass difference rather than simply the D^*

mass, resolution effects also cancel to first order and the observed peak is very narrow.

For each $\mu^+\bar{D}^0$ candidate, we search for an additional slow pion (π^*) with charge opposite to the charge of muon and with $p_T > 0.18$ GeV/c. The mass difference $\Delta M = M(\bar{D}^0\pi) - M(\bar{D}^0)$ for all such pions when $1.8 < M(\bar{D}^0) < 1.95$ GeV/c^2 is shown in Fig. 5.5.

At this point it is necessary to make sure that the μD^* candidate comes from a B meson and so, to reduce the contribution from $c\bar{c}$, particularly from gluon splitting, where one charm quark fragments to D^* and the other to a charm hadron that subsequently decays to a muon, a requirement was placed on the decay length significance of the μD^* vertex of $L/\sigma(L) > 1$, i.e., a requirement that the μD^* vertex is displaced from the primary vertex by more than the error on the measured decay length. This helps to ensure that the decay products come from a B meson since B mesons will travel a detectable distance before decaying. The effect of the $c\bar{c}$ contribution is discussed in detail later in section 5.4.7. The peak corresponding to the production of $D^*\mu$ is clearly seen (Fig 5.5) and later fit in Section 5.4 to obtain a D^* yield.

5.2.6 K^0_S Selection

To select a K^0_S once a D^* was already vertexed with a muon, all tracks were considered that shared a primary vertex with the μD^* vertex. It was

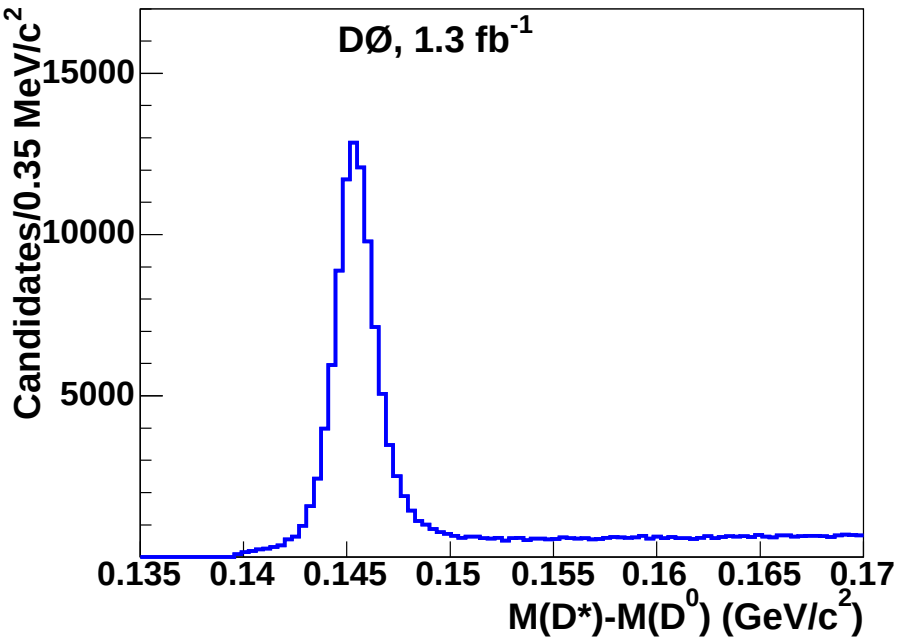

Figure 5.5: The mass difference $M(D^0\pi) - M(D^0)$ for events with $1.8 < M(D^0) < 1.95$ GeV/c^2.

required that each track have at least four two-dimensional hits, at least two of which were CFT hits. Both tracks were required to have opposite charge and, for the two pion hypothesis, the invariant mass was required to be in the mass range $0.43 < M(\pi_1, \pi_2) < 0.56$ GeV. To reduce contributions from photon conversions, the mass was required to be $M(\gamma_1\gamma_2) > 0.25$ GeV. The combined significance $\sqrt{(\epsilon_T/\sigma(\epsilon_T))^2 + (\epsilon_L/\sigma(\epsilon_L))^2}$ was required to be greater than 3 and the distance $d_T^{K_S^0}$ between the primary and both tracks in the axial plane was required to exceed 2 standard deviations: $d_T^{K_S^0}/\sigma(d_T^{K_S^0}) > 2$. The angle $\alpha_T^{K_S^0}$ between the K_S^0 momentum and the direction from the primary

to the K_S^0 vertex in the axial plane was required to satisfy the condition: $\cos(\alpha_T^{K_S^0}) > 0.8$.

5.2.7 $D_{s1}^{\pm}(2536)$ Selection

As mentioned in section 5.1.2, the $D_{s1}^{\pm}(2536)$ was reconstructed through the decay channel $D_{s1}^{\pm}(2536) \rightarrow D^{*\pm}K_S^0$. $D_{s1}^{\pm}(2536)$ candidates were formed by combining a D^* candidate with a K_S^0. D^* candidates were first selected from a mass difference window of $0.142 < (M(D^*) - M(D^0)) < 0.149$ GeV/c^2. This is where the small mass difference between the D^* and the D^0 comes into play as we can select a very pure sample of D^* candidates by cutting on such a narrow mass window.

In addition to the cuts described in selecting an initial K_S^0 candidate, cuts were also applied to the K_S^0 when combining it with the D^* to form the $D_{s1}^{\pm}(2536)$ candidate. The two tracks from the decay of the K_S^0 were required to have opposite charge and to have more than 5 hits in the CFT detector. The p_T of the K_S^0 was required to be greater than 1 GeV/c to reduce the contribution of background fragmentation K_S^0 mesons. A vertex was then formed between the reconstructed K_S^0 and the D^* candidate of the event with a loose requirement of $\chi^2 < 100$ on the vertex.

The decay length of the K_S^0 was required to be greater than 0.5 cm. The reason for this cut is that, as mentioned earlier, in a $p\bar{p}$ collision, the majority of event tracks are located very near to the primary vertex. Since

the majority of K^0_S candidates will decay away from the primary vertex, we can require that the decay length be longer than 0.5 cm and avoid confusion between the low-p_T pion tracks from the K^0_S decay vertex and other random tracks while still losing few K^0_S candidates. It is then expected that there would be a much greater loss of combinatoric background than signal with this cut. This turns out to be correct as this cut results in a loss of 19% of the K^0_S signal, but 52% of the background is also eliminated. One can see from Figure 5.6, a plot of the K^0_S mass versus decay length, that events with a decay length of less than 0.5 cm mostly fall within a flat combinatorial background.

While the initial cuts on the K^+ and π from the decay of the D^0 required a single hit in the CFT, this cut is tightened up in the final selection and the K^+ and π from the decay of the D^0 were both required to have more than 5 CFT hits.

Finally, it was required that the invariant mass of the reconstructed $D^{\pm}_{s1}(2536)$ and muon be less than the mass of the B^0_s meson [3] (since the ν escapes detection, this should always be true for the signal). For combinatoric background, background from $c\bar{c}$, and fragmentation sources, K^0_S mesons will often be at large angles with respect to the muon, pushing this invariant mass above $M(B^0_s)$. The invariant mass of $K^0_S \to \pi^+\pi^-$ candidates in events with reconstructed $D^*\mu$ candidates and passing the cuts above is shown in Fig. 5.7, with a fitted yield of 2815 ± 121 (stat) K^0_S candi-

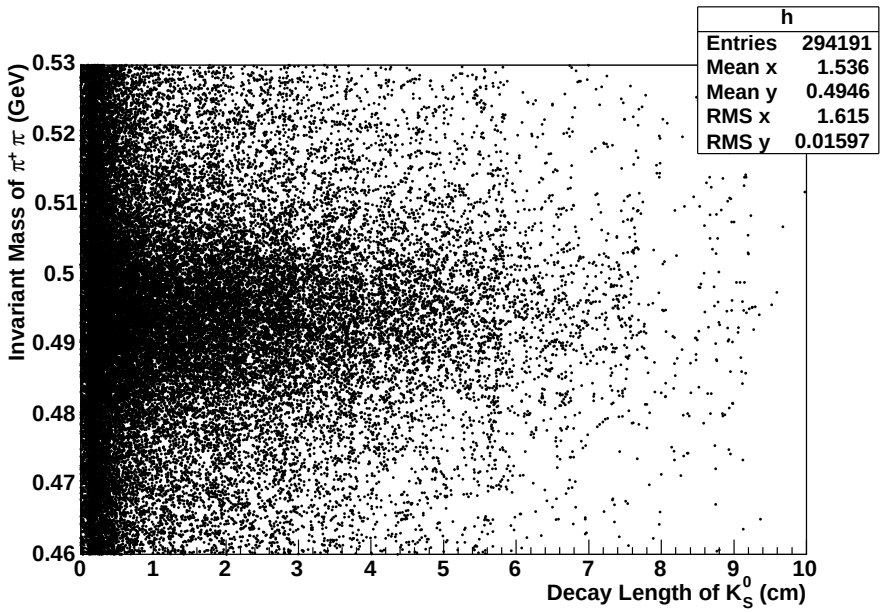

Figure 5.6: A 2-dimensional scatter plot of the K^0_S mass versus decay length.

dates where K^0_S candidates are defined as falling inside a mass window of $0.47 < M(K^0_S) < 0.52$ GeV/c^2, a symmetric window about the PDG value for the K^0_S mass, $M(K^0_S) = 0.497$ GeV.

To compute the $D^{\pm}_{s1}(2536)$ invariant mass, a mass constraint was applied using the PDG value [3] of $M(D^*) = 2010.0$ MeV for the D^* mass instead of the invariant mass of the $K\pi\pi$ system. It is a known effect described above that invariant masses reconstructed within the DØ detector have masses shifted lower than the mass values cited in the PDG. This effect is due to an incorrect modeling of the material within the detector (hence an incorrect determination of energy loss due to ionization) and the magnetic field within

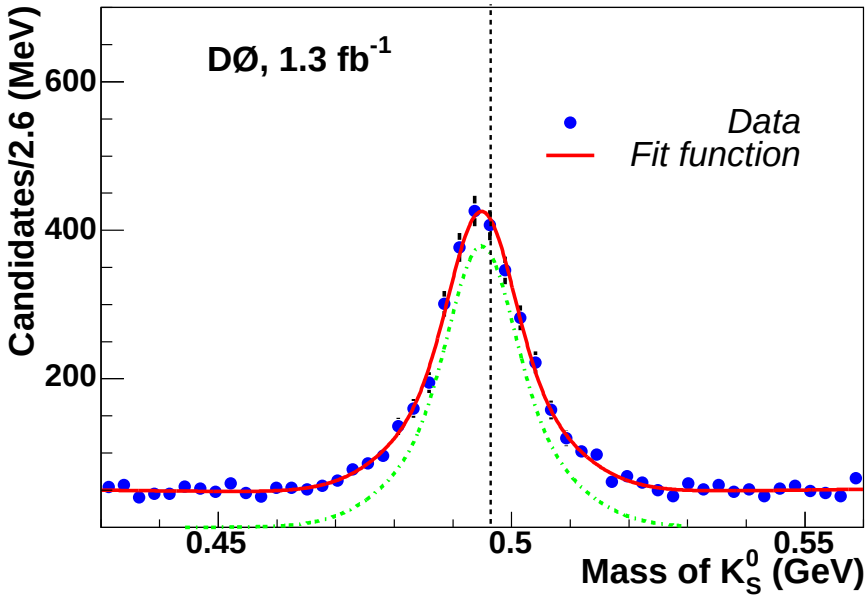

Figure 5.7: Mass of $\pi^+\pi^-$ for events after passing D^* and D^0 cuts. The mass plot was fitted with a double Gaussian function with the same mean for both Gaussian functions modeling the signal and a second-order polynomial function for the background. The dashed line represents the PDG value for the K^0_S mass (see text for explanation of shift).

the detector (resulting in incorrect momentum measurement). By correcting the four-vector momentum of the D^* decay products forcing the mass at the decay vertex to that of the D^* mass cited in the PDG, this mass discrepancy is accounted for. A mass constraint of $M(D^0) = 1.8645$ GeV [3] was also placed on the D^0. The resulting $D_{s1}(2536)$ mass peak is shown in Figure 5.8 and a fit to this peak is shown later in Section 5.4.

A likelihood ratio method [47] was also attempted to increase the signal-

to-noise ratio, but no significant improvement was found.

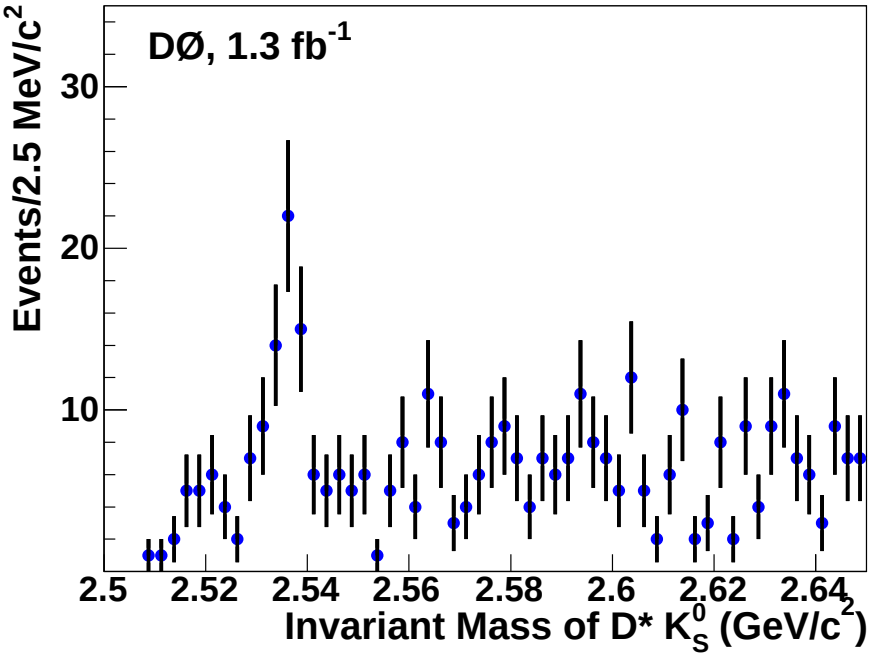

Figure 5.8: Invariant mass of $D^* K_S^0$ after all selection criteria.

5.2.8 List of selections

We list all selections used for the $\mu^\mp\ D_{s1}^\pm(2536)$ candidates below for reference.

- Muon
  - certified muon with nseg > 1
  - $p_T > 2$ GeV/c

  - $p_{tot} > 3$ GeV/c
  - $|\eta^{\mu}| < 2$
  - χ^2 of local fit of muon > 0
  - N(SMT) hits > 1
  - N(CFT) hits > 1

- D^0
  - 2 tracks of opposite charge with $p_T > 0.7$ GeV/c, $|\eta| < 2$ and in the same jet as the above muon
  - N(SMT) > 1 for each track
  - N(CFT) > 1 for each track
  - K has the same charge as muon
  - $1.4 < M(K\pi) < 2.2$ GeV/c^2
  - 3D IP significance > 2 for each track
  - χ^2 of $(K\pi)$ vertex < 9
  - D decay distance/error in axial plane > 4
  - cosine of angle between direction from primary to D vertex and momentum of $D^0 > 0.9$
  - B candidate composed of D^0 and μ

  - if B decay distance/error in axial plane > 4 then cosine of angle between direction from primary to B vertex and momentum of B > 0.95
  - $2.3 < M(\mu D^0) < 5.2$ GeV/c^2
  - χ^2 of (μD^0) vertex < 9
  - if B-vertex is at a radius greater than the D-vertex, distance/error between B and $D < 3$

- D^*
  - $D^* \rightarrow D^0 \pi^*$
  - 1.8 GeV/$c^2 < M(K\pi) <$ 1.95 GeV/c^2
  - π^* : track of opposite charge to muon
  - π^* : $N(\mathrm{SMT}) > 1$
  - π^* : $N(\mathrm{CFT}) > 1$
  - $\frac{dL(\mu D^*)}{\sigma(dL(\mu D^*))} > 1$

- K_S^0
  - It was required that each track have at least four two-dimensional hits, at least two of which had to be CFT hits.
  - Both tracks were required to have opposite charge
  - The invariant mass was required to be in the mass range $0.43 < M(\pi_1, \pi_2) < 0.56$ GeV

  - $M(\gamma_1\gamma_2) > 0.25$ GeV
  - $\sqrt{(\epsilon_T/\sigma(\epsilon_T))^2 + (\epsilon_L/\sigma(\epsilon_L))^2} > 3$
  - $d_T^{K_S^0}/\sigma(d_T^{K_S^0}) > 2$
  - $\cos(\alpha_T^{K_S^0}) > 0.8$

- $D_{s1}^{\pm}(2536)$
  - $D_{s1}(2536) \rightarrow D^* K_S^0$
  - 0.142 GeV/c^2 < [$M(K\pi\pi) - M(K\pi)$] < 0.149 GeV/c^2
  - N(CFT)> 5 for products of D^0 decay and π from D^*decay
  - N(CFT)> 5 for decay products of K_S^0
  - $p_T(K_S^0) > 1$ GeV/c
  - decay length of $K_S^0 > 0.5$ cm
  - invariant mass of μ $D_s^{**} < 5.3696$ GeV

5.3 Monte Carlo Studies

With the signal events reconstructed in data, the next step is to fit the signal and determine the number of D_s^{**} candidates observed. However, before this can be done, it is necessary to model the signal to determine the expected shape and invariant mass of the D_s^{**}. To do this, Monte Carlo samples were generated to model the expected signal. In addition, Monte Carlo

samples were needed for calculating efficiencies and resolutions of selected variables.

For all of the Monte Carlo sample, the standard DØ simulation chain was used that included the PYTHIA generator [35] interfaced with the EVTGEN decay package [36] followed by full GEANT [39] modeling of the detector response and event reconstruction as described in Chapter 4. The full EVTGEN and D0_MESS decay chain with cuts are shown in Appendix 7.

The full decay path of the signal was generated using the default decays of the EVTGEN package, in this case, the ISGW2 semileptonic decay model [19] for the $B_s^0 \to D_{s1}(2536)\mu\nu$ decay, and the model VVS_PWAVE [36] for the decay $D_{s1}(2536) \to D^* K_S^0$. Applying the same analysis cuts to the signal MC sample, the mass peaks of the intermediate (Fig. 5.9) and final candidates (Fig. 5.10) are shown in Fig. 5.9 and Fig. 5.10. A fit is made to the $D_{s1}(2536)$ mass peak with a Relativistic Breit-Wigner function to describe the signal convolved with a Gaussian to account for detector resolution. A Relativistic Breit-Wigner function:

$$\frac{1}{(E^2 - M^2)^2 + M^2\Gamma^2} \tag{5.2}$$

is commonly used to describe resonances in particle physics. In this case, E is the particle energy, M is the particle's mass, and Γ is the width. The detector is also not perfect and has finite resolution. To account for this, the Relativistic Breit-Wigner is convolved with a Gaussian function to take into

account the detector resolution.

The resonance width was fixed to the value of 1.03 ± 0.05 (stat.) ± 0.12 (syst.) MeV/c^2 as measured by BaBar [46] (the PDG upper limit of 2.3 MeV/c^2 was later used to assess the systematic uncertainty due to using this value). This measurement was chosen as the central value as it is the first measurement of the D_{s1} decay width rather than an upper bound as quoted in the PDG. Fitting the signal Monte Carlo with this fixed width, the detector resolution is determined to be 2.8 ± 0.1 MeV/c^2 (stat.). This detector resolution is significantly more narrow than that seen in previous analyses of the wider orbitally excited D-states at DØ, but this difference in resolution is due to the proximity of the D_s^{**} to the lower kinematic threshold. An analogous case is the relatively small detector resolution in the measurement of the Λ baryon mass, another state in which the peak is bounded by a threshold cutoff.

Two background MC samples were generated. An inclusive sample consisting of b quarks hadronizing to all B meson species, forcing semileptonic decays to a muon and then retaining all events with decay paths of the B hadron containing a D^* meson was used to determine the initial selection variables and cuts. A QCD inclusive Monte Carlo sample, including gluon splitting to $c\bar{c}$ and $b\bar{b}$ (i.e., `MSEL`=1) was also generated to estimate the contribution of $c\bar{c}$ events. All events containing both a D^* and a μ were retained.

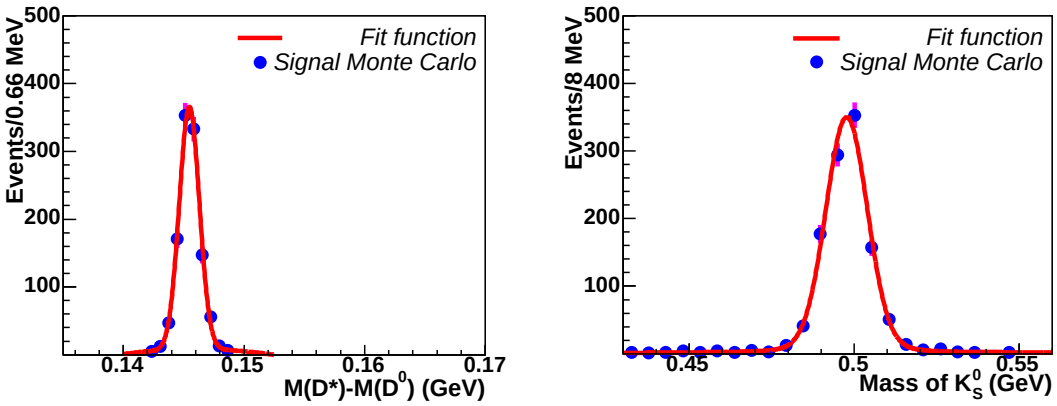

Figure 5.9: Mass peaks as reconstructed in the $B_s^0 \to D_{s1}(2536)\mu\nu$ signal MC sample showing (a) the D^* and (b) the K_S^0 mass peaks following analysis cuts.

5.4 Results

5.4.1 Fitting Methods

To determine the number of signal candidates for both the D^* sample and the D_s^{**} sample, two separate fit methods are used: a binned χ^2 fit and an unbinned extended maximum likelihood fit [48].

Binned χ^2 fit method

A binned fit can be made by minimizing the χ^2 between a fit hypothesis function and a histogram. The χ^2 is given by the expression

$$\chi^2 = \sum_{i=1}^{N} \frac{(n_i - \nu_i)^2}{\nu_i}, \tag{5.3}$$

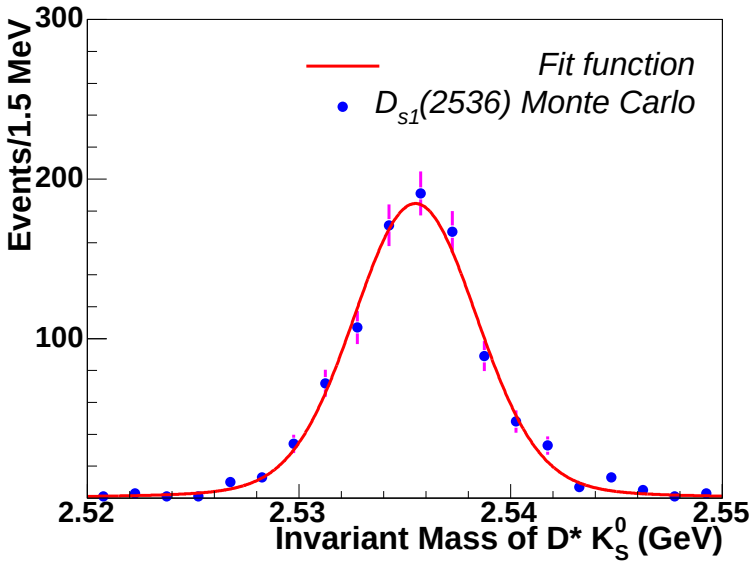

Figure 5.10: $D_{s1}(2536)$ mass peak as reconstructed in the $B_s^0 \to D_{s1}(2536)\mu\nu$ signal MC. The mass peak is fit with a relativistic Breit-Wigner convolved with a Gaussian with the Breit-Wigner width set to the $D_{s1}(2536)$ width as measured by the BaBar collaboration [46].

where ν_i is the hypothesis value for each bin and n_i is the number of entries in a given bin. The smaller the difference between the hypothesis and the bin content for each bin, the smaller (and better) the χ^2. In determining if a χ^2 fit is sufficiently good, one can determine the χ^2/dof where 'dof' is the number of degrees of freedom for the fit which is equal to the number of bins, N, minus the number of free parameters in the fit. A $\chi^2/d.o.f = 1$ is considered a good fit.

The unbinned extended maximum likelihood fit

A maximum likelihood fit starts from a set of N independently measured quantities x_i from a Probability Distribution Function (p.d.f.) $f(x;\theta)$, where $\theta = (\theta_1, ...\theta_n)$ is a set of n unknown parameters. Given a p.d.f., a likelihood function can be constructed

$$L(\theta) = \prod_{i=1}^{N} f(x_i;\theta). \tag{5.4}$$

It is typically easier to work with the $\ln L$ instead, since both are maximized for the same parameter values of θ, and so the maximum likelihood is found by minimizing the equation:

$$\frac{\partial \ln L}{\partial \theta_i} = 0, \tag{5.5}$$

where $i = 1, ..., n$. In practice, one generally minimized the quantity $-2\ln L(\theta)$. For the extended maximum likelihood fit, one can treat the number of n as a Poisson distribution. If we normalize out p.d.f. $f(x_i, \theta)$ such that

$$\int_{x_i}^{x_f} f(x_i, \theta) = A(\theta), \tag{5.6}$$

then the likelihood to be maximized becomes

$$L(\theta) = \frac{A(\theta)^N e^{-A(\theta)}}{N!} \prod_{i=1}^{N} \frac{f(x_i, \theta)}{A(\theta)}, \tag{5.7}$$

and so, for the negative log, we get

$$-\ln L(\theta) = -\sum_{i=1}^{N} \ln(\frac{f(x_i,\theta)}{A(\theta)}) - N\ln(A(\theta) + \ln(N!). \tag{5.8}$$

Dropping the constant term and canceling the $NlnA(\theta)$, we arrive at an expression for the extended log likelihood,

$$-\sum_{i=1}^{N} \ln f(x_i,\theta) + A(\theta). \tag{5.9}$$

As $n \to \infty$, we arrive at the unbinned extended maximum likelihood function used to fit the $D^*K^0_S$ invariant mass spectrum in this analysis.

5.4.2 Number of $D^* + \mu$ Candidates

To fit the $D^* - D^0$ mass difference peak, a binned χ^2 fit was made to the mass difference spectrum. A double Gaussian function was used to model the peak and an exponential function plus a polynomial was used to model the background. The total number of data D^* candidates in the peak of Fig. 5.11 is determined to be equal to $N_{D^*\mu} = 87506 \pm 496$ (stat.), and was defined as the number of signal events fit in the [0.142–0.149] GeV mass difference window.

5.4.3 Number of $D^{\pm}_{s1}(2536)$ Candidates

With the detector resolution effects understood and the signal shape determined, it is now possible to fit the invariant mass spectrum of the $D^*K^0_S$

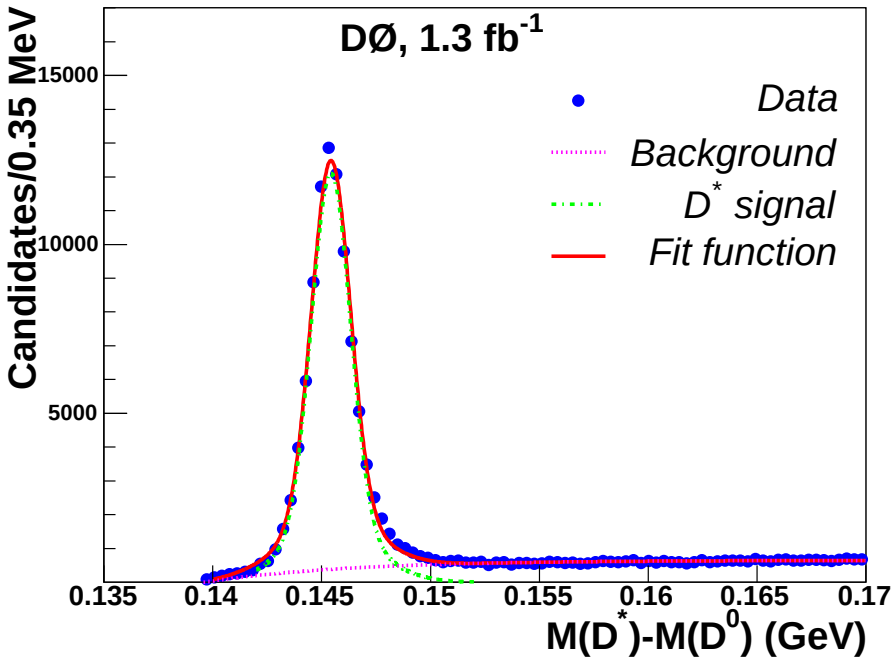

Figure 5.11: The mass difference $M(D^*) - M(D^0)$ for events with $1.8 < M(D^0) < 1.95$ GeV/c^2. The total number of D^* candidates and an associated muon is equal to 87506 ± 496 (stat) and was defined as the number of signal events in the [0.142–0.149 GeV/c^2] mass difference window. In the fit function, the signal and the background have been approximated by the sum of two Gaussian functions and by the sum of an exponential and first-order polynomial function, respectively.

data candidates. The signal model employed for the fit to the $D^* K^0_S$ invariant mass spectrum was a Relativistic Breit-Wigner function convolved with a Gaussian with the resonance width fixed to the value measured by BaBar and the width of the Gaussian determined from the MC studies of the previous section. However, mass resolutions predicted by the MC compared to

the data are typically underestimated by 10–20% for other B hadron mass peaks, and in this case, the MC width value of 2.8 MeV/c^2 was scaled up by a factor of 1.10 ± 0.10 (with the effect of the variation taken later as a systematic uncertainty). The unbinned maximum likelihood fit used an exponential function plus a first-order polynomial to model the background, and a common threshold cutoff of $M(D^*) + M(K^0_S)$ shown in Equation 5.10 was applied,

$$p_1 \cdot [1 - \exp^{(x-p_2)\cdot p_3} + p_4 \cdot (x - p_2)], \tag{5.10}$$

where p_2 represents the threshold cutoff.

The fit, as shown in Fig. 5.12, gives a central mass value for the Gaussian of 2535.7$\pm$0.6 (stat.) MeV/c^2, a yield of $N_{D_{s1}(2536)} = 45.9 \pm 9.1$ (stat.) events, and a calculated significance of 5.1σ for the observed signal to fluctuate down to background and a significance of 6.1σ for the background to fluctuate up to or more than the observed number of signal events. The error is statistical only.

5.4.4 Reweighting of Monte Carlo

It is a known effect that the PYTHIA MC generation of b production does not model the true $p_T(b)$ distribution well when compared to data. In addition, the MC sample has not been passed through a trigger simulation (which has its own deficiencies), that will affect the shape of the p_T distribu-

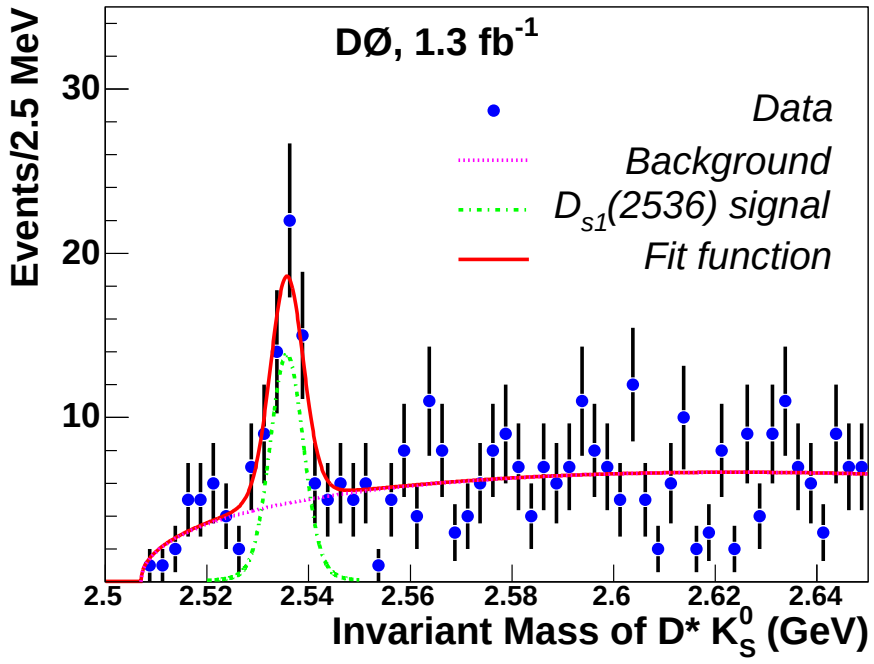

Figure 5.12: Invariant mass of $D^*K^0_S$ with an associated muon. Shown is the result of the fit of the $D^*K^0_S$ mass with a relativistic Breit-Wigner convolved with a Gaussian to model the signal and an exponential plus polynomial function with a threshold cutoff at $M(D^*)+M(K^0_S)$ to model the background. The total number of $D_{s1}(2536)$ candidates in the peak is estimated to be $45.9 \pm 9.1\,(\text{stat})$.

tion. Thus, to more accurately model the data with Monte Carlo simulated events, an iterative reweighting process is employed.

The first step in the reweighting process is to apply a weighting function to improve the kinematic agreement between the Monte Carlo and data. To do this, first it is necessary to generate a weighting function. This is

accomplished by plotting both the p_T distribution of the B meson in Monte Carlo and in data, and then dividing the data distribution by the Monte Carlo distribution, resulting in a ratio that can be fit to a functional form. In other words, if one has two histogram of the B meson p_T, then one can divide each histogram and each bin will then hold the value

$$\frac{p_T \text{ of } B \text{ meson(data)}}{p_T \text{ of } B \text{ meson(MonteCarlo)}} \tag{5.11}$$

and the new histogram holding that fraction will be fit to a functional form. To determine this weighting function, it is necessary to first obtain a p_T distribution from data with minimal trigger effect[4]. In this case, the p_T spectrum of B mesons that were recorded on a dimuon trigger was used [49]. Events with two muons are rarer than events with a single muon and the thresholds on the dimuon trigger can thus be set at a lower muon p_T. This allows the reweighting function to extend into the softer kinematic regions. This p_T spectrum is then compared with the B meson p_T spectrum in Monte Carlo at the generator level (to exclude detector effects) and a reweighting function is generated.

Depending on the production version of the Monte Carlo generated, one of the following functions was used for reweighting: for p14 the $p_T(B)$ dependent reweighting function took on the form $0.314 + 0.051 \cdot p_T(B)$ and for p17, the

[4]it is unrealistic to expect a p_T distribution that is completely free of trigger effects, but some triggers are less restrictive than others

reweighting has the functional form

$$1.32 \cdot \exp[0.018 \cdot (p_T(B) - 12.32)^2)] \tag{5.12}$$

as shown in Figure 5.13 if $p_T(B) \leq 14.0$ GeV and

$$1.39 \cdot \exp[-0.603 \cdot (p_T(B) - 0.012)] \tag{5.13}$$

for all other B meson p_T.

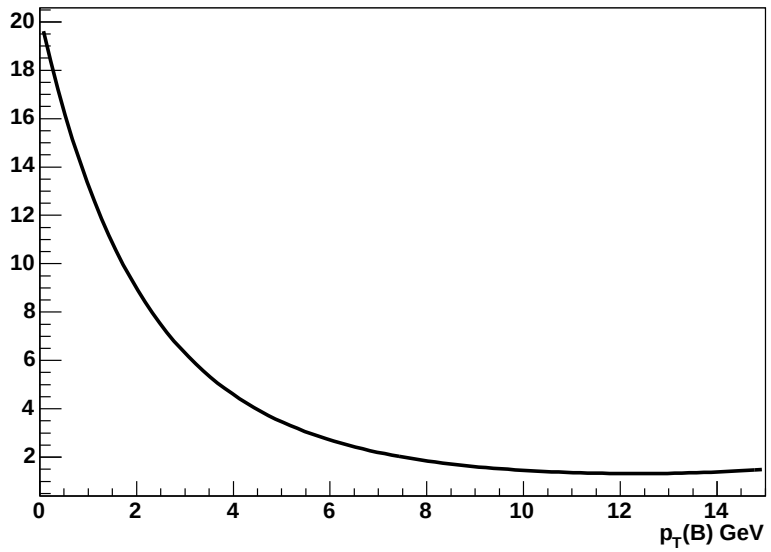

Figure 5.13: Plot of functional form used to reweight p17 Monte Carlo for $p_T(B) \leq 14.0$ GeV.

For the second step in the reweighting, data used in this measurement, in this case, the $D^*\mu$ sample, was used as a basis for further reweighting the

MC sample to provide a better description of the data, including single-muon trigger effects. This is referred to as a 'trigger turn-on' curve.

Figure 5.14(a) shows the data reconstruction of $p_T(\mu)$ compared with the MC weighted as described previously. The data and Monte Carlo are normalized to agree at high p_T where there is assumed to be no trigger effects. The disagreement at lower values of p_T is due to the unsimulated trigger. By dividing the two distributions of Fig. 5.14(a) and fitting to a sigmoid function, the trigger efficiency turn-on curve of Fig. 5.14(b) is obtained. This functional form is then used as a second weighting and is used to account for trigger effects. Weighted MC events, including this trigger efficiency extracted from the data, are included in the determination of efficiencies that follow.

5.4.5 Ratio of $D^* + \mu$ Efficiencies, $R^{\rm gen}_{D^*}$

In the determination of $Br(B^0_s \rightarrow D^-_{s1}(2536)\mu^+\nu X)$, we are normalizing to the known decay channel $\bar{b} \rightarrow D^*\mu\nu$. However, in order to do this, it is necessary to account for possible differences in efficiencies for reconstructing a D^* from the inclusive $\bar{b} \rightarrow D^*\mu\nu$ sample and a D^* from $B^0_s \rightarrow D^-_{s1}(2536)\mu^+\nu X$, $D^{**}_s \rightarrow D^*$. For example, it is expected that a D^* from $B^0_s \rightarrow D^-_{s1}(2536)\mu^+\nu X$, $D^{**}_s \rightarrow D^*$ will have a softer p_T than that from $B^0_d \rightarrow D^*\mu\nu$ and thus will have a lower reconstruction efficiency. To account for this, a ratio is taken of the efficiency to reconstruct a D^* in the inclusive semileptonic $b \rightarrow D^*\mu\nu$ sample to that of the $D^{\pm}_{s1}(2536) \rightarrow D^{*\pm}K^0_S$ sample,

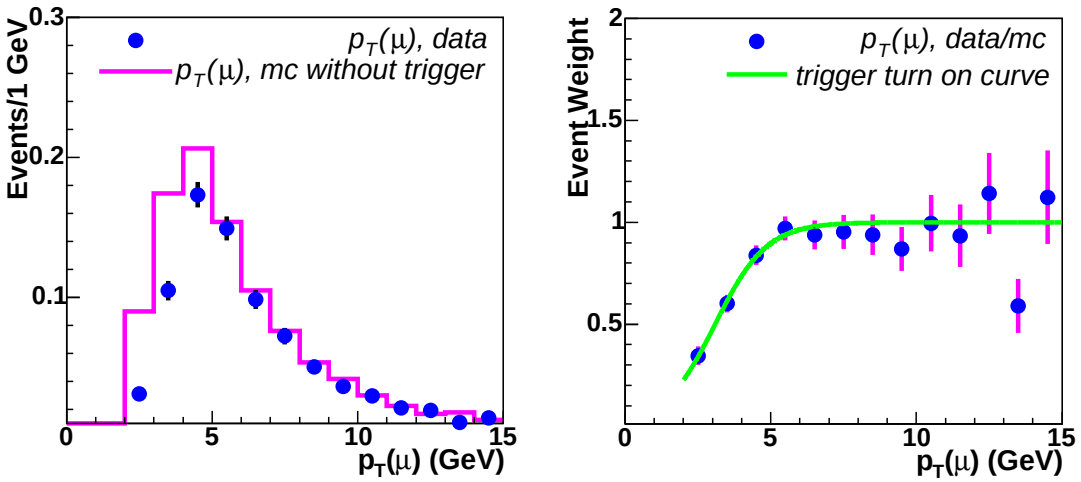

Figure 5.14: (a) Generated p_T distribution of μ after $B(p_T)$ reweighting, but before weighting due to trigger effects in the inclusive $D^*\mu$ MC sample compared to the $p_T(\mu)$ distribution from the data, both after application of $D^*\mu$ selection requirements. The difference at low p_T is due to trigger effects in the data. (b) Estimated trigger efficiency turn-on curve by taking the ratio of distributions in (a).

i.e.,

$$R_{D^*}^{gen} = \frac{\epsilon_{\bar{b}\to D^*\mu\nu}}{\epsilon_{B_s\to D_s^{**}\mu\nu, D_s^{**}\to D^*}}. \tag{5.14}$$

Using the MC sample of inclusive $b \to D^*\mu X$ events, specific major decays were identified as listed in Table 5.2. These decays are the principle b semileptonic decays and will be used to represent the inclusive $b \to D^*\mu\nu$ channel to which we are normalizing for this measurement. This sample

and the MC signal sample were both required to have $p_T^{\rm gen}(B) > 4$ GeV in the calculation of efficiencies as a point of normalization, and no MC events generated with $p_T(B) < 4$ GeV were observed to pass $D^*\mu$ selection cuts. Efficiencies for generated events to pass the $D^*\mu$ selection (but none of the K_S^0 requirements) were then determined and shown in Table 5.2. Errors on these efficiencies are due to MC statistics, including the additional statistical uncertainty produced due to the weighting procedure [50]. The predicted fraction, F_i of each channel contributing to the $D^*\mu$ sample before further cuts was found following a procedure similar to that given in Ref. [51]. To determine F_i, it was first necessary to identify the branching fraction for the decay channel indicated in Table 5.2. The desired quantity, however, is the fraction of the time that the D^* is produced in an inclusive $b \to D^*\mu X$ decay, so it was necessary to multiply each branching fraction by the appropriate hadronization fraction (f_i) [3]. From this, one could extract the fraction, F_i for each decay as shown in Table 5.1 below.

Table 5.1: Determination of fractions F_i.

Decay Channel	Br	f_i	$Br(b \to D^*\mu)$	F_i
$B_d^0 \to D^*\mu\nu$	$(5.44 \pm 0.23)\%$	0.398 ± 0.010	$2.17 \pm 0.09\%$	0.764 ± 0.032
$B_d^0 \to D^{**0}\mu\nu$	$(0.496 \pm 0.11)\%$	0.398 ± 0.010	$0.2 \pm 0.04\%$	0.070 ± 0.014
$B^+ \to D^{**+}\mu\nu$	$(1.06 \pm 0.24)\%$	0.398 ± 0.010	$0.42 \pm 0.1\%$	0.149 ± 0.029
$B_s^0 \to D^*\mu\nu$	$(0.49 \pm 0.42)\%$	0.107 ± 0.011	$0.05 \pm 0.04\%$	0.018 ± 0.015
$\sum Br(b \to D^*\mu X)$			2.84%	

The errors indicated on these fractions are dominated by uncertainties in PDG production fraction and branching ratio inputs (see Table 5.2), and are fully correlated (since they sum to unity by construction).

Table 5.2: Efficiencies for reconstructing $D^*\mu$ and fractions F_i.

Decay Channel	$\epsilon(b \to D^*\mu X)$	Fraction, F_i
$B_d^0 \to D^*\mu\nu$	$(6.02 \pm 0.14)\%$	0.764 ± 0.032
$B_d^0 \to D^{**0}\mu\nu$	$(4.29 \pm 1.05)\%$	0.070 ± 0.014
$B^+ \to D^{**+}\mu\nu$	$(6.49 \pm 0.72)\%$	0.149 ± 0.029
$B_s^0 \to D^*\mu\nu$	$(1.01 \pm 0.04)\%$	0.018 ± 0.015
$\sum \epsilon_i F_i$	$(5.88 \pm 0.80)\%$	

The efficiency to reconstruct a μD^* candidate in the $b \to D^*\mu\nu$ sample was found to be $(5.88 \pm 0.80)\%$.

Applying the same cuts for reconstructing $D^*\mu$ for the signal channel, the efficiency $\epsilon(B_s^0 \to D_{s1}\mu \to D^*\mu) = (3.20 \pm 0.02)\%$ (MC statistical error only) was found. It is not surprising that this efficiency is lower for the signal Monte Carlo since the D^* decay product cascades via the D_s^{**} resulting in a lower p_T of the D^* that in the inclusive semileptonic sample. The efficiencies in Equation 5.14 are then divided, resulting in the ratio of efficiencies of

$$R_{D^*}^{\text{gen}} = \frac{(3.20 \pm 0.02)\%}{(5.88 \pm 0.80)\%} = 0.547 \pm 0.075. \tag{5.15}$$

5.4.6 Efficiency to Reconstruct K^0_S

The final step in calculating the branching fraction is the determination of $\epsilon_{K^0_S}$. Once a K^0_S is produced in the detector, it will not be reconstructed with 100% efficiency. Some K^0_S will travel beyond the central tracking system before decay and thus will not be reconstructed, some tracks from K^0_S decay will have impact parameters too large to pass reconstruction criteria, and some K^0_S will be misreconstructed and therefore will not enter into the calculation. Therefore, events lost due to inefficient reconstruction of K^0_S will suppress the measured D^{**}_s production and an efficiency needs to be determined to correct for this effect. This efficiency is effectively that of reconstructing a $K^0_S \to \pi^+\pi^-$ and vertexing it with the $D^*\mu$, and already includes the branching ratio $Br(K^0_S \to \pi^+\pi^-) = 0.6895$ [3] for ease of use in calculating the product branching ratio. The signal MC sample was used to determine $\epsilon_{K^0_S}$ = (No. of $D^*\mu$ events passing additional K^0_S requirements)/(No. of $D^*\mu$ events), i.e., the efficiency to reconstruct $D^{\pm}_{s1}(2536) \to D^*K^0_S$ given a reconstructed $D^*\mu$ as a starting point.

The p_T-dependent weight factor as described previously was applied to the signal MC to result in a more realistic initial $p_T(B^0_s)$ distribution and the same trigger turn-on curve was applied to reweight the MC as with $R^{\rm gen}_{D^*}$. Figure 5.15 compares the $p_T(\mu)$ in the signal MC after reweighting with that found from $D^*\mu$ in the data after weighting and applying the weights of the trigger turn-on curve and shows agreement within statistical uncertainties.

Due to differences in the modeling of the $p_T(B)$ in reconstruction versions p17 and p14, the Monte Carlo sample was split into separate samples according to production version and efficiencies were calculated separately. For Monte Carlo produced with p14 the efficiency was found to be $\epsilon_{K^0_S} = (10.7 \pm 0.5)\%$ and for p17 the efficiency was $\epsilon_{K^0_S} = (10.6 \pm 0.4)\%$.

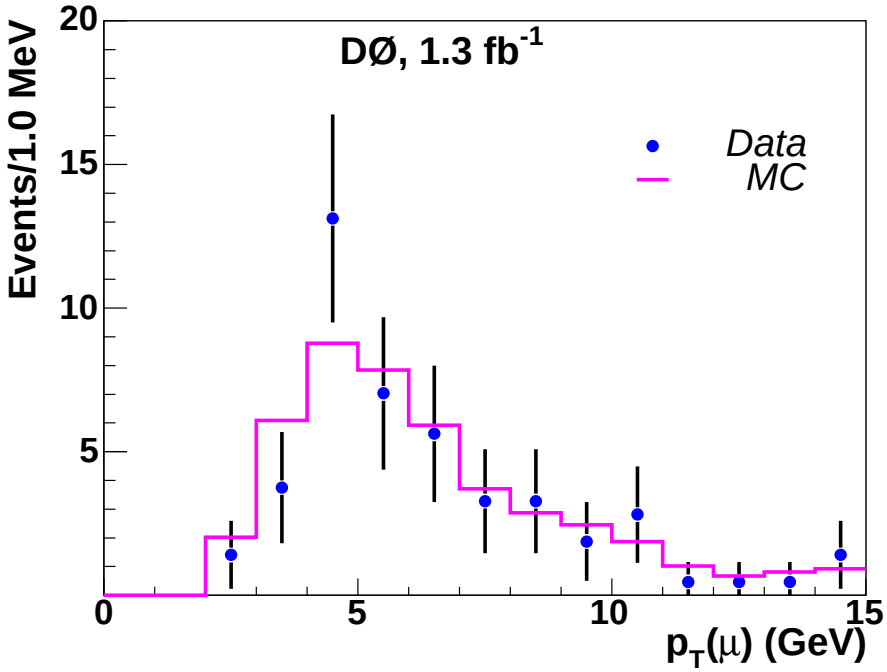

Figure 5.15: Comparison of the p_T of the μ in the signal MC after weighting described in the text to the $p_T(\mu)$ in the data, both after application of $D^*\mu$ requirements.

The data was reconstructed with version p17 and so the efficiency $\epsilon_{K^0_S}$ was taken to be $(10.6 \pm 0.4)\%$ with the differences to that found using p14 taken

as a systematic uncertainty. The quoted error is only due to MC statistics plus the statistical fluctuations of the weights [50]; additional errors due to the uncertainty in the determination of the weights and the procedure will be considered later.

The uncertainty in track reconstruction efficiency between data and Monte Carlo as a function of p_T is later taken as a systematic, but a correction to the efficiency is also needed for K^0_S mesons reconstructed outside the pseudo-rapidity range $|\eta| > 1.6$. When these correction factors (see Table 5.3) [52] are applied, the efficiency is slightly reduced to $(10.3 \pm 0.4)\%$. This is the value used in the final branching ratio calculation.

η range	Correction
$0.0 - 0.4$	(1.00 ± 0.01)
$0.4 - 0.8$	(1.00 ± 0.01)
$0.8 - 1.2$	(1.00 ± 0.01)
$1.2 - 1.6$	(1.00 ± 0.01)
$1.6 - 1.8$	(0.957 ± 0.01)
$1.8 - 2.2$	(0.912 ± 0.01)

Table 5.3: Pseudorapidity corrections for track-matching efficiency.

5.4.7 $c\bar{c}$ Contribution

A key component to the measurement of $Br(B^0_s \to D^-_{s1}(2536)\mu^+\nu X)$ is $N(D^*)$, the number of D^* events measured. However, events that enter into the D^* sample through the process $c\bar{c} \to D^{*-}\mu^+\nu X$ can also contribute to

$N_{\mu D^*}$, artificially inflating the branching ratio. To determine the number of events in our signal reconstructed from a prompt D^* and a nearby μ, a QCD inclusive Monte Carlo sample (`msel`=1) was generated in which each event was required to contain a D^* and a μ, but with no requirements on the parentage of the particle. These events were then fully reconstructed, vertexing the D^* and μ in the same manner as in the data, so the distribution includes μD^* events both from B hadrons and from $c\bar{c}$. With this sample, we can estimate the contribution from $c\bar{c}$ to the μD^* sample in data. This sample was reconstructed with the same impact parameter significance cuts as in data (see Section 5.2.4), so little $c\bar{c}$ contamination is expected since the sample is biased towards long-lived particles. Using this MC sample, an estimated $c\bar{c}$ contribution of $(3.4 \pm 0.2)\%$ is expected in the μD^* sample.

The $D^*\mu$ decay length significance cut was introduced in this analysis to reduce the $c\bar{c}$ contamination in the μD^* sample since these products from direct charm production will typically have shorter decay lengths than if they arise as products of B meson decay. For reasons described below, a decay length significance cut of $dL/\sigma_{dL} > 1$ was introduced to reduce the $c\bar{c}$ background. When this cut is applied to the Monte Carlo sample, the estimated $c\bar{c}$ contribution is further reduced to $(2.9 \pm 0.2)\%$.

Estimating the fraction of $c\bar{c}$ using MC studies may however have uncertainty due to incomplete knowledge in the modeling of all the relevant decays, including $c\bar{c}$ production via gluon splitting where the charm quarks

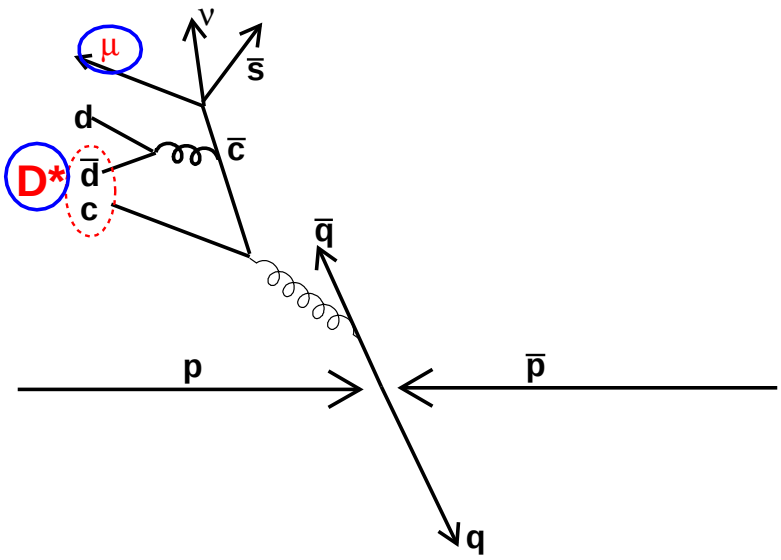

Figure 5.16: Contribution to $c\bar{c}$ contamination from gluon splitting.

are close in phase space as shown in Figure 5.16, with one decaying to D^* and the other to a muon.

As a systematic check on the $c\bar{c}$ contribution, the decay length significance distribution observed in the data, compared to the decay length significance distribution predicted by MC for $b \to D^*\mu X$ was also used to estimate the fraction of $c\bar{c}$ events in the $D^*\mu$ sample.

The analysis described in both Ref. [51] (before flavor tagging that reduces the $c\bar{c}$ contribution) and Ref. [55] use a similar selection for $D^*\mu$ before

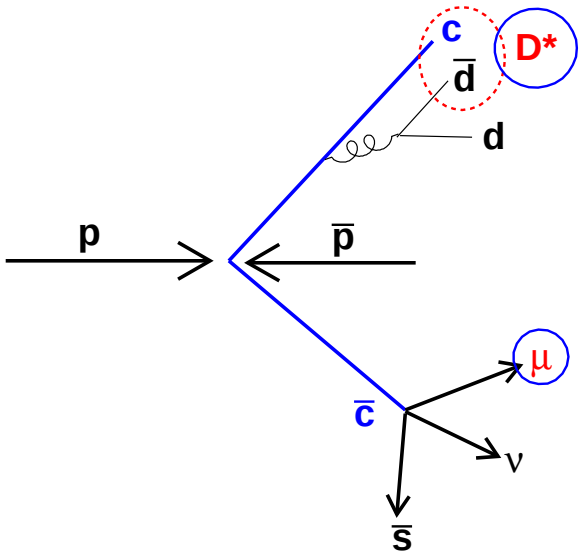

Figure 5.17: Contribution to $c\bar{c}$ contamination from direct $c\bar{c}$ production.

the decay length significance cut on the $D^*\mu$ vertex. From such previous studies, without the decay length significance cut, the fractional contribution for $c\bar{c}$ contamination was estimated to be $(9 \pm 3)\%$. The previous value of $(3.4 \pm 0.2)\%$ $c\bar{c}$ contamination included impact parameter significance cuts on the μD^* vertex; for the purpose of the following study, these cuts were removed.

Both the inclusive $p\bar{p} \to D^*\mu$ and signal $B_s^0 \to D_{s1}(2536)\mu\nu$ MC samples

were used to determine the expected shape of the decay length significance distribution for B decays. At a large value of significance greater than 5, where the charm contribution should be negligible, these MC distributions were scaled to give the same statistics as the data distribution beyond this value. For smaller values of the significance cuts, the excess of $D^*\mu$ candidates in the data above that predicted by the MC samples cutting at different significance values was attributed as coming from $c\bar{c}$. The average between the MC samples was taken, and the difference between the two MC predictions was taken as the systematic uncertainty added in quadrature with the statistical error.

Results of this study are given in Table 5.4.

Significance Cut	Estimated $c\bar{c}$ Fraction in $N_{D^*\mu}$
None	$(11.2 \pm 3.0)\%$
> 0	$(7.4 \pm 3.4)\%$
> 1	$(3.9 \pm 2.5)\%$
> 2	$(-0.2 \pm 2.8)\%$
> 3	$(3.2 \pm 1.8)\%$
> 4	$(2.2 \pm 2.4)\%$
> 5	0%

Table 5.4: Estimated fraction of $c\bar{c}$ in $D^*\mu$ sample as a function of the $D^*\mu$ decay length significance cut. The last entry is 0 by construction.

The observed value found when no decay length significance cut is applied is consistent with the $(9 \pm 3)\%$ estimated by other techniques [51, 56, 55]. As

the cut is tightened, the charm fraction drops as expected, until consistent with the previous result from Monte Carlo, albeit with significant uncertainty. This result is in agreement with the Monte Carlo studies and confirms the effectiveness of the decay length significance cut. For the cut value used in the analysis, the more conservative value of $(3.9 \pm 1.0)\%$ was used with the uncertainty being taken as the difference in the central value of the two estimates. The value of $N_{\mu D^*}$ was therefore scaled down appropriately, i.e., multiplied by 0.961 ± 0.010.

Regarding the possibility of residual $c\bar{c}$ contamination in $N_{D_{s1}(2536)}$, the fraction of c quarks fragmenting into $D_{s1}(2536)$ was estimated to be approximately 32 times smaller than the fraction of c quarks fragmenting into D^* from relative production ratios [57] and spin-counting arguments [58]. In the signal D_s^{**} mass distribution, contributions of D^* and μ arising from separate charm decays will not form a peak at the D_s^{**} mass peak, and will instead be included as part of the combinatorial background in the fit. However, if a real D_s^{**} arises from charm fragmentation, combined with a μ from the other charm decay, such a candidate will appear in the same D_s^{**} peak as the signal.

When the decay length significance cut on the $D^*\mu$ vertex was added, the resulting small drop in $N_{D_{s1}(2536)}$ in the data ($\sim 3\%$) was completely consistent with the small decrease in the efficiency for signal due the addition of this requirement.

Distributions of $D_{s1}(2536)$ decay length, decay length significance, and $D_{s1}(2536) - \mu$ invariant mass in the signal mass window, after sideband subtraction, were consistent between data and signal MC as shown in Fig. 5.21, with no significant discrepancies that may indicate the presence of $c\bar{c}$ contamination. Fig. 5.18(b) shows the event content of the QCD inclusive sample passing all cuts demonstrating no significant evidence for peaking backgrounds at the mass of the D_s^{**}, as expected. No evidence of the other doublet member, $D_{s2}^{*\pm}(2573)$, decaying into the same channel appears in the data. Shown are the contributions from $b \to D^* \mu\nu$ and from direct $c\bar{c}$ production (i.e., 'prompt'), with the remaining background being comprised of $b \to D^*$ through an intermediate excited state other than $D_{s1}(2536)$. Given this, no further correction to $N(D_s^{**})$ is made due to contamination from $c\bar{c}$.

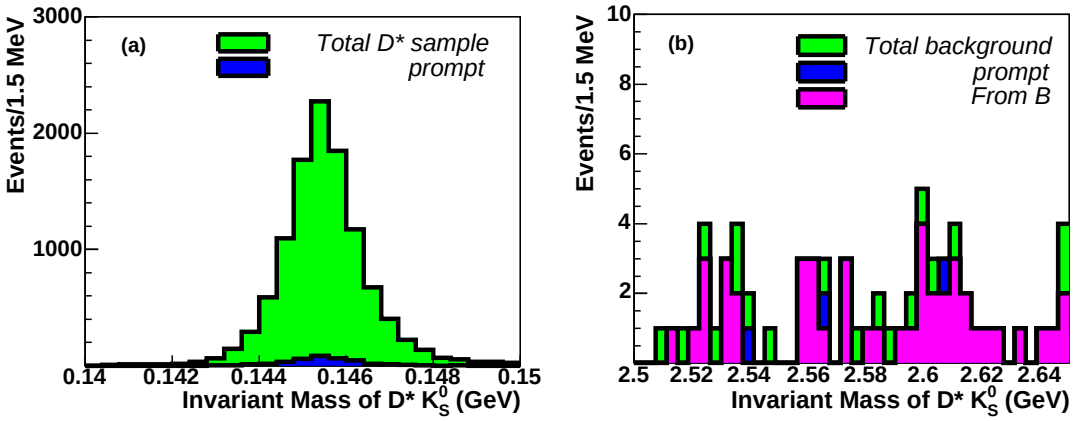

Figure 5.18: $c\bar{c}$ content in the QCD inclusive Monte Carlo sample for (a) the D^* mass difference and (b) the $D^* K_S^0$ invariant mass spectrum.

5.4.8 Product Branching Fraction

Using the equation of Section 5.1.3

$$f(\bar{b} \to B_s^0) \cdot Br(B_s^0 \to D_s^{**}\mu^+\nu X) \cdot$$
$$Br(D_s^{**} \to D^{*-}K_S^0) = Br(\bar{b} \to D^{*-}\mu^+\nu X) \cdot \frac{N_{D_s^{**}}}{N_{D^*\mu}} \cdot$$
$$\frac{\epsilon(\bar{b} \to D^*\mu)}{\epsilon(B_s^0 \to D_s^{**}\mu \to D^*\mu)} \cdot \frac{1}{\epsilon_{K_S^0}}, \ . \tag{5.16}$$

and the inputs discussed previously, the product branching ratio is determined to be:

$$f(\bar{b} \to B_s^0) \cdot Br(B_s^0 \to D_{s1}^-(2536)\mu^+\nu X) \cdot Br(D_{s1}^- \to D^{*-}K_S^0) =$$
$$(2.66 \pm 0.52\,(\text{stat.})) \times 10^{-4}, \tag{5.17}$$

i.e., this is the value for $Br(\bar{b} \to D_{s1}^-(2536)\mu^+\nu X) \cdot Br(D_{s1}^- \to D^{*-}K_S^0)$.

5.5 Systematic Uncertainties

For this analysis, systematic uncertainties are assigned for both the product branching ratio and the mass measurement. The total systematic uncertainty includes contributions from:

- $Br(\bar{b} \to D^{*-}\mu^+\nu X)$ uncertainty
- $N(D^*)$

  - signal and background modeling
  - $c\bar{c}$ contribution

- $N(D_s^{**})$
  - signal and background modeling
  - scaling of Monte Carlo Gaussian width

- $\epsilon_{K_S^0}$
  - Monte Carlo statistics
  - Semileptonic decay model
  - Weighting uncertainty
  - Detector modeling and track reconstruction efficiency uncertainty

- $R_{D^*}^{gen}$
  - MC statistics
  - PDG Br and f uncertainties
  - Weighting uncertainty
  - Semileptonic decay model

5.5.1 Systematic uncertainty on product branching ratio

The uncertainty in the normalizing branching ratio, $Br(\bar{b} \to D^{*-}\mu^+\nu X) = (2.75 \pm 0.19)\%$ [3], was taken as a systematic uncertainty.

Systematic uncertainty on $N(D^*)$

For determining $N_{D^*\mu}$, uncertainties in modeling the signal and background were studied. A triple Gaussian (each Gaussian with the same mean) was used instead of a double Gaussian to model the signal, and the background was fit using both an exponential function alone and an exponential function plus a square root function as opposed to the default exponential plus a polynomial. With each new model, the product branching ratio was recalculated and the maximum variation in each case was taken as the estimated systematic uncertainty due to fit modeling.

The estimated $c\bar{c}$ contribution of $(3.9 \pm 1.0)\%$ was varied by the indicated uncertainty.

Systematic uncertainty on $N(D_{s1})$

In the determination of $N_{D_{s1}(2536)}$, the signal model was varied in a number of ways to determine the sensitivity of the candidate yield. A fit was made to the $D^*K_S^0$ invariant mass with a double Gaussian with both means fixed instead of a Relativistic Breit-Wigner, giving a new D_s^{**} yield as shown in Figure 5.19, with which the Br was recalculated. Due to the fact that the

D_s^{**} width is extremely narrow as compared to the mass of the resonance, differences in fitting with a Breit-Wigner and Relativistic Breit-Wigner were found to be negligible and are not included as a systematic. The background model was changed to an exponential plus a square root function from the default exponential plus a polynomial and the variation in signal yield was taken as a systematic uncertainty.

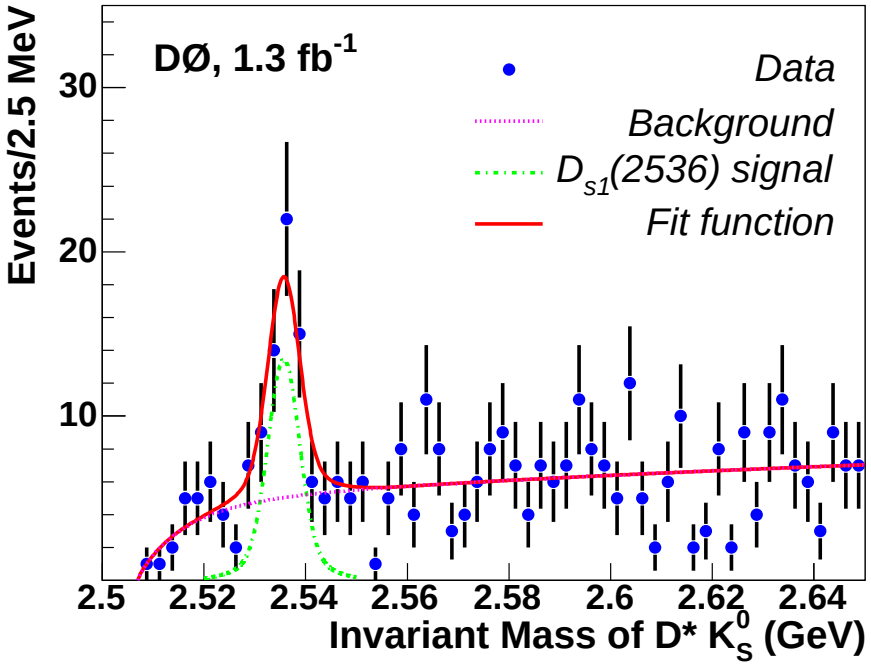

Figure 5.19: Invariant mass of $D^*K_S^0$. Shown is the result of the fit of the $D^*K_S^0$ mass with an exponential plus polynomial function with a threshold cutoff at $M(D^*) + M(K_S^0)$ to model the background and a double Gaussian with the same means to model the signal. The total number of $D_{s1}(2536)$ candidates in the peak is 46.3 ± 9.5(stat.).

As described in Section 5.3, the Monte Carlo predicts mass widths that are more narrow than those found in data and therefore the width of the detector resolution Gaussian function had to be scaled up. When using the predicted mass shape determined using Monte Carlo, the scaling of the widths was varied from 1.00 to 1.20 from the default value of 1.10 to check the sensitivity to uncertainty in mass resolution. The maximum variation from the default fit over these variations was taken as the systematic error due to this source.

Examination of MC events passing all cuts did not show any peaking backgrounds. As mentioned in Section 5.4.7, no peaking background is found due to $c\bar{c}$ contribution. The branching ratio of this state into $D^*K_S^0$ is expected to be low and even if a signal appeared, given the expected mass resolution, it would not contaminate the $D_{s1}(2536)$ mass peak.

Systematic uncertainty on $\epsilon_{K_S^0}$

By comparing the true $p_T(\mu)$ distribution for the signal using the default ISGW2 decay model [14] to the HQET semileptonic decay model [36] (see Figure 5.20), a weighting factor was found and applied to the fully simulated signal MC events. The determination of the weighting factor followed the methodology of Subsection 5.4.4. The p_T distributions were divided and a functional form was fit to the new distribution. This functional form was used to reweight all the distributions and the efficiency determined again. The difference observed was assigned as the systematic uncertainty due to

uncertainty on the decay model.

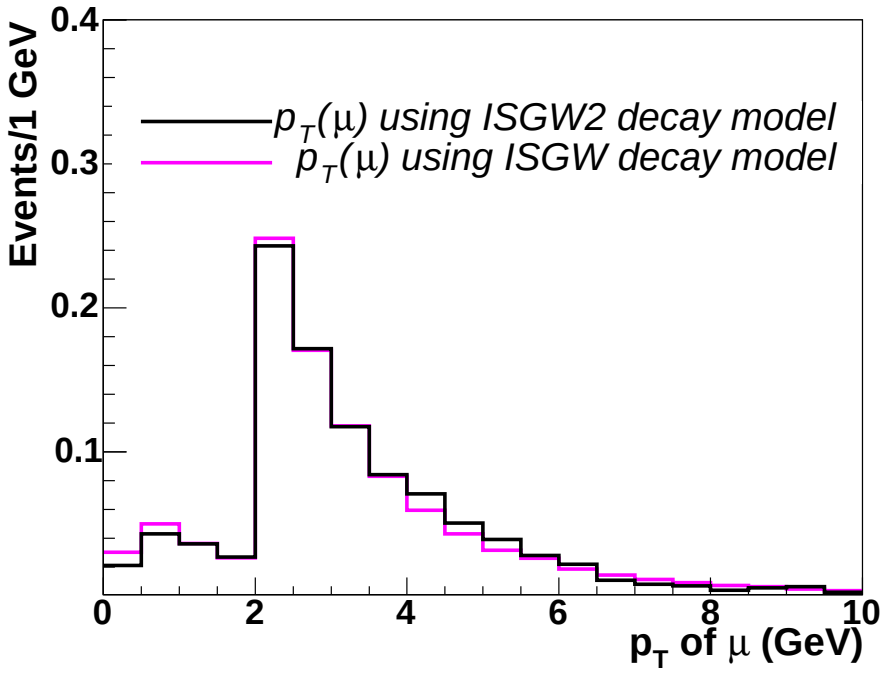

Figure 5.20: Comparison of true muon p_T between HQET and ISGW2 decay models in PYTHIA generation. These distributions were then divided to form a weighting function.

When finding $\epsilon_{K^0_S}$, the uncertainty in p_T weighting was found by using an alternate weighting technique, i.e., weighting instead using p_T of the $D^*\mu$ vertex in data and Monte Carlo. The variation in this efficiency was taken as the systematic error due to the uncertainty in the weighting procedure.

To assess the effects of differences between data and MC on the modeling of K^0_S kinematics and decay length, the p_T cut on the K^0_S was varied in steps

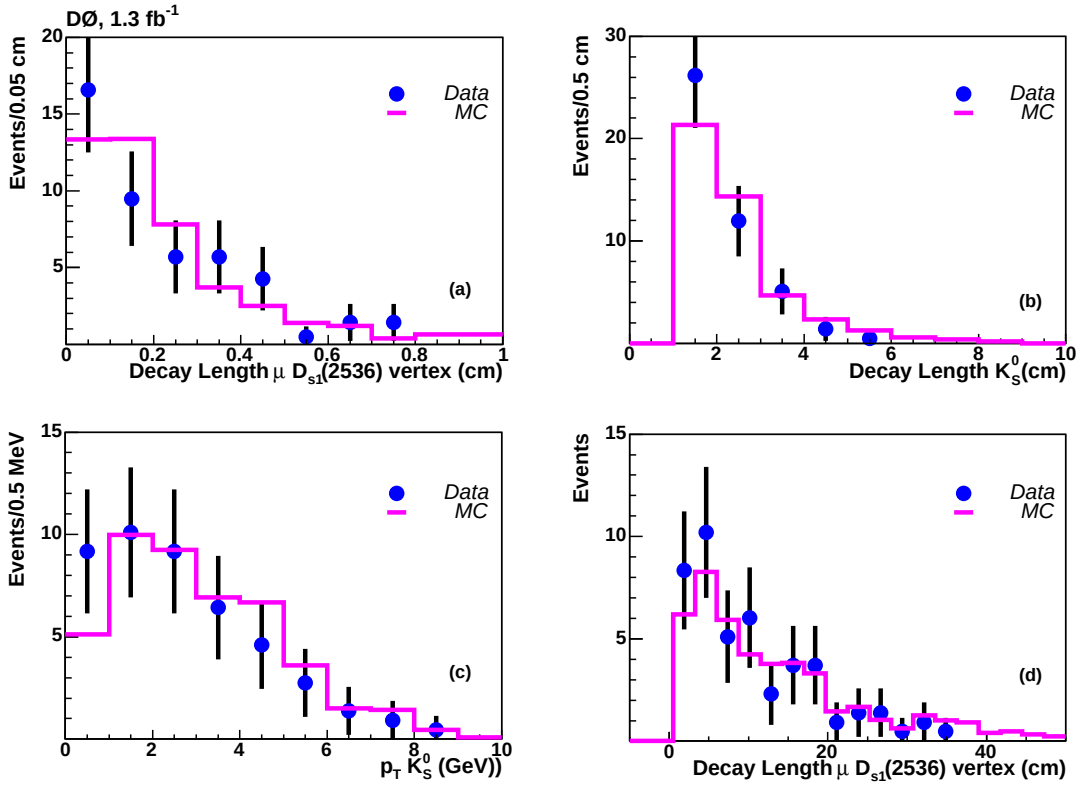

Figure 5.21: Comparison of data in the mass window $2.52 < M(D^*K^0_S) < 2.55$ GeV, after sideband subtraction, to signal MC for (a) decay length of the $D_{s1}(2536)$-μ vertex; (b) decay length of the K^0_S vertex; (c) decay length significance of $D_{s1}(2536)$-μ vertex; (d) p_T of K^0_S vertex.

from its nominal value of greater than 1.0 GeV down to 0.75 GeV and up to 1.50 GeV. The cut on the decay length of the K^0_S was varied in steps from its nominal value of 0.5 cm down to 0.25 cm and up to 1.5 cm. The resulting variation of the fitted signal divided by the new MC efficiency determined in each case was found and the RMS spread of these 'number produced' was

taken as a systematic uncertainty.

Discrepancies in track reconstruction efficiencies between data and Monte Carlo in low p_T tracks are accounted for by conservatively assigning a systematic uncertainty of 7% to each pion track in the K^0_S reconstruction that has a $p_T < 0.9$ GeV from studies of the soft pion from D^* [56] and an error of 1% taken for each track with a $p_T > 0.9$ GeV from studies of track-matched muons from J/ψ [49]. These errors were averaged over the p_T distributions of all the tracks used for a total uncertainty of 9.5%.

Systematic Uncertainty from $R^{D^*}_{gen}$

The uncertainty in $R^{\rm gen}_{D^*} = 0.547 \pm 0.049$ was due to uncertainties in the fractions F_i due to PDG branching ratio uncertainties as well as uncertainties in production fractions, $f(\bar{b} \to b\,\text{hadron})$.

Systematic effects on efficiencies due to decay modeling uncertainties as well as weighting factor uncertainties were tested as described earlier for $\epsilon_{K^0_S}$, applying different weighting to both the $D^*\mu$ inclusive sample and the signal MC sample. To assess the uncertainty of the trigger efficiency turn-on curve in the weighting, the MC was weighted to agree directly with $p_T(D^*\mu)$ without the turn-on curve, as well as varying the turn-on curve within statistical errors, and the difference was taken as a systematic uncertainty. The necessity of weighting as a function of η was explored by finding and then using a separate trigger turn-on curves in each of the two regions $|\eta| < 1$ and $|\eta| > 1$. The observed difference is 2.7% in the ratio of efficiencies.

The estimated systematic uncertainties on the product branching ratio are summarized in Table 5.5 and added in quadrature to obtain a total estimated systematic error on the product branching ratio of 16.6%.

Table 5.5: Estimated systematic uncertainties.

Source		Systematic Uncertainty
Normalizing Br	$Br(b \to D^* \mu X)$	6.9%
$N_{D^*\mu}$	Signal Modeling	0.5%
	Background Modeling	1.3%
	$c\bar{c}$ Contribution	1.0%
$N_{D_{s1}(2536)}$	Signal Modeling	3.0%
	Background Modeling	4.6%
$\epsilon_{K^0_S}$	MC Statistics	2.8%
	Semileptonic Decay Model	1.2%
	Weighting Procedure	2.4%
	Detector Modeling	4.0%
	Track Reconstruction Eff.	9.5%
$R^{\text{gen}}_{D^*}$	MC Statistics, PDG Br and f Uncertainties	8.2%
	Weighting Procedure	2.7%
	Semileptonic Decay Model	0.9%
Total		16.6%

Including the systematic uncertainty, the product branching ratio is determined to be:

$$f(\bar{b} \to B_s^0) \cdot Br(B_s^0 \to D_{s1}^-(2536)\mu^+\nu X) \cdot Br(D_{s1}^- \to D^{*-}K_S^0) = (2.66 \pm 0.52\,(\text{stat.}) \pm 0.44\,(\text{syst.})) \times 10^{-4}. \quad (5.18)$$

5.5.2 Systematic uncertainty on mass measurement

The same variations of the $D_{s1}(2536)$ mass signal model, as well as background functional form were made as described above, i.e., using Gaussian functions for the fit, the mass resolution variations, and the shape of the MC predicted peak, etc. The mass values used for the mass constraints on the decay products were varied within their PDG uncertainties, and also set to the DØ central fit values. A new central mass value found in each case. The maximum variation observed was 0.4 MeV/c^2. These tests were also repeated on the higher statistics of the signal MC with smaller variations found. The signal MC was broken up into 50 ensembles, each with statistics close to the data, and the mass found in each case. Examples of this are shown in Figure 5.22. Plotting the pull distribution, which is defined as:

$$\frac{M(D_s^{**})_{measured} - M(D_s^{**})_{true}}{\sigma_{measured}}, \quad (5.19)$$

a pull distribution is calculated and fit to a Gaussian function. The fit yields a central value of 0.193 ± 0.281 and a width of 0.85 ± 0.3. Given that the pull is consistent with zero and the width of the pull distribution is consistent with one, one can conclude that the assigned statistical error is

consistent, and that no significant bias in mass exists in these size samples.

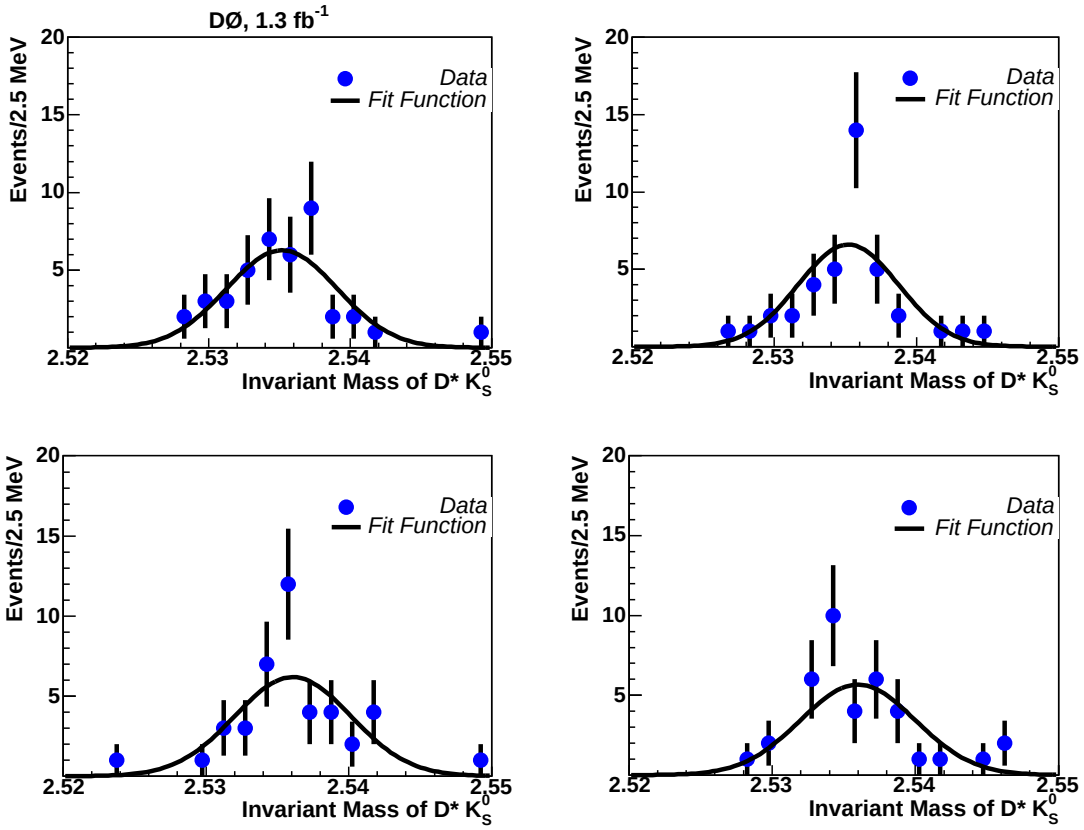

Figure 5.22: Four examples of ensemble tests.

The mass value found tends to remain stable due to the mass constraints on the decay products, as well as the peak location close to threshold, despite the larger variations observed in other typical mass peaks due to momentum scale uncertainties. The difference between the mass fit in the large signal MC sample and the input PDG mass value was 0.16 ± 0.10 MeV/c^2 and

the full mass difference with error was taken as a systematic. To check for momentum scale shifts for the signal, the fitted value of the mass difference $M(D^*) - M(D^0)$ in the data, signal MC, and inclusive $D^*\mu$ MC were compared to the PDG value, with a maximum observed difference of 0.2 MeV. An unbinned likelihood fit was made to the invariant mass distribution with minimal difference in fitted mass value. A total estimated systematic mass error of 0.5 MeV/c^2 was taken, for a mass measurement of $M(D_{s1}(2536)) = 2535.7 \pm 0.6\,(\text{stat.}) \pm 0.5\,(\text{syst.})$ MeV/c^2.

5.6 Cross Checks

5.6.1 Measuring the K^0_S lifetime

An important cut in this analysis is the cut on the decay length of the K^0_S. As shown in Figure 5.23, the decay length distribution of the K^0_S in data is consistent within statistics with the MC prediction after the cut. As mentioned previously, this cut removes a great deal of the background by not considering the soft pion tracks from the primary vertex and the many other tracks that would result in a large combinatorial background. It is essential, however, to make sure that this cut is not biasing the analysis in any way and to assess the impact of this cut on the final result. One of the systematic studies discussed in Section 5.5.1 varies the decay length cut to determine the systematic uncertainty due to this cut. In addition to this systematic uncertainty, we can also check that we can measure the K^0_S lifetime after all

our cuts.

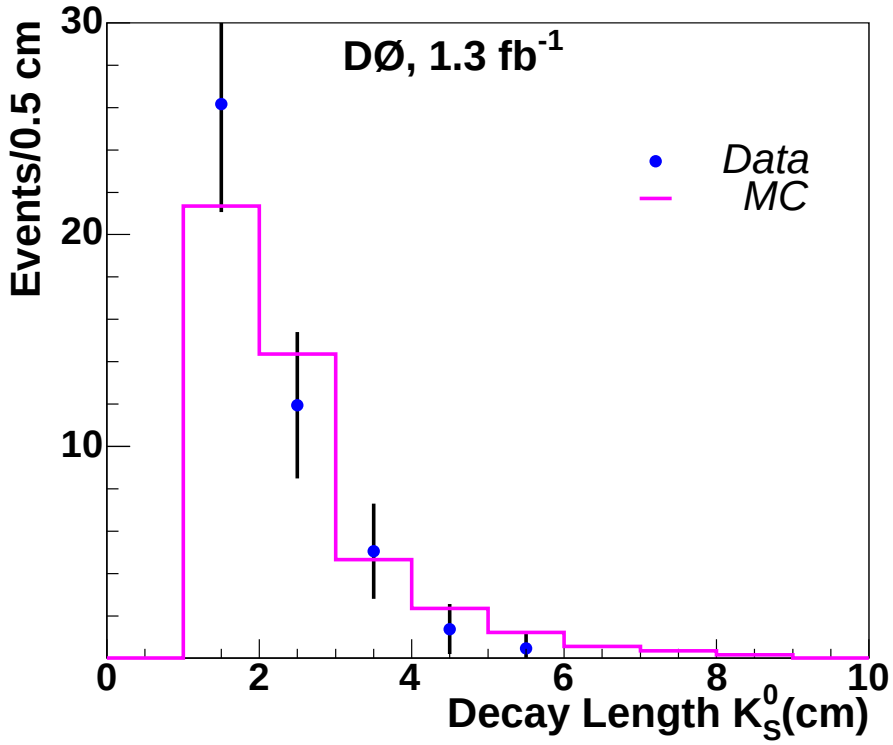

Figure 5.23: A plot of the decay length of K_S^0 in data compared with the reweighted Monte Carlo after the 0.5 cm cut.

The challenge with measuring the lifetime of the K_S^0 is that it is a long-lived, neutral particle. Track reconstruction efficiency track decreases with increased radial distance of closest approach of the tracks from the beamspot and, as a result, the longer-lived K_S^0 particles have a greater tendency to go undetected and thus the lifetime is biased towards shorter lifetimes. In addition to failing to reconstruct tracks, longer lived tracks will also decay

outside the tracking volume and will thus go undetected. To account for this bias, a tracking efficiency function is determined using the K^0_S decay length distribution in signal Monte Carlo and data.

The proper lifetime is given by $\tau = (\frac{\delta L_{xy}}{p_T} \cdot m)$, where L_{xy} is the transverse decay length of the K^0_S, p_T is the transverse momentum of the particle, and m is the mass of the K^0_S. In the following sections, we will quote proper decay length ($c\tau$) in cm.

To correct for detector inefficiencies, an efficiency curve as a function of L_{xy} was determined (Figure 5.24) using signal Monte Carlo at the PYTHIA generator four-vector level to determine the true transverse decay length and p_T of all K^0_S produced. Fully reconstructed signal Monte Carlo was used to determine the transverse decay length and p_T of fully reconstructed K^0_S events and the efficiency curve was determined by dividing the reconstructed proper decay length by the true proper decay length. This efficiency curve was then applied to the K^0_S decay length in data and the corrected proper decay length was compared between data and Monte Carlo (Figure 5.25) and found to be consistent. For both data and Monte Carlo, only K^0_S mesons passing all cuts for the D^{**}_s sample were retained.

Fitting the data to an exponential as shown in Figure 5.26, a proper decay length of 2.58 ± 0.10 cm was found with a $\chi^2/d.o.f = 4.99/5$ and the lifetime is determined to be consistent with the PDG value of 2.67cm [3].

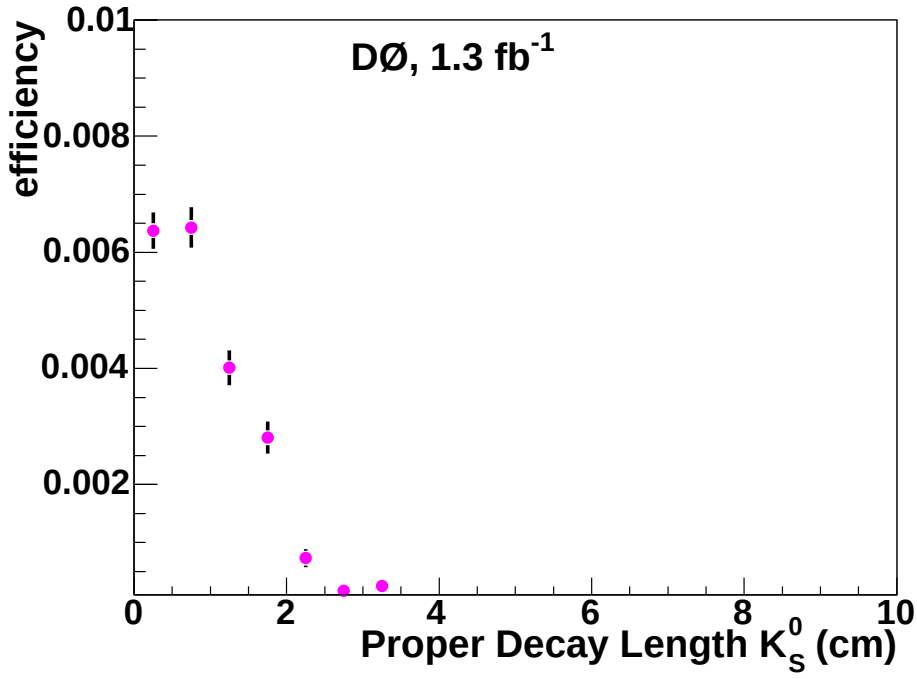

Figure 5.24: The efficiency curve determined for correcting the K_S^0 proper decay length.

5.6.2 Angular Distribution

Since we are analyzing the decay $B_s^0 \to D_{s1}^-(2536)\mu^+\nu X$, with the expectation that the D_s^{**} will have a narrow width due to the fact that it is a D-wave decay, it is useful to check that the decay angular distribution measured agrees with our expectations. Thus, in the following section we will compare the angular distribution found in data with that given by Monte Carlo.

To perform an angular analysis of the $D_{s1}^{\pm}(2536) \to D^{*\pm}K_S^0$ decay, it is

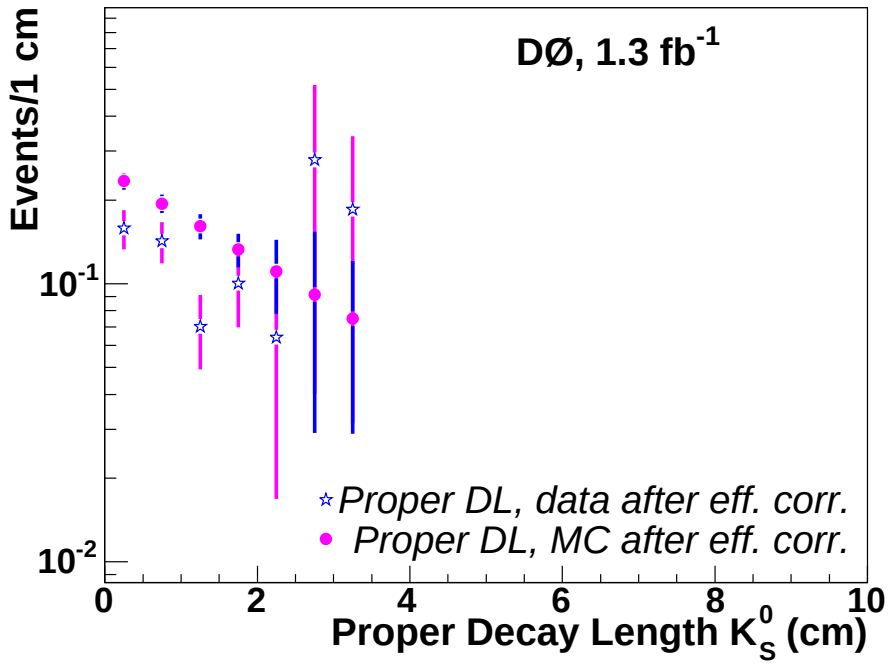

Figure 5.25: Proper decay length of K_S^0 compared between data and Monte Carlo after efficiency correction.

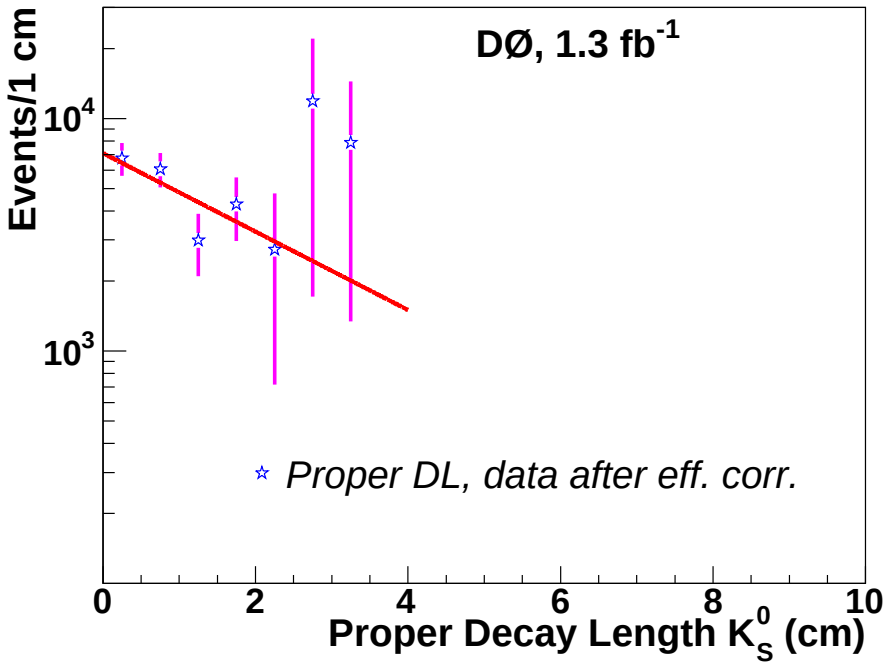

Figure 5.26: Proper decay length of K_S^0 in data after efficiency correction. The line is a fit to the data with an exponential function giving a proper decay length of 2.58 ± 0.10 cm.

first necessary to define the angle which will be measured. The angle α is the angle between the K_S^0 momentum and the boost direction in the rest frame of the $D_{s1}^{\pm}(2536)$ as shown in Figure 5.27. The BELLE Collaboration has measured the distribution of additional angles [24] between decay products in the $D_{s1}^{\pm}(2536) \to D^{*\pm}K_S^0$ decay, including β, the angle between the decay plane and the plane formed by the boost direction and the K_S^0 momentum, and γ, the angle between the K_S^0 and π in the rest frame of the D^*.

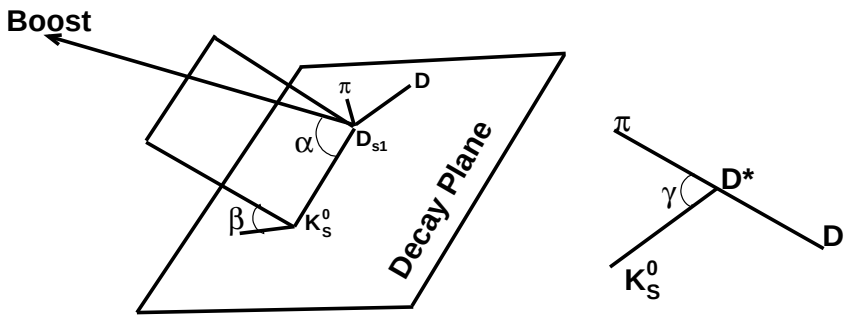

Figure 5.27: Schematic of definition of decay angles discussed in the text [24].

The distribution of the angle α measured in data is not flat, as shown in Figure 5.28. This indicates that the decay is not pure S-wave but is rather some linear combination of S and D wave. It is not, however, expected that the decay of the $D^{\pm}_{s1}(2536)$ would be either pure D-wave or S-wave. In the limit $m_Q \gg \Lambda_{QCD}$, we expect a pure D-wave decay, but after introducing $1/m_q$ corrections this perfect symmetry breaks down and an S-wave component is expected to be introduced.

Comparing the angular distribution of the signal in data with the signal Monte Carlo angular distribution as shown in Figure 5.28, we see that the data and Monte Carlo are consistent within the small statistics available, i.e.,

the observed decay angular distribution of the $D_{s1}(2536)$ is consistent with theoretical expectations.

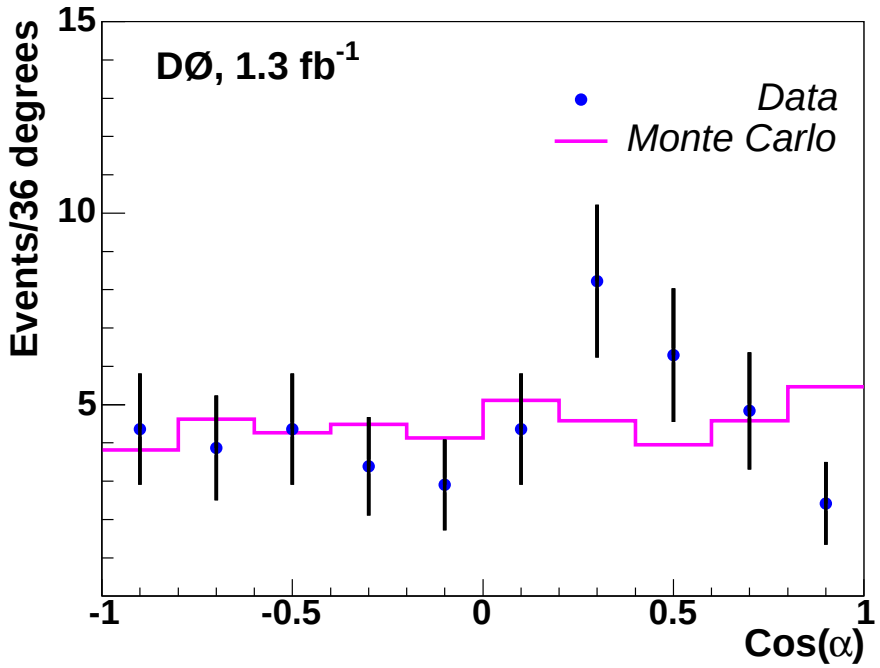

Figure 5.28: Comparing the decay angle α in data and Monte Carlo.

Chapter 6

Summary and Conclusion

In summary, we have measured in DØ data the product branching ratio $Br(B_s^0 \to D_{s1}^-(2536)\mu^+\nu X)$ to be

$$f(\bar{b} \to B_s^0) \cdot Br(B_s^0 \to D_{s1}^-(2536)\mu^+\nu X) \cdot Br(D_{s1}^- \to D^{*-}K_S^0) = (2.66 \pm 0.52\,(\text{stat.}) \pm 0.44\,(\text{syst.})) \times 10^{-4}. \quad (6.1)$$

To compare this result with theoretical predictions, it is necessary to extract $Br(B_s^0 \to D_{s1}^-(2536)\mu^+\nu X)$. The semileptonic branching ratio alone is extracted by taking the hadronization fraction into B_s^0 as $f(\bar{b} \to B_s^0) = 0.107 \pm 0.011$ [3]. By spin-counting and isospin arguments, $D_{s1}(2536)$ is expected to decay to D^*K^0 half of the time and K^0 will decay a K_S^0 half of the time, and so it is assumed that $Br(D_{s1}(2536) \to D^*K_S^0) = 0.25$ [36]. Inputting these numbers, the first experimental measurement of this value is found to be

$$Br(B_s^0 \to D_s^{**}\mu^+\nu X) = [1.00 \pm 0.20\,(\text{stat}) \pm 0.17\,(\text{syst}) \pm 0.14\,(\text{prod.frac.})]\% \tag{6.2}$$

This value is compared to a number of theoretical predictions [19, 20, 17] discussed earlier in Section 2.6 and given in Table 6.1. The systematic uncertainty on this quantity is as described earlier, and the error labeled '(prod. frac.)' is due to the current uncertainty on $f(\bar{b} \to B_s^0)$.

Table 6.1: Experimental measurement compared with various theoretical predictions.

Source	$Br(B_s^0 \to D_{s1}(2536)\mu\nu X)$
This result	$[1.00 \pm 0.20\,(\text{stat})$
	$\pm 0.17\,(\text{syst}) \pm 0.14\,(\text{prod.frac.})]\%$
	$Br(B_s^0 \to D_{s1}(2536)\mu\nu)$
ISGW2 [19]	$(0.53 \pm 0.27)\%$
Relativistic Quark Model & $1/m_Q$ corrections [20]	$(1.06 \pm 0.16)\%$
HQET & QCD sum rules [17]	0.195%

As one can see from Table 6.1 and Fig. 6.1, the measured value is in most consistent with the predictions made by RQM and agrees within error with that predicted by ISGW2. HQET does not agree with measurement, but this theory does not include any $1/m_Q$ or relativistic corrections, resulting in the lower predicted value. Note that this measurement includes any con-

tribution from decays with more than three-bodies. Although contributions are expected to be small ($\tilde{<}$ 15%), they still may contribute at some level.

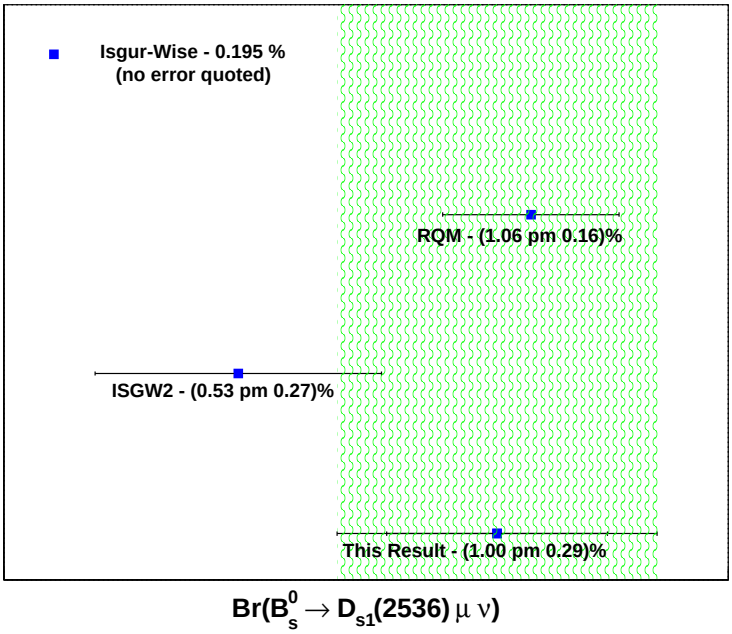

Figure 6.1: Comparison of this measurement with several theoretical predictions

An additional measurement made in this analysis is the mass of $D_{s1}(2536)$. The measured mass value of the $D_{s1}(2536)$ of

$$M(D_{s1}(2536) = 2535.7 \pm 0.6\,(\text{stat.}) \pm 0.5\,(\text{syst.})\ \text{MeV}/c^2 \qquad (6.3)$$

can be compared to the PDG average value of 2535.34 ± 0.31 MeV/c^2 [3] and is found to be consistent.

The measurement of $Br(B_s^0 \to D_{s1}^-(2536)\mu^+\nu X)$ is the first measurement of the branching ratio of a B_s to any orbitally excited D_s state. The value measured was found to be in agreement with theoretical measurements which include higher order $1/m_Q$ and relativistic corrects, thus further demonstrating the need for future development of these methods.

Chapter 7

Appendix A

7.1 d0_mess cuts

7.1.1 Signal Monte Carlo d0_mess cuts

For the signal Monte Carlo, all $B_s^0 \to D_{s1}^-(2536)\mu^+\nu X$ decays were used and the D_s^{**} was forced to decay to $D^*K_S^0$. See Appendix 7.2.1 for full decay path.

The `d0_mess` file filtered events as follows:

- Each event was required to have a $\bar{b}b$ pair.
- Each event was required to have at least one B_s^0 or $\bar{B}_s^o$.
- All B_s^0 decay products were required to be within the range $|\eta| < 2.5$.
- The muon from the B_s^0 was required to have a $p_T > 2$ GeV.
- Each event was required to have a $D_{s1}^{\pm}(2536)$ with a B_s^0 as a parent.

- The K_S^0 from the $D_{s1}^{\pm}(2536)$ was required to have a $p_T > 0.5$ GeV.
- The D^0 from the D^* decay was required to have a $p_T > 1$ GeV and the π^* from the D^* decay was required to have a $p_T > 0.17$ GeV.

```
   string PackageName = 'd0_mess'
   string PackageName = 'd0_mess'
   bool d0_mess_on = true
   bool HardScatterCuts_on = false
   int DebugLevel = 1
   int NumberOfCuts = 9
   string Cut1 = 'PdgId == 5'
   string Cut2 = 'PdgId == -5'
   string Cut3 = 'PdgId == 531 || PdgId == -531'
   string Cut4 = '(PdgId == -13 && ParentId==531 && Pt>2 && AbsEta<2.5)
|| (PdgId == 13 && ParentId==-531 && Pt>2 && AbsEta<2.5)';
   string Cut5 = '(PdgId == -10433 && ParentId == 531) || (PdgId
== 10433 && ParentId == -531)'
   string Cut6 = '(PdgId == 311 && ParentId == 10433 && Pt>0.5) ||
(PdgId == -311 && ParentId == -10433 && Pt>0.5)'
   string Cut7 = '(PdgId == 413 && ParentId == 10433) || (PdgId ==
-413 && ParentId == -10433)'
   string Cut8 = '(PdgId == 211 && ParentId==413 && Pt>0.17) || (PdgId
== -211 && ParentId==-413&&Pt>0.17)';
```

```
string Cut9 = '(PdgId == 421 && ParentId==413 && Pt>1) || (PdgId
== -421 && ParentId==-413&&Pt>1.0)';
```

7.1.2 QCD inclusive background Monte Carlo

For the QCD Inclusive (`msel=1`) Monte Carlo generated, all events with a muon, a D^* meson, and a K^0_S meson were retained. See Appendix 7.2.2 for full decay path.

The `d0_mess` file filtered events as follows:

- All decay products were required to be within the range $|\eta| < 2.5$.
- Each event was required to have a D^*
- Each event was required to have a K^0_S with a $p_T > 1$ GeV.
- The D^0 from the D^* decay was required to have a $p_T > 3$ GeV and the pi^* from the D^* decay was required to have a $p_T > 0.17$ GeV.
- Each event was required to have a μ with a $p_T > 2.5$ GeV.

```
string PackageName = 'd0_mess'
bool d0_mess_on = true
bool HardScatterCuts_on = false
int DebugLevel = 1
int NumberOfCuts = 5
```

```
   string Cut1 = '(PdgId == 311 && Pt>1 && AbsEta<2.5) || (PdgId
== -311 && Pt>1 && AbsEta<2.5)'
   string Cut2 = '(PdgId == 413 && AbsEta<2.5) || (PdgId == -413
&& AbsEta<2.5)'
   string Cut3 = '(PdgId == 211 && ParentId==413 && Pt>0.17 && AbsEta<2.5)
|| (PdgId == -211 && ParentId==-413&&Pt>0.17 && AbsEta<2.5)';
   string Cut4 = '(PdgId == 421 && ParentId==413 && Pt>3 && AbsEta<2.5)
|| (PdgId == -421 && ParentId==-413&&Pt>3.0 && AbsEta<2.5)';
   string Cut5 = '(PdgId == -13 && Pt>2.5 &&AbsEta<2) || (PdgId ==
13 && Pt>2.5 && AbsEta<2)'
```

7.2 User Decay Files

7.2.1 Signal Monte Carlo

```
   Decay B_s0
   1.000 D_s1- mu+ nu_mu PHOTOS ISGW2;
   Enddecay
   Decay anti-B_s0
   1.000 D_s1+ mu- anti-nu_mu PHOTOS ISGW2;
   Enddecay
   Decay D_s1-
   1.000 D*- anti-K0 VVS_PWAVE 0.0 0.0 0.0 0.0 1.0 0.0;
   Enddecay
```

```
Decay D_s1+
1.000 D*+ K0 VVS_PWAVE 0.0 0.0 0.0 0.0 1.0 0.0;
Enddecay
Decay D*-
1.000 anti-D0 pi- VSS;
Enddecay
Decay anti-K0
1.000 K_S0 PHSP;
Enddecay
Decay D*+
1.000 D0 pi+ VSS;
Enddecay
Decay K0
1.000 K_S0 PHSP;
Enddecay
Decay K_S0
Enddecay
Decay anti-D0
1.000 K+ pi- PHSP;
Enddecay
Decay D0
1.000 K- pi+ PHSP;
```

```
Enddecay

End
```

7.2.2 QCD Inclusive Monte Carlo

```
 Decay D*-

1.000 anti-D0 pi- VSS;

Enddecay

Decay anti-K0

1.000 K_S0 PHSP;

Enddecay

Decay D*+

1.000 D0 pi+ VSS;

Enddecay

Decay K0

1.000 K_S0 PHSP;

Enddecay

Decay K_S0

Enddecay

Decay anti-D0

1.000 K+ pi- PHSP;

Enddecay

Decay D0
```

```
1.000 K- pi+ PHSP;

Enddecay

End
```

Bibliography

[1] S. Weinberg, Phys. Rev. Lett. **19**, 1264 (1967); A. Salam, "Elementary Particle Theory", ed. N.Svartholm, Almquist and Wiksells, Stockholm, p. 367, (1969).

[2] Y. Fukuda *et al.* [Super-Kamiokande Collab.], Phys. Rev. Lett. **81**, 1562 (1998).

[3] W.-M. Yao *et al.*, Journal of Physics G **33**, 1 (2006).

[4] A. Pich, *'The Standard Model of Electroweak Interactions'*, hep-ph/0502010.

[5] P.W. Higgs, Phys. Lett. **12**, 132 (1964).

[6] W. Marciano and H. Pagels, Phys. Rep. C **52**, 137 (1954).

[7] N. Cabibbo, Phys. Rev. Lett. **10**, 531 (1963).

[8] L. Wolfenstein, Phys. Rev. Lett. **51**, 1945 (1983).

[9] R. Fleischer, *'Flavour Physics and CP Violation'*, arXiv:hep-ph/0405091v1.

[10] C. Jarlskog, Phys. Rev. Lett. **55**, 1039 (1985).

[11] S.W. Bosch, *'CKM Overview and Determinations from B Decays'*, hep-ph/0506153.

[12] M. Neubert, *'Heavy-Quark Effective Theory'*, hep-ph/9610266.

[13] N. Isgur and M.B. Wise, Phys. Rev. Lett. B **232**, 113 (1989).

[14] D. Scora and N. Isgur, Phys. Rev. D **52**, 2783 (1995).

[15] T. Mannel, *'Review of Heavy Quark Effective Theory'*, hep-ph/9611411v1.

[16] F. Halzen and A. Martin, *'Quarks and Leptons: An Introductory Course in Modern Particle Physics'*, John Wiley & Sons, New York, NY (1984).

[17] H. B. Mayorga, A. Moreno Briceno and J. H. Munoz, J. Phys. G **29**, 2059 (2003).

[18] Particle Data Group, D. E. Groom *et al.*, Eur. Phys. J. C **15**, 1, (2000).

[19] Ref. [17], for input using the results of [14].

[20] D. Ebert, R. N. Faustov, and V. O. Galkin, Phys. Rev. D **61**, 014016 (2000).

[21] B. Aubert *et al.* [BaBar Collab.], Phys. Rev. Lett. **90**, 242001 (2003) ; D. Besson *et al.* [CLEO Collab.], Phys. Rev. D **68**, 032002 (2003); P. Krokovny *et al.* [BELLE Collab.], Phys. Rev. Lett. **91**, 262002 (2003).

[22] S. Godfrey and N. Isgur, Phys. Rev. D **32**, 037502 (1985); S. Godfrey and R. Kokoski, Phys. Rev. D **43**, 1679 (1991); M. Di Pierro and E. Eichten, Phys. Rev. D **64**, 114004 (2001).

[23] M. Huang, Phys. Rev. D **69**, 114015 (2004).

[24] V.Balagura, *et al* [Belle Collab.], *'Observation of* $D_{s1}(2536)^+ \rightarrow D^+\pi^-K^+$, arXiv:hep-ex/0507030v1.

[25] A. V. Evdokimov *et al.* [SELEX Collab.], Phys. Rev. Lett. **93**, 242001 (2004).

[26] J. Thomspon, *'Introduction to Colliding Beams'*, FERMILAB-TM-1909 (1994).

[27] http://www-bd.fnal.gov/public/proton.html.

[28] http://www-bd.fnal.gov/public/maininj.html.

[29] http://www-bd.fnal.gov/public/antiproton.html.

[30] V.M. Abazov *et al.* [D0 Collab.], Nucl. Instrum. Meth. A **565**, 463 (2006).

[31] V.M. Abazov *et al.* [DO Collab.], Nucl. Instrum. Meth. A **552**, 372 (2005).

[32] L3 DAQ web page, http://www-d0online.fnal.gov/www/groups/l3daq/doc/.

[33] A. Khanov, *'HTF: histogramming method for finding tracks. The algorithm description'*, DØ Note 3778 (2000).

[34] G. Borrisov, *'Technical Details of AA Tracking'*, DØ Note in preparation, http://www-d0.fnal.gov/global_tracking/talks/

[35] T. Sjöstrand *et al.*, Comp. Phys. Comm. **135**, 238 (2001).

[36] D. J. Lange, Nucl. Instrum. and Methods A **462**, 152 (2001).

[37] Y. Fisyak, J. Womersley, 'DØGSTAR*:* DØGEANT *Simulation of the Total Apparatus Response'*, DØ Note 3191 (1997).

[38] S. Youssef *et al.*, 'DØSIM *User Manual'*, DØ Note 407 (1986).

[39] R. Brun *et al.*, CERN Report No. DD/EE/84-1, 1984.

[40] T. Bose, *'Search for B_s^0 oscillations at DØ'*, Ph.D. Thesis, Columbia University, New York (2005).

[41] M. Paulini, Int. J. Mod. Phys. A **14** 2791 (1999).

[42] T. Andeen *et al.*, *'The DØ Experiment's Intergrated Luminosity for Tevatron Run IIa'*, FERMILAB-TM-2365 (2007).

[43] p17 release.
http://www-d0.fnal.gov/computing/algorithms/.

[44] Muon ID web page
http://www-d0.fnal.gov/computing/algorithms/muon/muon_algo.html.

[45] S. Catani, Yu.L. Dokshitzer, M. Olsson, G. Turnock, B.R. Webber, Phys. Lett. B **269**, 432 (1991).

[46] B. Aubert *et al.*, BABAR-CONF-06/019, (2006), hep-ex/0607084.

[47] D. Krop, *'Search for B_s^0 oscillations at the Tevatron Collider Experiment DØ'*, Ph.D. Thesis, Indiana University, Bloomington (2007).

[48] S. Eidelman *et al.*, Phys. Lett. B **592**, 1 (2004).

[49] V.M. Abazov *et al.* [D0 Collab.], Phys. Rev. Lett. **94**, 071802 (2005); private communication, R. Bernhard.

[50] C. Blocker, CDF Memo/Statistics/Public/7168, (2004).

[51] V. Abazov *et al.* [D0 Collab.], Phys. Rev. D **74**, 112002 (2006).

[52] V. Abazov *et al.*, [D0 Collab.], Phys. Rev. Lett. **94**, 232001 (2005).

[53] N. Isgur and M. B. Wise, Phys. Rev. Lett. **66**, 1130 (1991).

[54] V. M. Abazov *et al.* [D0 Collab.], Phys. Rev. Lett. **94**, 182001 (2005).

[55] C. Ay *et al.*, DØ Note 4639, (2006).

[56] V. M. Abazov *et al.* [D0 Collab.], Phys. Rev. Lett. **95**, 171803 (2005).

[57] D. Acosta *et al.* [CDF Collab.], Phys. Rev. Lett. **91**, 241804 (2003).

[58] A. F. Falk and M. E. Peskin, Phys. Rev. D **49**, 3320 (1994).